Evaluating Fluoride Molten Salt Thermophysical Properties with Transient Grating Spectroscopy

By

Sean Gunn Robertson

B.Sc. Chemistry, Mount Allision University (2013)
M.Sc. Nuclear Reactor Physics and Engineering, Université Paris XI (2015)

Submitted to the Department of Nuclear Science and Engineering
In partial fulfilment of the requirements for the degree of

Doctor of Philosophy in Nuclear Science and Engineering

at the

Massachusetts Institute of Technology

May 2022

Author..
Department of Nuclear Science and Engineering
May 2nd, 2022

Certified by...
Michael P. Short
Class of '42 Associate Professor of Nuclear Science and Engineering
Thesis Supervisor

Certified by...
Antoine Allanore
Associate Professor of Metallurgy
Thesis Reader

Accepted by...
Ju Li
Battelle Energy Alliance Professor of Nuclear Science and Engineering
Professor of Materials Science and Engineering
Chairman, Department Committee on Graduate Theses

Evaluating Fluoride Molten Salt Thermophysical Properties with Transient Grating Spectroscopy
by
Sean Gunn Robertson
Submitted to the Department of Nuclear Science and Engineering
On May 2nd, 2022, in partial fulfillment of the requirements for the degree of
Doctor of Philosophy in Nuclear Science and Engineering

ABSTRACT

Accurate molten salt thermophysical properties are required to optimize the efficiency and safety of molten salt-based energy technologies. Unfortunately, existing thermal conductivity data for molten fluorides are plagued by large uncertainties. In addition, the data displays a curious positive temperature coefficient. Understanding of heat transfer in simple fluids suggests thermal conductivity should decrease as a function of temperature. Unaccounted-for contributions from convection and radiation may result in the observation of erroneous positive temperature coefficients. Interestingly, negative temperature coefficients have been observed in non-fluoride salts when measured using Transient Grating Spectroscopy (TGS). This work has shown that convection and radiation are insignificant for most TGS regimes. Therefore, it was hypothesized that TGS measurements of fluorides could finally resolve the discrepancies between theory and experiments.

The design and validation of a first-of-a-kind fluoride salt compatible TGS setup is presented. Demonstration of system performance is achieved through the acquisition and comparison of sound speed and thermal diffusivity data in lithium chloride (LiCl). The system has subsequently been used to measure the thermal conductivity of fluorides (FLiNaK). Results show a flat to slightly increasing thermal conductivity as a function of temperature ($0.7086 + 0.0002 \cdot T(^\circ C)$ +/- 0.08 W/m-K). In addition to thermal conductivity, sound speed data as a function of temperature ($2998 - 1.24 \cdot T(^\circ C)$ +/- 27 m/s) has also been obtained for the first time in FLiNaK. The use of accurate sound speed data in theoretical models of thermal conductivity provides better, but not complete agreement with the results from TGS.

The continued existence of a positive temperature coefficient poses more questions than it answers. Three new hypotheses are presented, namely, the influence of vapor pressure in multi-constituent salts, uncertainty surrounding existing heat capacity data, and the validity of neglecting diffusive contributions from theoretical models. Ultimately, this work suggests that fluoride molten salt thermal conductivity is weakly temperature-dependent. Reliable property data has far-reaching consequences for the size of heat exchangers, response to accident scenarios, or more broadly, the safe and efficient deployment of molten salt-based energy technologies.

Thesis Supervisor: Michael P. Short
Title: Class of '42 Associate Professor of Nuclear Science and Engineering

Thesis Reader: Antoine Allanore
Title: Associate Professor of Metallurgy

This Page is Intentionally Left Blank

Contents

List of Figures

1.   Background and motivation

1.1   The importance of accurate thermophysical property data

Molten salts are proposed within the designs of a variety of advanced energy technologies [1] [2] [3] [4]. Within nuclear power specifically, their potential use spans from the fuel and coolant in advanced fission reactors [1], to that of a tritium breeding blanket in some fusion designs [2]. Due to their stability under irradiation, negligible neutron absorption, and relatively low melting points and vapor pressures, fluoride salts make up the majority of these proposals [5]. However, despite the significant interest, material compatibility constraints have prevented fluoride salts from being accurately characterized. For multi-constituent salts, data for fundamental properties such as compressibility (β) are essentially non-existent [6], while thermal conductivity (λ) data has shown unexpected positive temperature coefficients [7] and large discrepancies between the results of different measurement techniques [8].
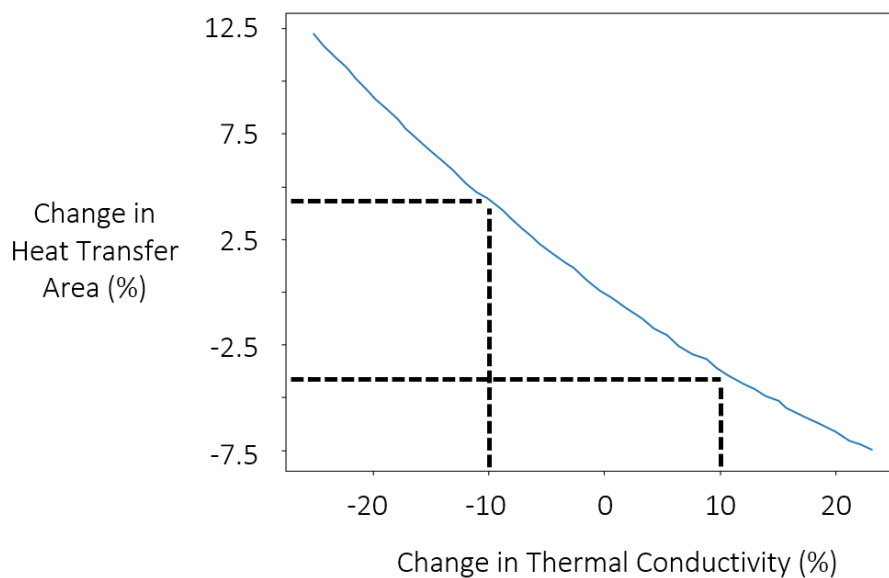
Figure 1. The effect of uncertainty in thermal conductivity on the required heat transfer area of a molten salt shell and tube heat exchanger. In this analysis, the reference case is a nitrate salt (λ = 0.46 W/m-K) operating at an average temperature of 590 K. [9]. Dashed lines are added to highlight the implication of +/-10% uncertainty for the salt's thermal conductivity [10].

Effective modeling of the safety and efficiency of these future systems hinges on the availability of accurate property data. For example, an important design parameter such as the size of a primary heat exchanger is intimately related to the value assumed for the salt's thermal conductivity. Large experimental uncertainties can force designers to turn to theoretical estimates of thermal

conductivity, which can be as much as 25% higher for commonly proposed coolant salts [8] [11]. Even when considering the estimated relative uncertainty for experimental thermal conductivity of ±10% [10], a roughly ±5% difference in the required heating transfer area can be observed (Figure 1). As an absolute value, a ±5% difference in the required heating transfer area may appear insignificant, however, as many reactors built today can exceed 4 GW thermal [12], the sheer size and cost of nuclear heat exchangers can be put into context.
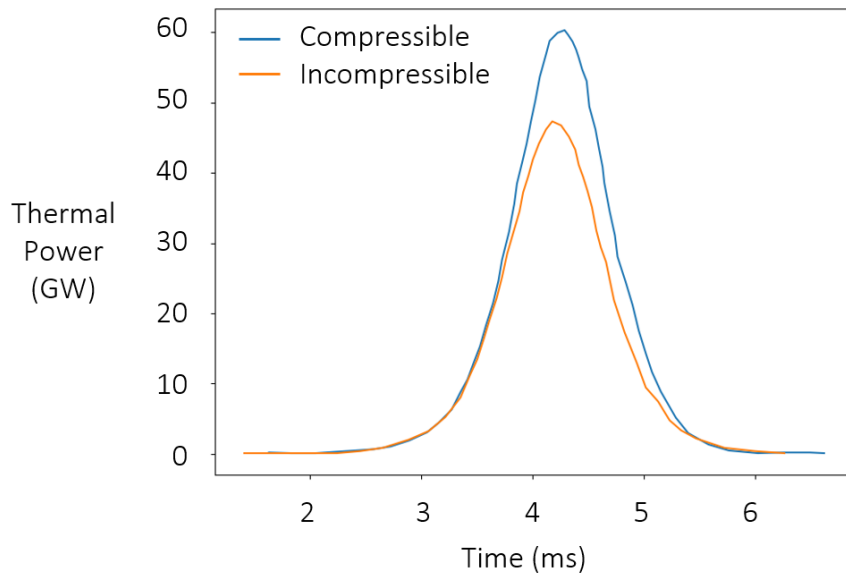
Figure 2. The influence of modeling fuel salts in a molten salt fast reactor as compressible vs incompressible during a super-prompt critical transient (500 pcm reactivity insertion) at reactor startup [10].

For compressibility, the lack of experimental data has led transient analysis software to assume that salts are essentially incompressible (sound speeds on the order of 4000 m/s) [13], allowing density changes in the salt to propagate instantaneously. Expansion of the salt with increasing temperature is expected to be an important feedback mechanism to control the rate of reaction in molten salt reactors [14]. Figure 2 shows the results of modeling fuel salts in a molten salt fast reactor (MSFR) as compressible vs incompressible during a reactivity insertion event [14], highlighting the non-conservative nature of the incompressible assumption.

Understanding the full implications of a 13 GW difference in peak power (47 vs 60 GW in Figure 2) during an accident scenario depends on the ability to model heat transport within the reactor, with additional salt properties such as thermal conductivity playing an important role in the accuracy of said models. Although the relative uncertainty of the salt's thermal conductivity has already been

discussed, of potential larger concern for accident scenarios is the evolution of the property as a function of temperature. To date, not even the sign of the temperature coefficient for fluoride molten salt thermal conductivity can be agreed upon.

1.2   The thermal conductivity temperature dependence debate
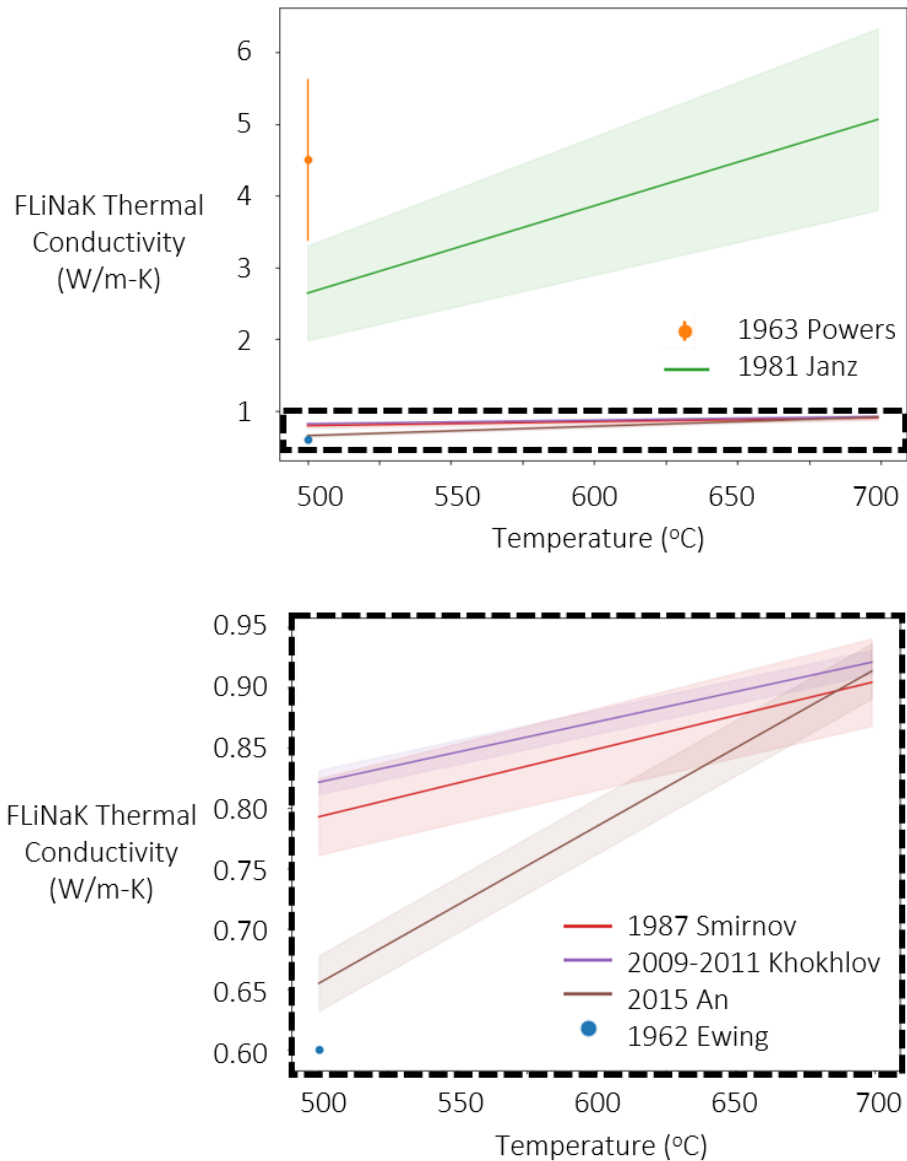
Figure 3. FLiNaK thermal conductivity data presented as a line of best fit and reported error (shaded region) when available for temperature dependent data [15] [16] [17] [18] [8]. Additional single temperature measurements are also included with the reported error when available [19] [20].

When looking at the thermal conductivity data (Figure 3) for a commonly proposed coolant salt like FLiNaK (the eutectic composition of LiF-NaF-KF [46.5-11.5-42 mol%]), the large discrepancy between different data sets is readily apparent. However, in addition to the data's spread, a more curious observation is that all the data indicates that thermal conductivity increases with increasing temperature, a fact that contradicts the established understanding of conductive heat transfer in simple fluids [21].
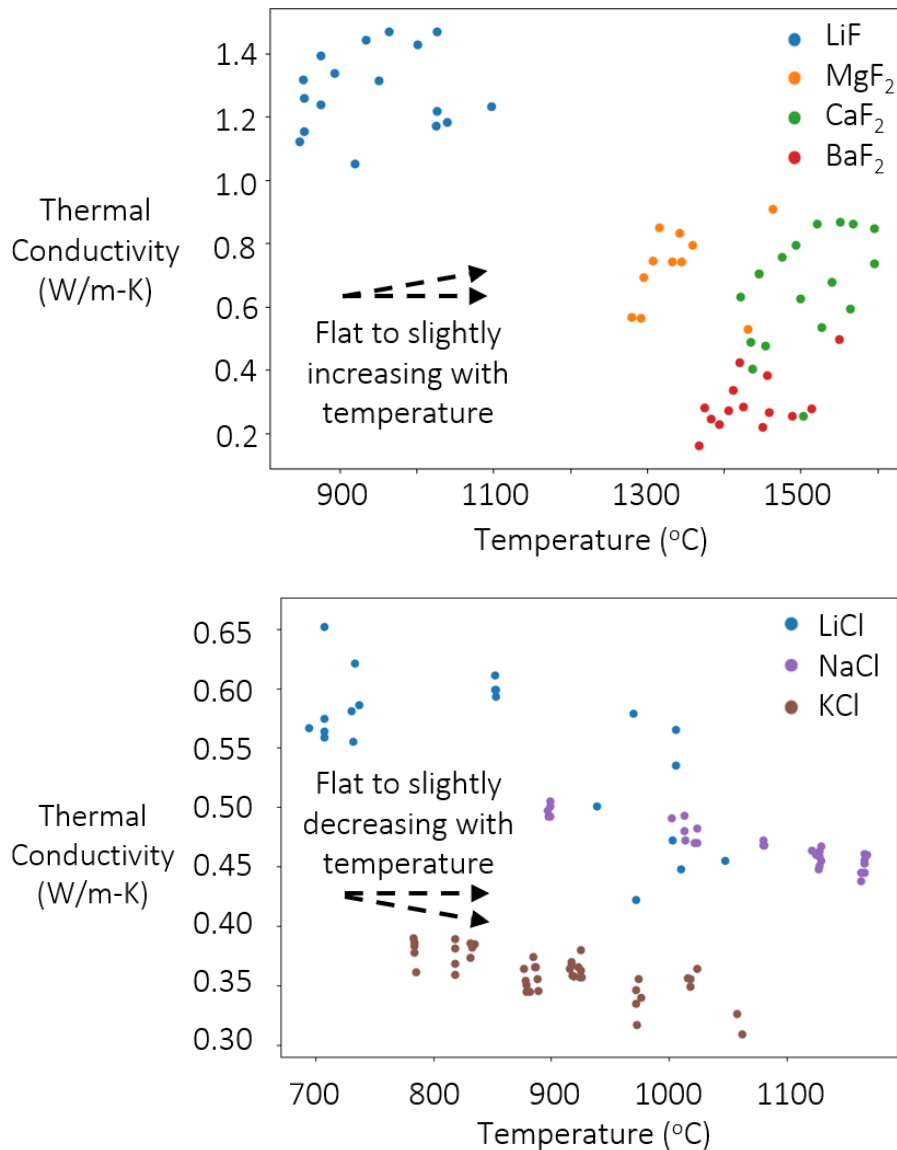
Figure 4. (Top) Experimental thermal conductivity data [22] [23] for a variety of single constituent fluorides that was deemed reliable for comparison to theoretical models [7]. (Bottom) A selection of single constituent chloride thermal conductivity data that shows a negative temperature coefficient [24].

Looking at more reliable data for single constituent halide salts (Figure 4), a negative slope can be seen to exist for chlorides. However, the limited fluoride data remains largely flat if not slightly increasing. To rectify the discrepancy between theory and experiments, the theoretical community has proposed that at the elevated temperatures of these measurements, experimental techniques often do a poor job at isolating a single mode of heat transfer [21]. As both radiation and convection are expected to increase with temperature, contributions from these modes that are unaccounted for could lead to erroneous observations of positive temperature coefficients in thermal conductivity measurements.

Although the mechanistic difference between chloride and fluoride molten salts is likely small, the inability of existing fluoride salt measurements to capture a negative coefficient is curious. The unexpected temperature dependence warrants review of the proposed models of thermal conduction to see if fluorides could indeed elicit a different temperature response than chlorides.

1.3   Theoretical models of molten salt thermal conductivity

Unlike solids and gasses, mechanistic understanding of thermal conduction in liquids is quite poor, with molten salts being no exception. One of the first attempts at a theoretical model of liquid thermal conductivity was proposed by Bridgeman [25], where liquids were assumed to have a quasi-crystalline structure with heat being transferred between neighboring atoms at the speed of sound (v). The resulting expression (Eq 1, where k_B is the Boltzmann constant) proposed that thermal conductivity was inversely proportional to the distance between atoms (l), in addition to its direct relation with the sound speed in the material.

$$\lambda = \frac{3k_B v}{l^2} \qquad\qquad \text{Eq 1}$$

The assumption of a cubic lattice allows for the spacing between atoms to be determined (Eq 2, where N_A is Avogadro's number) with knowledge of the liquid's density (ρ) and molar mass (M_W).

$$l = \left(\frac{M_W}{N_A \rho}\right)^{1/3} \qquad\qquad \text{Eq 2}$$

Although many molten salt properties have large uncertainties, molten salt density and its temperature dependance are well characterized, showing a strong positive thermal expansion coefficient [10]. Sound speed data in molten salt's is unfortunately much more limited [6]. However, knowing that the distance between atoms grows as the salt expands, indicates that salts will likely

become more compressible at higher temperatures, leading to a decrease in sound speed [26]. As density and sound speed are the only temperature dependent parameters in Bridgman's expression, thermal conductivity values determined via this method will undoubtedly possess a negative temperature coefficient.

At the time of the original article (1923), insufficient sound speed and density data were available for molten salts to evaluate the accuracy of Bridgman's model. However, the expression was later used to calculate the thermal conductivity of alkali nitrate salts, yielding values that were 17 to 30% higher than what had been observed experimentally [27]. The overestimation of Bridgman's model for nitrates was later determined to be even higher, as subsequent experimental measurements [28] yielded lower values than what was initially used for comparison. Alternatively, when the model is applied to some of the reliable chloride salt data [24], a slight underestimation is observed (Figure 5), providing a potential better comparison for fluorides.
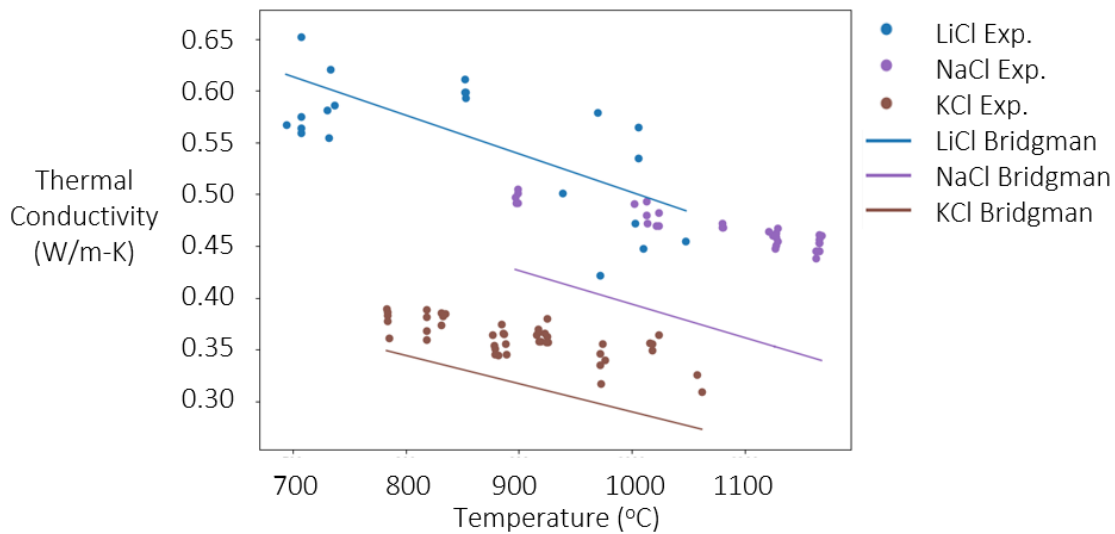
Figure 5. Single constituent chloride thermal conductivity data [24], along with a theoretical estimate based on Bridgman's model [25]. Sound speed data used in the model was taken from Bockris [26].

Building off Bridgman's model, subsequent attempts at describing thermal conductivity broke the property into two contributions [27], one from the interactions between vibrating atoms (λ_{vib}) and their neighbors, and the other from diffusive movement (λ_{diff}) of higher energy molecules into lower temperature regions.

$$\lambda = \lambda_{vib} + \lambda_{diff} \qquad \text{Eq 3}$$

To estimate the vibrational contribution, a picture was developed (Eq 4) where the flux of heat (q")
could be thought of as the product of the vibrational frequency (f) or number of collisions per
second, the difference in energy between neighboring atoms (atom spacing (l) multiplied by the
energy gradient in space (dE/dx)), and the number of atoms per unit area in an adjacent plane (n/l^2)
[29]. A factor of 2 was added to account for the fact that during one vibrational cycle, an atom will
interact with 2 planes of adjacent atoms.

$$q" = \frac{-2fn\left(\frac{dE}{dx}\right)}{l}$$

<div align="right">Eq 4</div>

Comparing the resulting expression (Eq 4) to Fourier's law (Eq 5), allows for determination of the
vibrational contribution to thermal conductivity (Eq 6, where dE/dT has been replaced by the
specific heat per molecule (C_V), and the constants have been consolidated into a)

$$q" = -\lambda\left(\frac{dT}{dx}\right)$$

<div align="right">Eq 5</div>

$$\lambda_{vib} = \frac{afC_V}{l}$$

<div align="right">Eq 6</div>

Numerous models used this general vibrational component form (Eq 6) as a jumping off point, with
differences primarily stemming from the potential used to estimate the vibrational frequency (ex.
harmonic oscillator [27], square well [30], Lennard Jones [29]). However, regardless of the frequency
relation, temperature dependencies continue to arise from the inverse relationship with the spacing
between atoms. Therefore, when considering the vibrational component alone, thermal conductivity
is expected to show a negative temperature dependence.

For the diffusive contribution, the derivation is largely similar to the vibrational component, however,
the vibration frequency has been replaced with a rate at which molecules will jump to an adjacent
location [29]. This frequency of movement can be expressed as the self-diffusion coefficient (D_m)
divided by a unit area (defined by the atomic spacing (l^2)), resulting in Eq 7.

$$\lambda_{diff} = \frac{aD_mC_V}{l^3}$$

<div align="right">Eq 7</div>

For the majority of models, the diffusive contribution is assumed to be negligible compared to the
vibrational component, having been calculated to represent less than 5% of the total thermal

conductivity for molten sodium nitrate and sodium chloride [27]. The validity of this assumption will be discussed in more detail in Section 5.3, however, when the diffusive component is ignored, estimated thermal conductivity values using this approach where 10 to 40% higher than what was observed experimentally [21].

Numerous other models of molten salt thermal conductivity have been developed with many containing similar roots or pulling directly from the fundamental picture outlined above [7]. Alternative attempts have relied on corresponding states [31], or semi-empirical correlations [32], where models depend on the accuracy of existing data, providing minimal predictive capability.

1.4   Predicting molten salt thermal conductivity using molecular dynamics

In addition to theoretical models, several attempts have been made at extracting molten salt transport properties from molecular dynamics simulations [33] [34] [35]. For thermal conductivity, this can be performed by using either equilibrium (EMD) or non-equilibrium molecular dynamics (NEMD). In the case of NEMD, one method is to apply heat flux boundary conditions across a simulation cell. The resulting temperature gradient permits thermal conductivity to be determined through comparison to Fourier's law [36]. Alternatively, temperature boundary conditions can be specified, leading to the formation of an artificial temperature gradient. The use of temperature-based boundary conditions requires more intricate algorithms (Ex. Evans-Gilian [37]) to extract the intrinsic thermal conductivity and has seen limited use beyond single constituent salts [35]. For equilibrium methods, Green-Kubo formulations (Eq 8 and Eq 9) allow thermal conductivity to be derived from the microscopic fluxes in energy (j_e) and charge (j_Z) that occur from spontaneous fluctuations at thermal equilibrium [38].

$$\lambda = \left(L_{ee} - \frac{L_{ze}^2}{L_{zz}} \right) \frac{1}{T^2}$$
Eq 8

$$L_{\alpha\beta} = \frac{1}{3Vk_B} \int_0^\infty \langle j_\alpha(t) j_\beta(0) \rangle$$
Eq 9

Both methods (EMD and NEMD) are subject to size constraints, as the system must be large enough to accurately represent scattering of different long range vibrational modes of heat transfer. However, NEMD is additionally constrained by the unrealistic possibility that a vibrational mode will not scatter as it propagates between the hot and cold boundaries [36]. Reduced system size effects

have led EMD and Green-Kubo based methods to be the predominant choice for estimating molten salt thermal conductivity [34] [33].
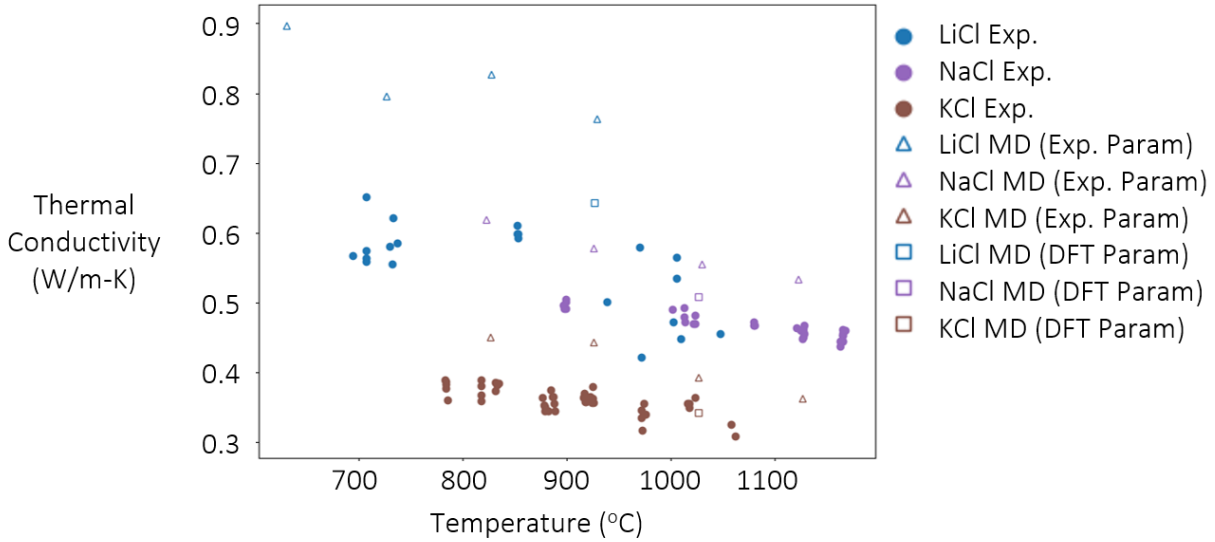
Figure 6. Single constituent chloride thermal conductivity data [24], along with estimates from two sets of molecular dynamics calculations, one using a potential parameterized using experimental data (Exp. Param) [33], and the other a potential parameterized with DFT simulations (DFT Param) [39].

To obtain adequate statistics, EMD simulations for molten salts have been conducted on hundreds of atoms and have simulated the system over several nanoseconds using femtosecond time steps [34] [33]. The scale of these simulations necessitates the use of classical molecular dynamics where an interatomic potential must be defined. For molten salts, a common class of potentials that has been used is known as Born-Mayer-Huggins-Fumi-Tosi (BMHFT, Eq 10), where a sum of coulomb interactions (first term Eq 10, q is ionic charge, r is interatomic distance), repulsive forces due to the overlap of electron clouds (second term Eq 10, A is the Pauling factor, σ is the crystal ionic radius, ρ is the hardness parameter), dipole-dipole (third term Eq 10) and dipole quadrupole (fourth term Eq 10) dispersion interactions are used [40]. Potentials of this kind require parameterization, where many of the model's variables (Ex. C_{ij}, D_{ij}, and b) are adjusted to reproduce experimental properties. For molten salts, single constituent solid phase data [41] [42] is often used for parametrization.

$$U_{ij}(r) = \frac{q_i q_j}{r} + A_{ij} b e^{\frac{\sigma_i + \sigma_j - r}{\rho}} - \frac{C_{ij}}{r^6} - \frac{D_{ij}}{r^8} \qquad \text{Eq 10}$$

As an alternative to the use of experimental data, parametrization of potentials has also been performed by fitting the expressions to the results of first-principles or density functional theory (DFT) calculations [39]. A comparison of EMD obtained thermal conductivity results for both potential parameterization methods to experimental data for single constituent chlorides is shown in Figure 6. Results highlight that in general, molecular dynamics will tend to overestimate the thermal conductivity when compared to experiments, however, the work that has been done on DFT parameterized potentials looks to offer good agreement for single constituent chlorides [39].

The success of single constituent chloride simulations (Figure 6) have led researchers to pursue MD based methods as a predictive tool for salts that have large uncertainties in their experimentally obtained thermal conductivity, such as FLiNaK.
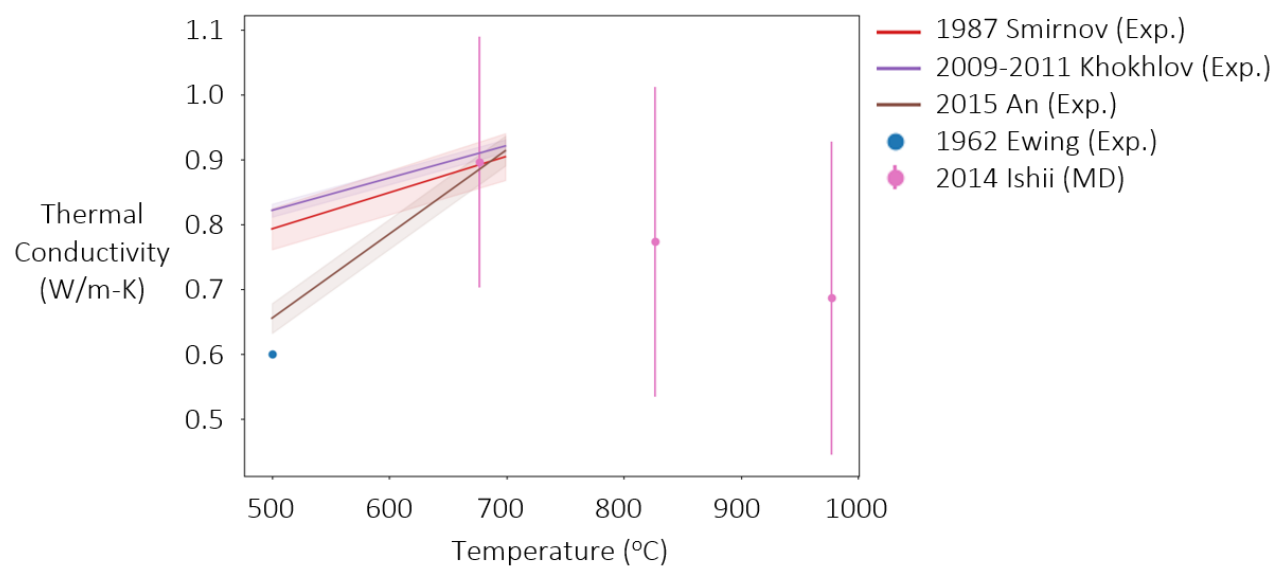
Figure 7. A selection of experimental FLiNaK thermal conductivity data (Exp.) [15] [16] [17] [18] [8]. along with estimates from a DFT parameterized molecular dynamics simulations (MD) [34].

A comparison of DFT parameterized MD simulations and previous experimental data for FLiNaK (Figure 7) highlight a continued offset in magnitude, however, as the validity of the experimental results is in question, this discrepancy must be taken with a grain of salt. Regardless of the magnitude of the EMD results, the observation of a negative temperature dependance reinforces the consensus from the theoretical community. As molten salts, and in particular alkali metal fluorides, are expected to have simple structures, their thermal conductivity should decrease with temperature, similar to what has been observed for other halide [24] and nitrate salts [28]. This

consensus shines further light on previous attempts at determining fluoride salt thermal conductivity experimentally, and why they have not been able to capture the expected temperature dependance.

1.5   Previous experimental measurements of fluoride molten salt thermal conductivity

Thermal conductivity measurement techniques can generally be broken down into two classes: steady state and transient. For steady state methods, producing a small but constant temperature difference across the material of interest, allows for elimination of time derivatives from the governing equation (transforming the heat equation into Laplace's equation). Accurate knowledge of the temperature at the boundaries, geometry, and supplied power, allow for subsequent determination of the material's thermal conductivity without consideration for the sample's density and heat capacity [43]. Subdivision of steady state techniques comes primarily from the geometry employed. Parallel plates [15] is one example, where the salt is sandwiched between two flat surfaces, with the top heated to minimize convective contributions. Alternatively, the salt can be placed in between concentric cylinders [16], with the central cylinder acting as the heat source.

Minimizing convection is critical in all thermal conductivity measurement techniques, however, steady state methods have particular challenges related to "edge" effects, where heat is lost at the boundaries, causing temperature deviations and the potential onset of convection [43]. Of the two steady state methods described, concentric cylinders has produced the more reliable results for FLiNaK (0.8 to 0.9 W/m-K) [16] [17] [18] albeit with a strong positive temperature coefficient. Attempts at using parallel plates have yielded order of magnitude higher values (2.5 to 5 W/m-K) [20] [15], indicating the likely presence of additional modes of heat transfer.

For transient techniques, measuring a temperature response as a function of time following a short heating duration allows for determination of the material's thermal diffusivity. The resulting values can be converted to thermal conductivity with knowledge of the salt's heat capacity and density, creating a reliance on the accuracy of other salt property data. Transient techniques that have been employed with respect to fluoride molten salts include Laser Flash Analysis (LFA) [8] and Transient Hot Wire methods [44]. LFA was primarily developed for opaque solid samples, necessitating the use of intricate crucible designs when applied to molten salt measurements. In LFA, one side of the salt's container is subject to a heat pulse from a laser, while the opposite side's temperature is monitored with an infrared detector. LFA results for FLiNaK show a strong positive temperature dependence, increasing by almost 40% when going from 500 to 700°C [8]. Despite the inexplicable

temperature coefficient, as of 2018, LFA was the recommended technique by the Department of Energy for assessing molten salt thermal conductivity [45]. The unique errors associated with adapting LFA for molten salts have been investigated in this thesis and are detailed further in Section 4.3.

For hot-wire methods, a thin wire submerged in the salt can act as both a transient heat source and thermocouple. The relationship between electrical resistance and temperature for the wire material (ex. platinum) is typically well known, and measuring the resistance provides very little additional heating. The transient hot wire method is one of the techniques that has been deemed reliable by the theoretical community [7], having produced largely temperature independent nitrate salt thermal conductivity data [46]. Hot wire measurements that have been obtained in FLiNaK were performed at a single temperature and were much lower than previous measurements and estimates (0.22 W/m-K) [44], indicating the likely presence of setup-specific experimental error.

Designing compatible techniques and setups for the highly corrosive nature of fluoride salts is by itself challenging. However, the fact that FLiNaK offers minimal absorption for infrared wavelengths [47] allows confounding radiative heat transfer through the salt to easily take place. Techniques that rely on heating and measuring salt contacted surfaces are likely to be plagued by contributions from radiation. As the salt density decreases with increasing temperature, this contribution will continue to grow as less radiation is attenuated in the salt itself. One way to get around this issue is to create and measure temperature differences directly within the salt, a mechanism employed by what is known as transient grating spectroscopy.

1.6   Transient grating spectroscopy

Transient grating spectroscopy (TGS) also known as forced Rayleigh scattering, is one of the only techniques to have shown a negative temperature coefficient for the thermal conductivity data of molten halide salt systems [24] [48] [49].

In an embodiment relevant to molten salt property measurements (Figure 8), TGS works by crossing two parallel polarized "pump" lasers within a material which is mostly, but not entirely, optically transparent at the pump laser wavelength (λ_P). Some absorption is needed to create the "transient grating," whereby constructive and destructive interference within the overlap of the two beams yields regions of high and low light intensity, characterized by a spacing $d = \lambda_P/(2\,sin(\theta/2))$ (where is θ is the crossing angle of the two beams). Absorption of the light, followed by thermalization and thermal expansion, results in the formation of a transient density and temperature grating directly

within the molten salt sample. Over longer timescales (μs to ms), relaxation of the grating back to equilibrium is governed primarily by thermal conduction, however, over short timescales (100s of ns), acoustic oscillations can be observed, allowing for determination of the salt's sound speed in addition to thermal diffusivity. Signal acquisition is achieved by diffracting a continuous "probe" laser off the density grating and into a photodiode. In practice, property information is obtained by comparing the time-dependent diffracted signal intensity (I_D) to an equation in line with the governing hydrodynamic theory (Eq 11) [50].
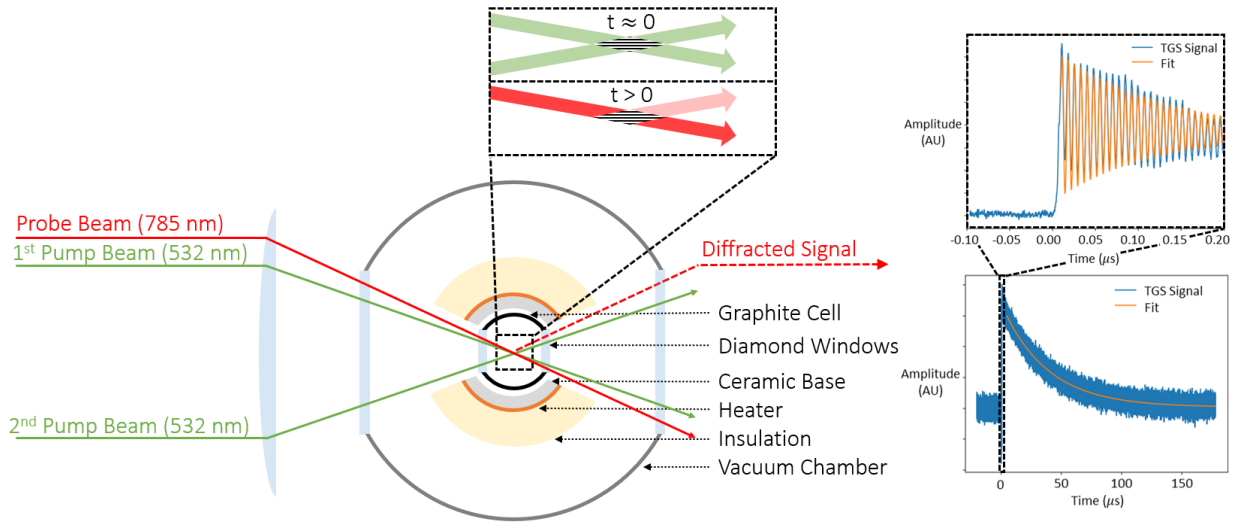
Figure 8. A conceptual top-down view of transient grating spectroscopy when operated in transmission. Pump and probe wavelengths, as well as details related to sample containment, are specific to the system implemented in this thesis and will be discussed further in Section 2. Example long and short timescale signals have been obtained in FLiNaK and will be discussed further in Section 4.

$$I_D = \left[C_1 \left(e^{-C_2 \left(\frac{2\pi}{d} \right)^2 t} - e^{-C_3 \left(\frac{2\pi}{d} \right)^2 t} \cos \left(C_4 \left(\frac{2\pi}{d} \right) t \right) \right) \right]^2 \qquad \text{Eq 11}$$

In Eq 11, C_i values are variables to be used in a non-linear, least-squares fitting procedure, with C_2 and C_4 physically representing the thermal diffusivity and sound speed, respectively. C_1 represents the total signal amplitude, controlled by the pump and probe laser powers along with the optical absorption characteristics of the salt, while C_3 represents the damping parameter of the sinusoidal acoustic standing wave, a rarely used but potentially useful property that is discussed further in Section 6.

Although not implemented in the previous TGS molten salt efforts, a heterodyne configuration [51], where a undiffracted reference beam is aligned with the diffracted signal can also be employed. Interference between the two beams allows for a substantial increase in signal strength (I_S), described mathematically by Eq 12 where I_R and ϕ are the reference beam intensity and the phase difference between the diffracted and reference beams, respectively. As I_R is normally much greater than I_D, the relevant signal becomes proportional to the square root of I_D, and thus the square root of Eq 11 must be used when fitting the obtained signals.

$$I_S = I_R + I_D + 2\sqrt{I_D I_R}\, cos\,\phi \qquad\qquad \text{Eq 12}$$

1.7   Central hypothesis

Despite the previous success of TGS based molten salt measurements, until now it has never been performed successfully in fluorides, primarily due to material compatibility constraints. In the previous experimental setup for chlorides, a quartz cell was used to contain the molten salt [24]. The authors noted that both quartz and sapphire corroded rapidly when exposed to fluorides (LiF and KF), eliminating the ability to pass lasers through the salt sample [52]. Building on this observation, the central hypothesis at the outset of this thesis was that by designing a fluoride salt compatible TGS setup, the discrepancy between experimental and theoretical estimates of fluoride salt thermal conductivity could finally be rectified. The remaining sections detail these efforts, and shine light on the need for new explanations as to why experimental measurements, or theoretical estimates, cannot capture the correct temperature dependance for fluoride molten salts.

2.   Design and validation of a fluoride salt compatible setup

Parts of this chapter have been reproduced from S. G. Robertson and M. P. Short, "Design and performance of a molten fluoride salt-compatible optical thermophysical property measurement system," Review of Scientific Instruments, 92, 2021, with the permission of AIP Publishing

2.1   System design overview
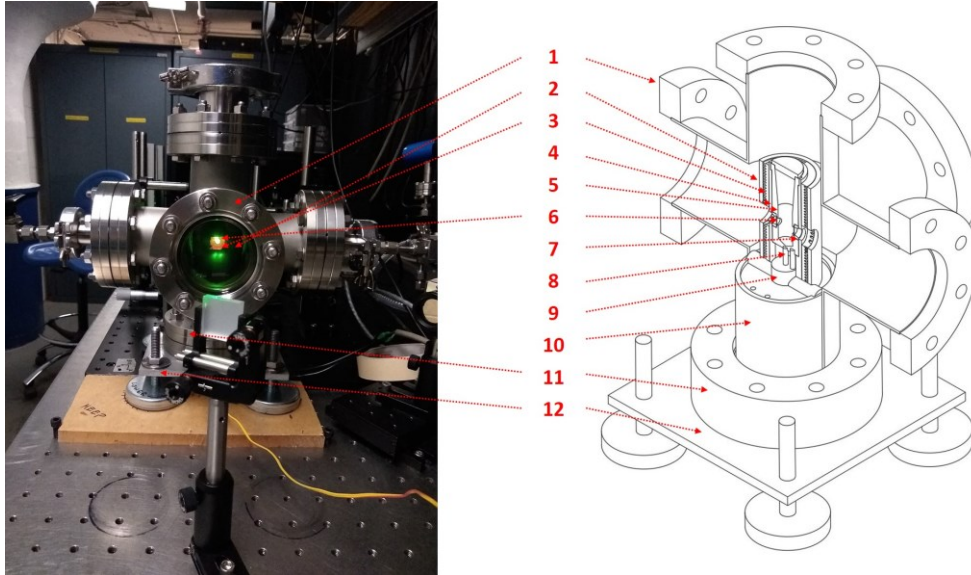
Figure 9. Fluoride salt compatible measurement chamber shown in operation (left) and as a sectional CAD drawing (right). (1) External vacuum chamber, (2) ceramic fiber insulation, (3) boron nitride heater base, (4) graphite sheath, (5) graphite cell, (6) diamond windows, (7) graphite rings, (8) K-type thermocouple, (9) Macor alignment key, (10) Macor stage, (11) feedthrough flange, and (12) chamber stand.

To facilitate the use of TGS for evaluating molten salt thermophysical properties, a fluoride-salt-compatible optical measurement chamber has been designed and tested. Figure 9 shows an image of the chamber in operation (left) and as a CAD drawing cutaway (right). The primary feature of the design is the salt container, which consists of a high-density graphite cell with two chemically vapor deposited (CVD) diamond windows oriented 180° from one another. To minimize geometrical changes as a function of temperature, graphite was chosen over alternative salt-compatible cell materials such as nickel due to its lower thermal expansion coefficient [53] [54]. Although adverse reactions such as carbide formation can occur for salts in graphite containers [55], short

measurement times along with pre- and post-composition analysis should mitigate and quantify its impact, respectively.

To facilitate salt containment and transmission of the lasers, CVD diamond acts as the only known visibly transparent materials capable of sustained operation in fluoride salts [56]. However, as shown in Figure 10, the percentage of transmission for diamond decreases with wavelength throughout the visible and UV range. Although limited absorption spectra exist for halide salts, in general primary salt constituents absorb light preferentially within UV wavelengths [57]. Small quantities of transition metal halides ($\approx$ 1 wt. %) are therefore added to the salt to increase absorption within the visible range. Windowless cell designs that rely on the salt's surface tension [58] were avoided due to concerns over changes in the curvature of the salt-vapor interface as functions of temperature and composition.
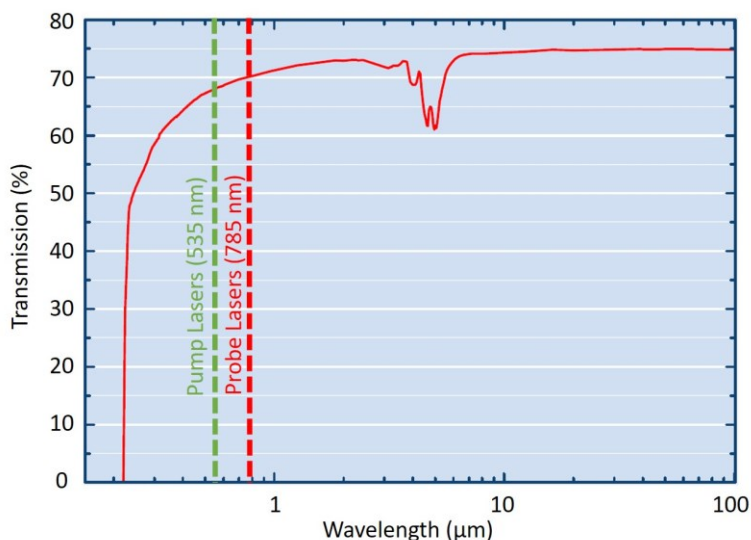
Figure 10. Transmission (%) vs. wavelength for CVD diamond overlaid with the relevant wavelengths of the pump and probe beams used in the TGS setup. This figure has been adapted from a publicly available commercial brochure [31] with permission from the author and supplier of the diamond windows used in this work, Diamond Materials - Advanced Diamond Technology.

Building on the work of Toth et al. [56], the diamond windows are held in place by light pressure from a graphite ring and external sheath (Figure 11). The internal diameter of the sheath is slightly tapered (not shown in Figure 11), and the thickness of the graphite rings is such that full pressure is applied to the windows only once the components are fully assembled. Larger dimensions of the cell (ID 12 mm) and windows (OD 7 mm) were chosen to simplify alignment of the lasers and to

reduce influence from the surrounding cell walls on grating formation and decay [59]. However, to accommodate this design choice, larger salt volumes on the order of 3.2 cm^3 are required during a measurement.
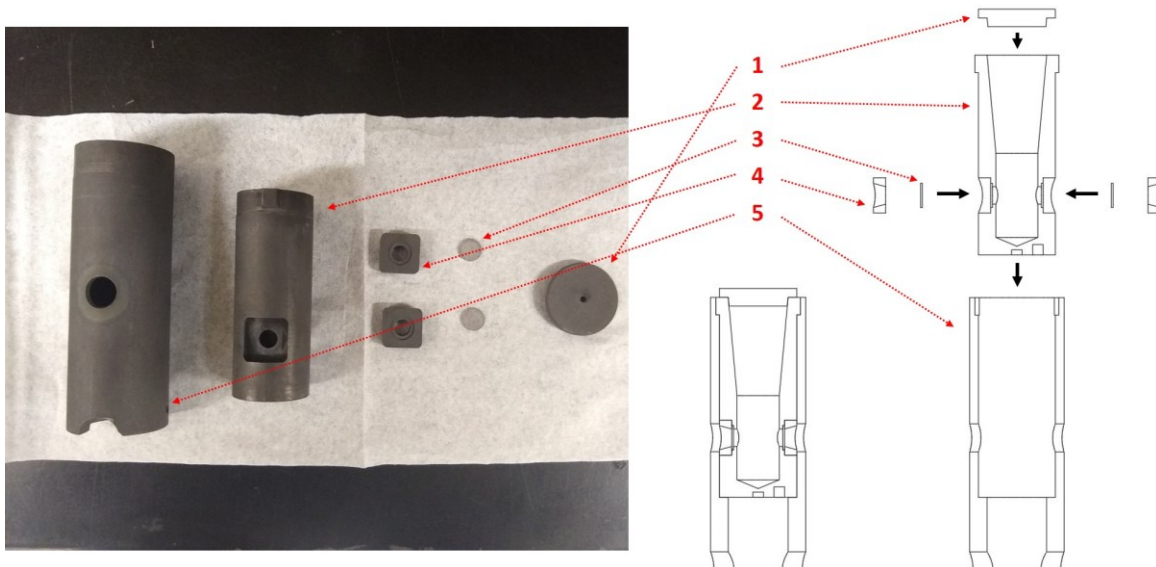
Figure 11. Salt container shown dissembled on the benchtop (left) and as a blowout CAD model (right). Solid arrows indicate the movement direction required for a component during assembly. (1) Graphite lid, (2) graphite cell, (3) diamond windows, (4) graphite rings and, (5) graphite sheath.
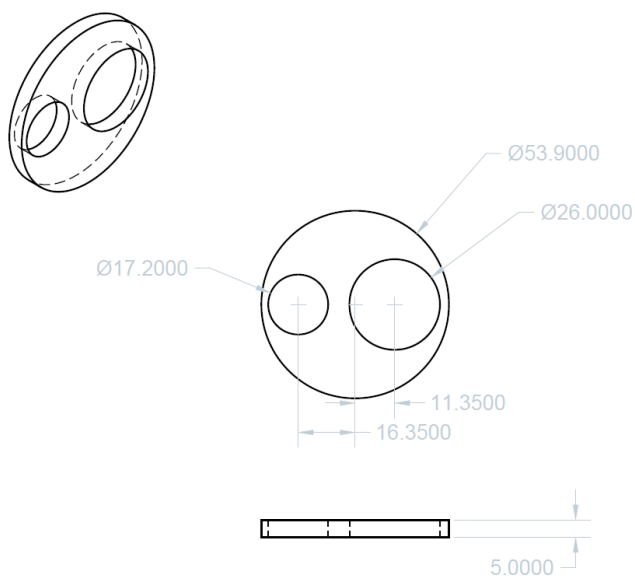
Figure 12. Custom graphite stage to remove salt from the graphite cell following a measurement. Dimensions have been reported in mm with the larger opening accommodating the bulk of the cell and the smaller opening being used for the lid.

To remove the salt from the graphite cell, a custom graphite stage (Figure 12) was designed to fit inside a tapered glassy carbon crucible (GAT 34, HTW Hochtemperatur-Werkstoffe GmbH). Differences in radii between the inner cell and sheath allow the cell to stand firmly upside down on the stage after the inner cell is pushed slightly out of the sheath. Within a furnace inside an argon glove box, the cell containing crucible can be raised above the salt's melting point, allowing salt to flow into the space below the stage. As the salt does not wet the glassy carbon, it can then be easily extracted for composition analysis or reloaded into the cell for additional measurements. Multiple stage materials were tried, with nickel and glassy carbon proving inadequate due to high thermal expansion and machinability respectively.

Although the stage has worked well for extracting the bulk of the salt from the cell, additional cleaning is performed to remove any residual material prior to a subsequent measurement. Current cleaning procedures rely on sonicating the cell withing an aluminum nitrate aqueous solution, with subsequent sonication in deionized water followed by drying prior to reloading the cell with salt.
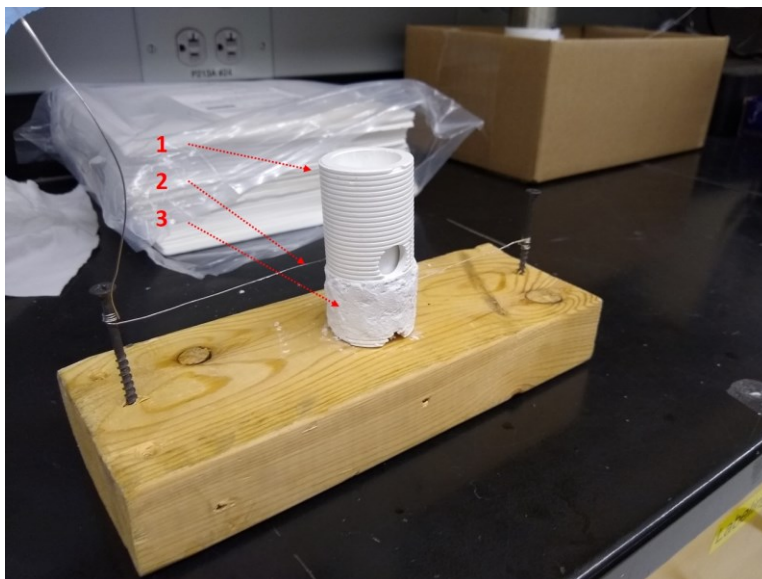
Figure 13. Chamber heater during construction, showing the grooved boron nitride base (1), Nichrome wire (2), and adhesive alumina paste (3).

To bring the salt to the desired temperature range (500 to 700°C) for measurements, a heater design similar to that proposed by Raptis et al. [60] has been used, where a grooved boron nitride base wrapped in Nichrome wire sits external to the salt container (Figure 13). The Nichrome wire is adhered to the base using a thermally conductive alumina paste, which is then wrapped further in several layers of ceramic fiber insulation (3 mm total thickness).
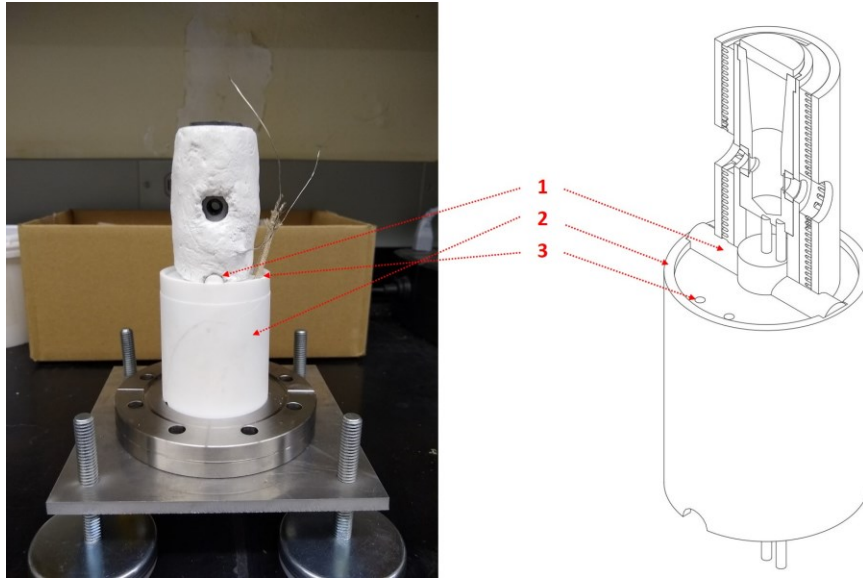
Figure 14. Benchtop image (left) and sectional CAD drawing (right) of the chamber's heating assembly positioned on top of the Macor stage. (1) Macor alignment key, (2) Macor stage, and (3) power lead feedthroughs.
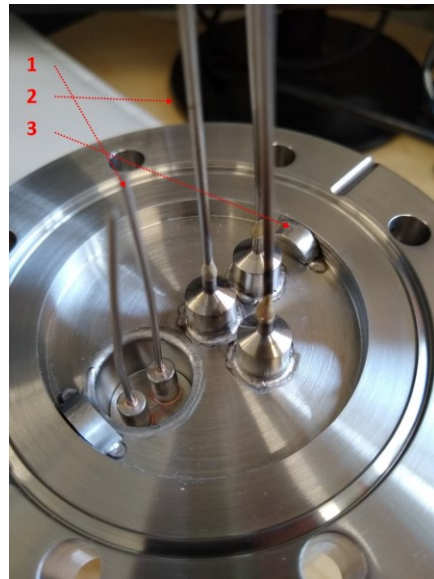
Figure 15. The chamber's bottom feedthrough flange, showing the heater's power leads (1), thermocouples used for temperature profile assessment (2), and half-circle alignment mechanism (3).

A half-circle cutaway from the base of the heater and graphite cell allows for alignment of the assembly on top of a Macor stage (Figure 14). The low thermal conductivity of Macor, along with

the stage's hollow cylinder design, allow the heating assembly to be elevated into the center of the larger vacuum chamber, while limiting the temperature of the bottom flange.

The external vacuum chamber is designed as a six-way cross, distancing all flanges from the internal heating assembly while providing ample surface area for external convective cooling. The two flanges aligned with the diamond windows are standard borosilicate glass viewports, with the remaining two horizontal flanges facilitating vacuum and gas hookup (Figure 9). Although the system is designed to operate under vacuum, an argon gas line is provided to purge the system following addition and removal of a sample, achieved through removal of the chamber's top flange. The bottom flange acts as a feedthrough for thermocouples and heater power leads, as well as provides an alignment mechanism for the heating assembly within the larger chamber (Figure 15). Further details of the chamber design can be found in the CAD model provided in the supplemental information in the GitHub repository for this section [61].

2.2   Assessment of the system's thermal performance

To characterize the thermal performance and validate the chamber design for molten alkali halide salt thermophysical property evaluation, LiCl was used as a first test material. LiCl has some of the more accurate thermal conductivity and sound speed data openly available [26] [24], while also having one of the lowest melting points of any of the single constituent halide salts (605°C). Future measurements in fluoride salts will be primarily concentrated between 500 and 700°C, necessitating the use of a test material within this range

Using a variable 60 V DC power supply, internal thermocouple temperatures in excess of 700°C were observed. The vacuum levels for the chamber at these temperatures is less than 100 mTorr. Due to material compatibility constraints, internal thermocouples are embedded within the graphite cell below the base of the salt (Figure 9). To better understand the temperature profile within the salt itself, a model of the chamber was constructed using COMSOL Multiphysics [62]. As there is significant uncertainty regarding the emissivity of many of the components used in the chamber, emissivity values were taken as fitting parameters for the model. Hand-held measurements of the external flange temperatures and readings from the internal thermocouples at three different power levels (103.2 W (48 V), 107.3 W (49 V) and 112.0 W (50 V)) were used as reference points. Model predictions within +/- 10°C of the flange measurements were deemed adequate, while maximum allowable deviation from internal thermocouples was set at +/- 2.5°C.

Table 1. Comparison of experimental temperature measurements and predictions from a fitted COMSOL model for several chamber reference points. Flange temperatures were evaluated at the base of the flange, where contact occurs with the chamber's piping.

Power	Central T/C (°C)		Bottom Flange (°C)		Top Flange (°C)		Viewport Flange (°C)	
(W)	Exp.	COMSOL	Exp.	COMSOL	Exp.	COMSOL	Exp..	COMSOL
103.2	628.8	630.1	63.3	58.0	98.7	97.6	54.8	53.5
107.3	641.0	640.9	66.6	58.9	107	100.5	56.3	54.6
112.0	653.0	652.8	68.3	59.9	112.9	103.7	58.8	55.9
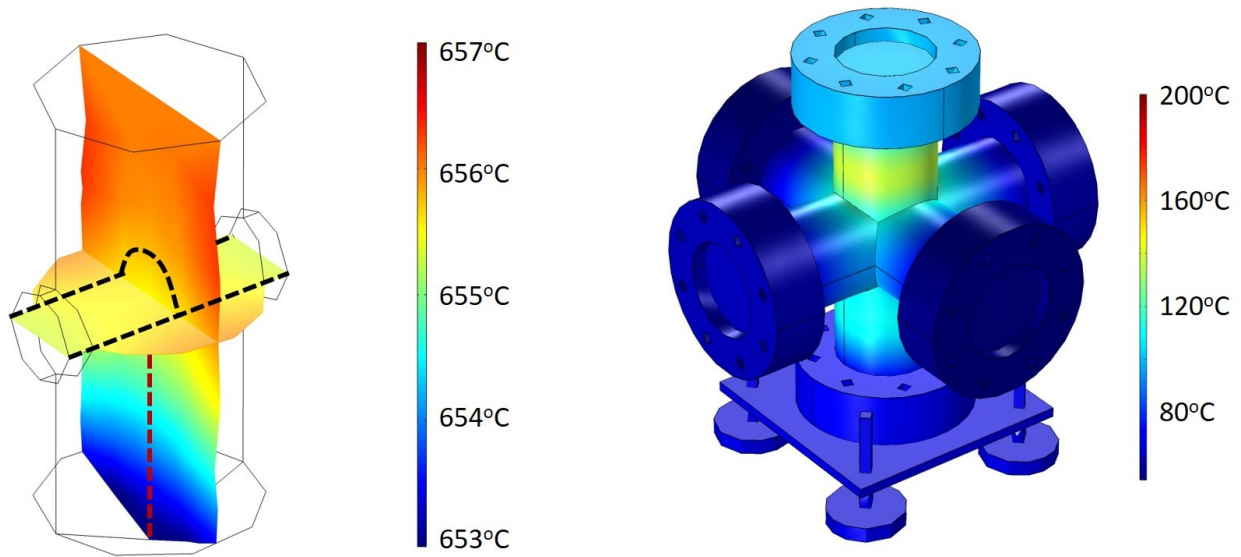
Figure 16. COMSOL predicted temperatures for both the salt volume (left) and external chamber (right) for a heater power of 112 W (50 V). Black and red dashed lines highlight the salt volume that will be exposed to lasers and the temperature difference between the salt and internal thermocouples, respectively.

Using the fitted model, the temperature difference between the internal thermocouples and the relevant salt volume was seen to be roughly 3°C (Figure 16). This temperature difference provides an adjustment to be used when reporting future measurement temperatures based off the internal thermocouple readings. Salt temperatures within the lasers path are expected to range +/- 0.5°C (Figure 16). As K-type thermocouples at these temperatures have uncertainties on the order of +/- 5°C, combining this with the range in the salt gives the total uncertainty of the measurement temperature (+/- 5.5°C). Both the axial and radial temperature profiles of the salt were seen to be

relatively constant across the power levels assessed in the model (Table 1). It is important to note that the model treats the salt as transparent to radiation and does not model natural convection within the salt. As a result, the model is expected to provide an upper bound of the temperature gradients present, and thus only a rough estimate of the offset from the thermocouple.

To provide a further check of the model's accuracy, a comparison between the melting point of LiCl and the internal thermocouple reading when the lasers are able to pass through the salt (not possible when solid) was performed. The heating rate of the salt through the melting point was dropped to roughly 0.5°C/min to allow temperature profiles to reach a quasi-steady state. Visibility of the lasers through the salt occurred for an internal thermocouple reading of 600°C. Using the models 3°C adjustment and +/- 5.5°C uncertainty gives a predicted salt temperature of 603 +/- 5.5°C. As this result encompasses the 605°C reference melting temperature of LiCl, the 3°C adjustment and +/- 5.5°C range was adopted for reporting all future chamber temperature measurements in LiCl. Full details of the COMSOL model can be found in the supplemental information available in the data repository for this section [61].

2.3   Thermophysical property evaluation of molten LiCl

Following characterization of the chamber's thermal performance, validation of the design for thermophysical property evaluation was carried out. Approximately 1 wt. % of $NiCl_2$ ($\geq$ 99.99% metals basis, Beantown Chemical) was added to LiCl ($\geq$ 99.9% metals basis, Alfas Aeser) to increase absorption within the 532 nm wavelength pump beam. This quantity of added $NiCl_2$ was deemed low enough by previous groups to not significantly affect thermophysical property results [24]. Although this is adequate for system validation and comparison to literature results, further trials at various concentrations were performed when assessing the accuracy of fluoride salt measurements (Section 4). Prior to settling on the use of $NiCl_2$, five other dye candidates were attempted, $FeCl_2$, $MnCl_2$, $CoCl_2$, $CrCl_2$ and $K_2Cr_2O_7$. At 1wt%, $FeCl_2$ and $MnCl_2$ offered only weak absorption of the 532nm pump beam, while $CoCl_2$ and $CrCl_2$ showed the adverse effect of strongly absorbing the 785nm probe. $K_2Cr_2O_7$ which was used by previous groups for the acquisition of single constituent chloride data [24], decomposed upon heating in the salt, showing signs of green chromium oxide formation. As minimal information was provided by previous groups on salt preparation, the use of $K_2Cr_2O_7$ was abandoned in favor of the $NiCl_2$.

Samples were prepared by prebaking the constituents separately in glassy carbon crucibles at 700°C for 1 hour under an argon atmosphere. The constituents were then combined in relevant

proportions (1 wt% $NiCl_2$) and baked again at 700°C for 1 hour prior to loading into the graphite cell. The cell was then transferred to the vacuum chamber (< 1 min of air exposure) and baked at 300°C for 12-14 hours under vacuum to remove any remaining water content that could have been introduced during loading. The bakeout time selected is largely arbitrary, as vacuum levels typically plateau after a few hours. However, for convivence, a 12-hour bakeout allows for alignment and setup the night before, with measurements taking place the following morning.

To better resolve the different timescale phenomena, signal acquisition was broken into two separate components, "short" and "long," defined by the use of a 100ns and 10µs timebase, respectively. Separate detectors were employed for the different timebases, with the "short" signal being obtained using a Hamamatsu C5658 and the "long" using a Newport - New Focus 1801. Raw signals for the two timescales can be seen in Figure 18. The use of an AC coupled detector (Hamamatsu C5658) proved inadequate for acquisition of the long timescale decay present in molten salts and other liquids. The frequency cutoff associated with AC detectors limits the ability to measure slowly changing light levels, leading to an erroneous signal shape, where a dip below the baseline is observed (Figure 17).
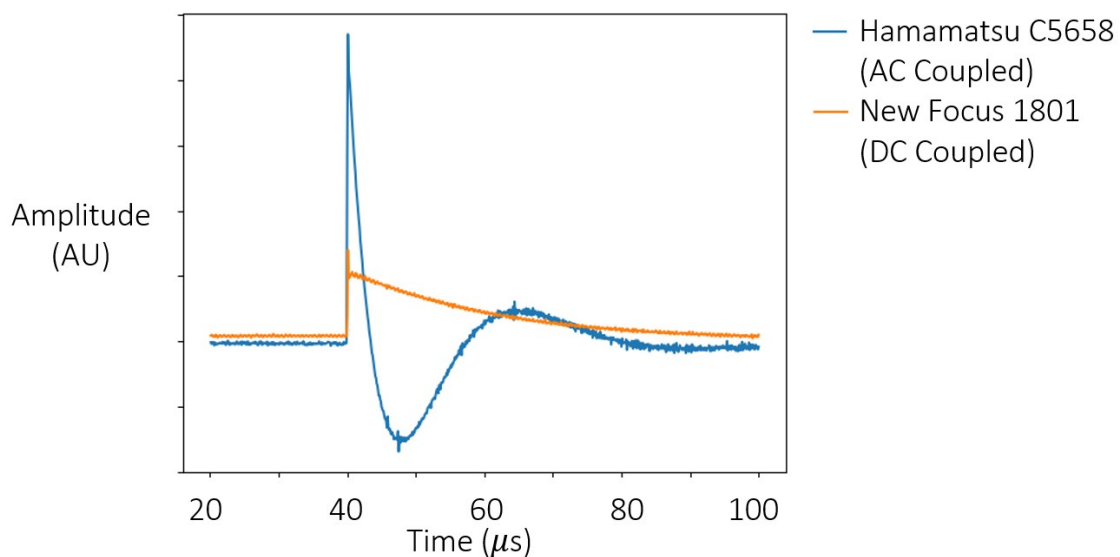
Figure 17. Comparison of a long timescale signal obtained using Hamamatsu C5658. (AC Coupled) and Newport - New Focus 1801 (DC coupled) detectors. Signals were obtained in an aqueous solution with a ferroin dye used to absorb adequate pump light. Aqueous ferroin solutions have led to much higher signal strengths than molten salts, however, the same relative signal shape is observed.
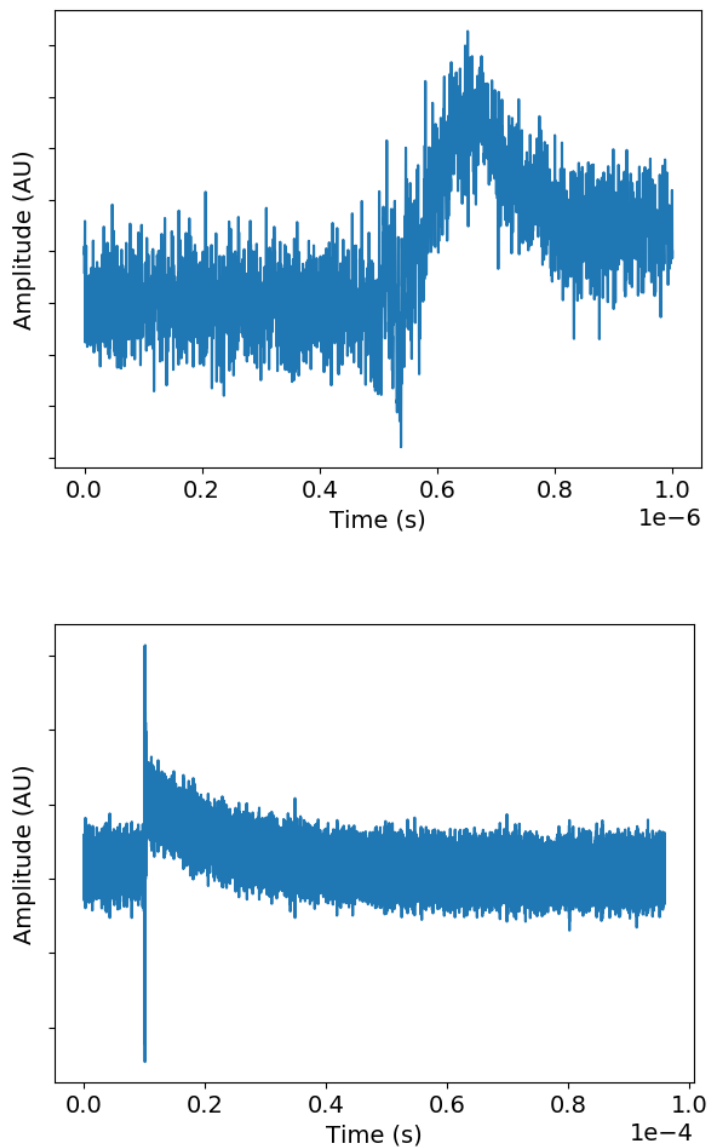
Figure 18. Raw TGS signals obtained in LiCl+1wt%NiCl₂. (Top) 100ns timebase obtained using a Hamamatsu C5658. (Bottom) 10μs timebase obtained using a Newport - New Focus 1801. Both signals are for approximate salt temperatures of 715°C and have different pump timing offsets applied.

LiCl signals were taken as an average of 10,000 grating formations and decays and were repeated 10 times at each measurement temperature. Small acoustic oscillations were observed in the short timescale signal for approximately 100 to 150 ns after pump beam exposure. To maximize the sensitivity of the fit to the oscillations, only a portion of the signal following pump beam exposure was fit. To determine the optimal fit duration, the standard error of Eq 11's C_4 fitting parameter was

plotted as a function of fit duration (Figure 19). A local minimum in the standard error was observed in the range of 110 to 150 ns, however, no clear optimal value was able to be determined using C_4 standard error alone. To support the selection of an optimal fit duration, the R^2 and mean squared error (MSE) of the entire fit was calculated over the 110 to 150 ns range (Figure 20). MSE and R^2 values indicated that approximately 120 ns yielded the best fits of the data and was thus used for all Eq 11 short timescale signals fits discussed in this section.
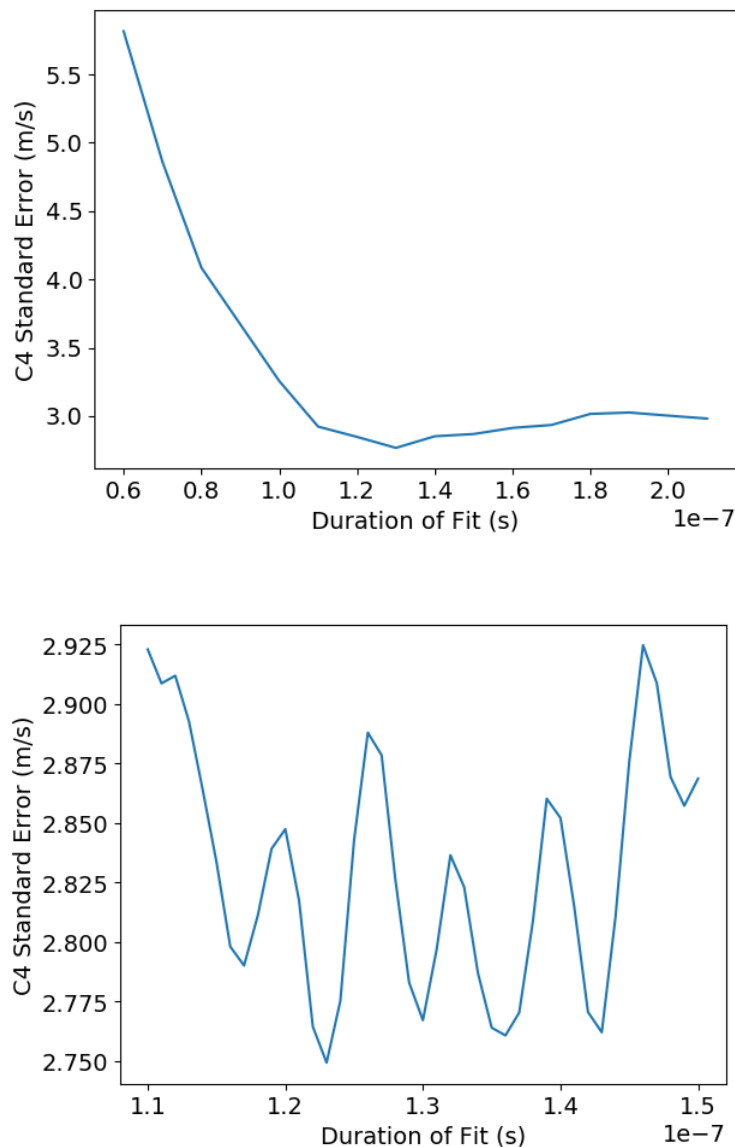
Figure 19. (Top) The average standard error of Eq 11's C_4 fitting parameter as a function of the duration of the fit for short timescale signals. (Bottom) An alternative version of the top plot with a reduced range in fit duration, showing no clear optimal value.
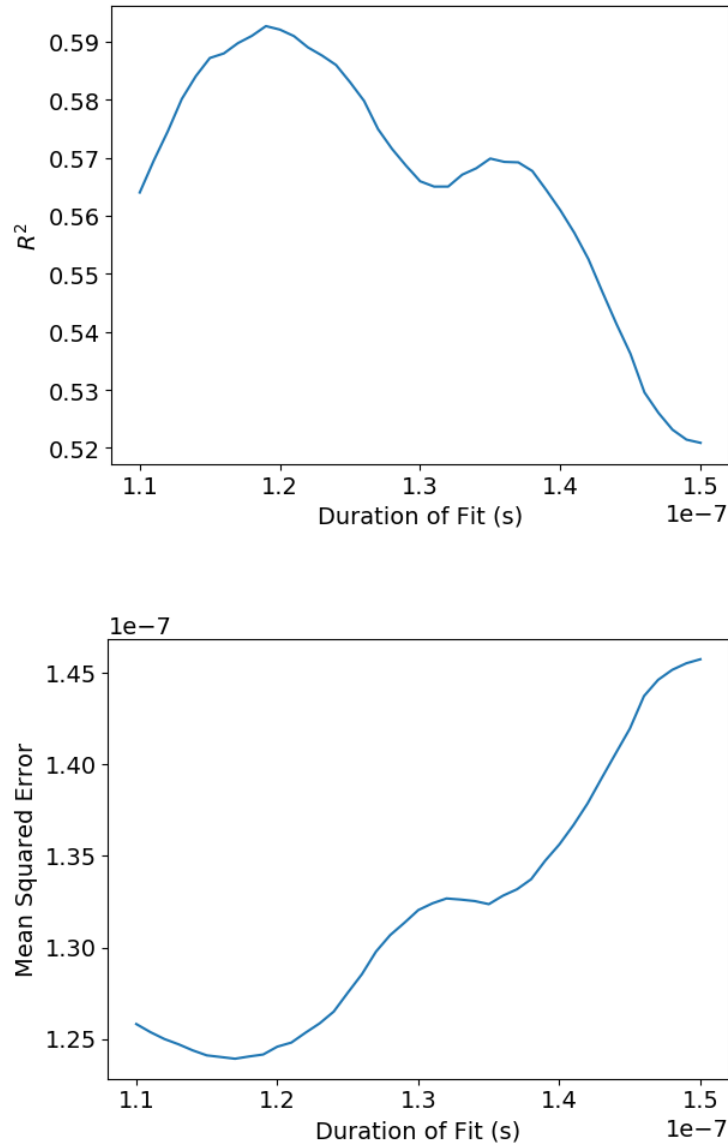
Figure 20. The average R^2 (Top) and mean squared error (Bottom) for the Eq 11 fit of short timescale signals as a function of the duration of the fit, showing an optimal value around 120 ns.

A comparison of the obtained sound speed results as a function of temperature to previous LiCl literature data [26] shows good agreement (Figure 21). A Chow Test [63] was used to assess whether there was a statistical difference between separate linear regressions of the TGS data and literature values, resulting in a F-Statistic of 9.7529 and a P-Value of 0.9998, or an inability to reject the null hypothesis. To perform the Chow test, the number of group degrees of freedom (DOF) was set at 2 due to the use of a liner model (i.e., slope and y-intercept), while the number of residual DOF was equal to 68 from the combined TGS and reference data points minus two times the group

DOF. To the authors' best knowledge, this is the first time that TGS has been used to measure halide molten salt sound speed, as previous groups focused solely on thermal diffusivity [24].
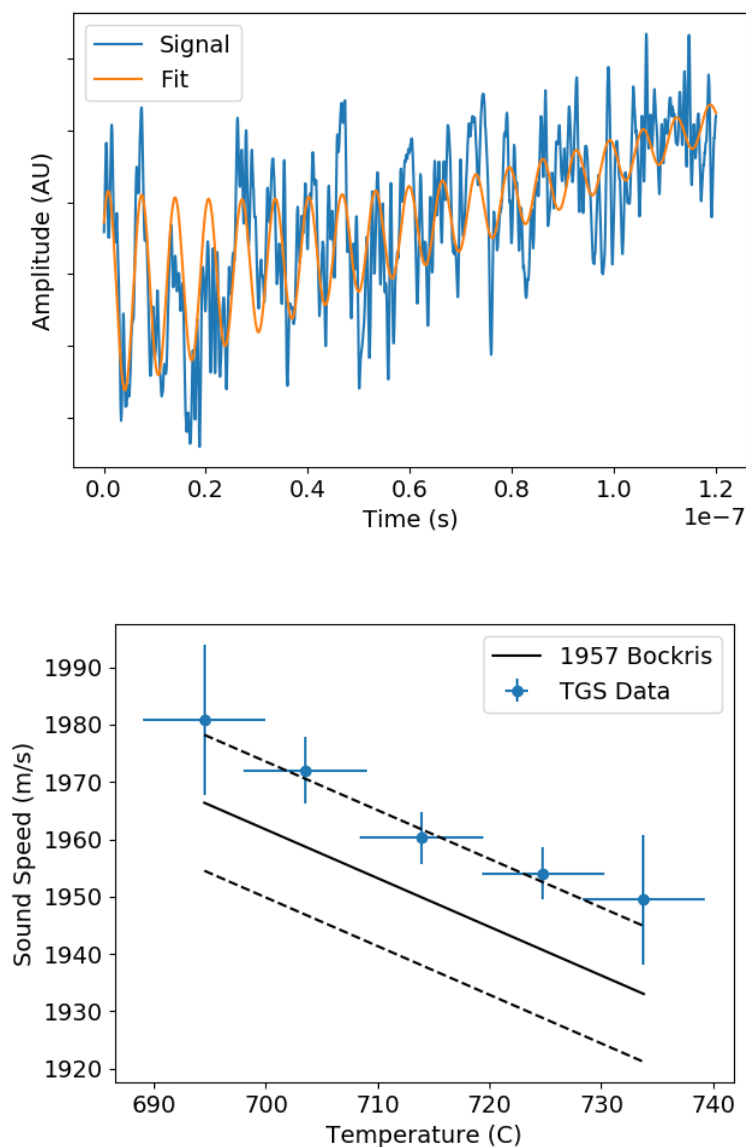
Figure 21. (Top) A portion of the short timescale signal measured in LiCl + 1 wt. % NiCl$_2$ at 713.9°C along with a fit of the data. (Bottom) Extracted sound speed results from the TGS measurements as compared to available literature values [26]. Signals were taken as an average of 10000 grating formation and decays and repeated 10 times at each temperature. All TGS data error bars represent plus or minus one standard deviation for the 10 independent measurements, with the dashed reference lines representing plus or minus one standard error of the estimate. Temperature uncertainty is reported as the adjusted thermocouple reading +/- 5.5°C as discussed in Section 2.2.

Despite the success of the sound speed measurements, restricting the fit duration is not ideal, and can be attributed to the apparent "slow" rise in the signal strength that is uncharacteristic of Eq 11 (Figure 18). Similar TGS signal shapes have been observed in other fluids and have been better modeled using a modified version of Eq 11 (Eq 13, where $0 < \beta < 1$) that is appropriate for viscoelastic samples [64]. Although a detailed analysis of this phenomenon is beyond the scope of the current thesis, Figure 22 exemplifies the improvement to the fit of the full short time scale signal when using Eq 13 vs Eq 11.
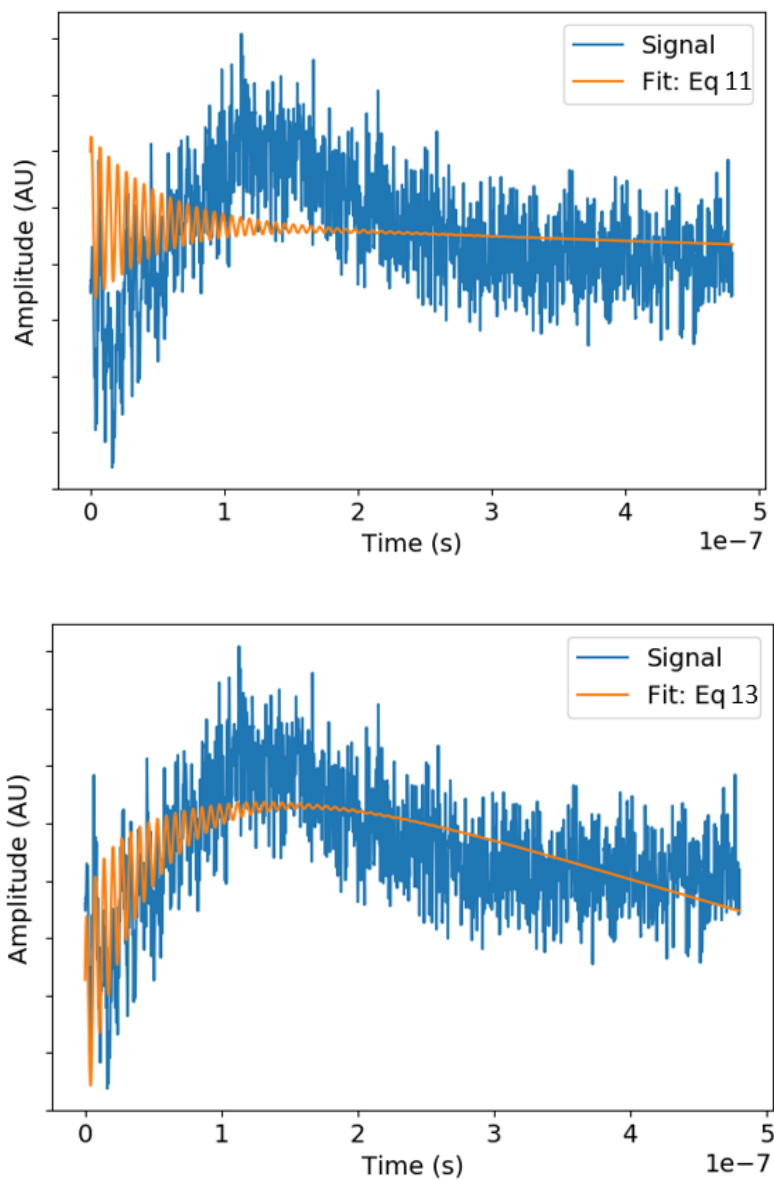
Figure 22. A comparison of Eq 11 (Top) and Eq 13 (Bottom) fits of the short timescale signal measured in LiCl + 1 wt. % $NiCl_2$ at 713.9°C.

$$I_D = \left[C_1 \left(e^{-C_2\left(\frac{2\pi}{d}\right)^2 t} - e^{-C_3 t} \cos\left(C_4 \left(\frac{2\pi}{d}\right) t \right) \right) + C_5 \left(e^{-C_2\left(\frac{2\pi}{d}\right)^2 t} - e^{-(C_6 t)^\beta} \right) \right]^2 \qquad \text{Eq 13}$$

Experiments conducted later with fluorides (Section 4.2) showed that by decreasing the level of reference probe light that was reaching the detector using a neutral density filter, the initial signal spike elicited the characteristic sharp rise. It is expected that saturation of the detector is likely responsible for the unusual signal shape observed in LiCl over very short timescales and is therefore not investigated further in this thesis.

Low signal to noise ratios for both the short and long timescale signals can be attributed to partial absorption of the 785 nm probe lasers by the 1 wt% $NiCl_2$, leaving room for optimization of the dye selection and concentration moving forward. However, without adequate absorption spectrum, the selection of a successful dye candidate is tedious. Consistency of melt vs solid phase colors has lent credence to the use of probe wavelength (785 nm, Red) colored dyes. As an alternative to dye trials, variable wavelength lasers could also be implemented to optimize the pump and probe wavelengths for each salt of interest.

Long timescale signals were fit effectively with Eq 11, as the initial 100 to 150 ns signal rise was unnoticeable over the 50 to 100 μs decay of the full signal (Figure 23). Signals were again taken as an average of 10,000 grating formation and decays and repeated 10 times at each temperature. Obtained thermal diffusivity results showed again good agreement with previous LiCl literature data (Figure 23), with a similar Chow test analysis resulting in an F-Statistic of 1.6690 and P value of 0.8038 (2 group degrees of freedom, 67 residual degrees of freedom). Although, a line of best fit for the TGS data would appear to have a positive slope, within the error of the two measurements, no distinction can be drawn between the two data sets. Additionally, as LiCl density has a strongly negative temperature dependance ($\rho_{LiCl} = 1884.2 - 0.4328 \cdot$T[K]) [24], converting the TGS obtained thermal diffusivity data to thermal conductivity yields a roughly constant value with temperature.
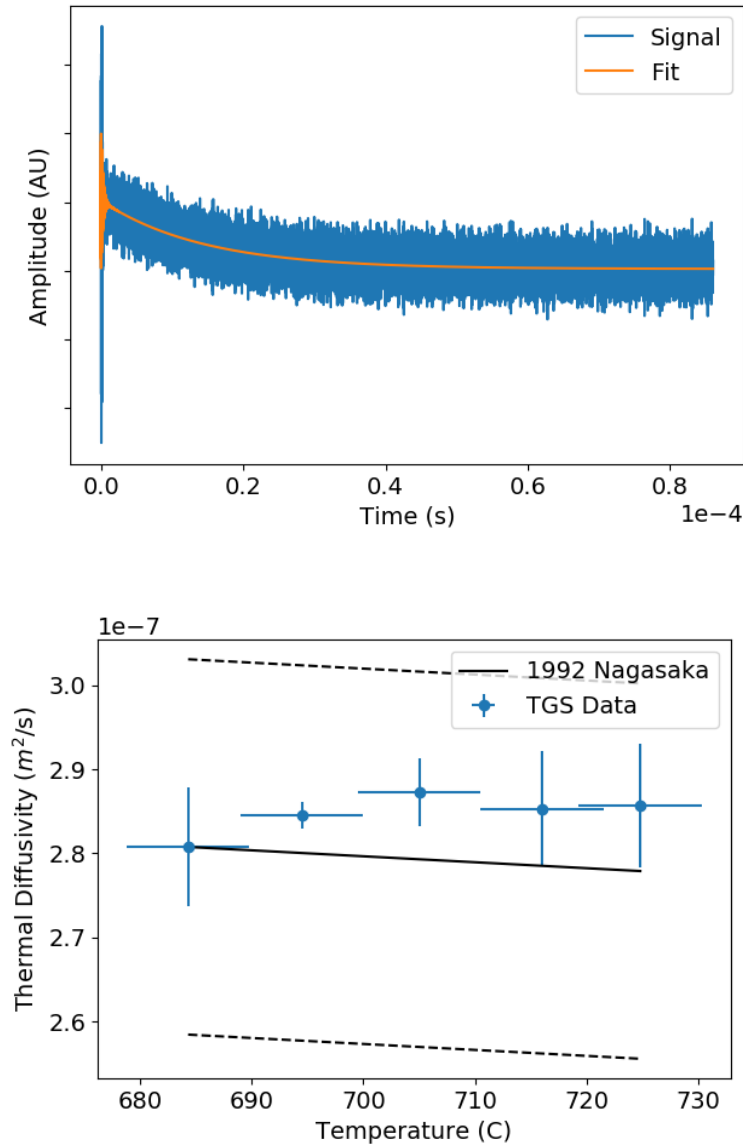
Figure 23. (Top) The long timescale signal measured in LiCl + 1 wt. % NiCl$_2$ at 716°C along with a fit of the data. (Bottom) Extracted Thermal diffusivity results from the TGS measurements as compared to available literature values [24]. Signals were taken as an average of 10000 grating formation and decays and repeated 10 times at each temperature. All TGS data error bars represent plus or minus one standard deviation for the 10 independent measurements, with the dashed reference lines representing plus or minus one standard error of the estimate. Temperature uncertainty is reported as the adjusted thermocouple reading +/- 5.5°C as discussed in Section 2.2.

2.4   System design outlook
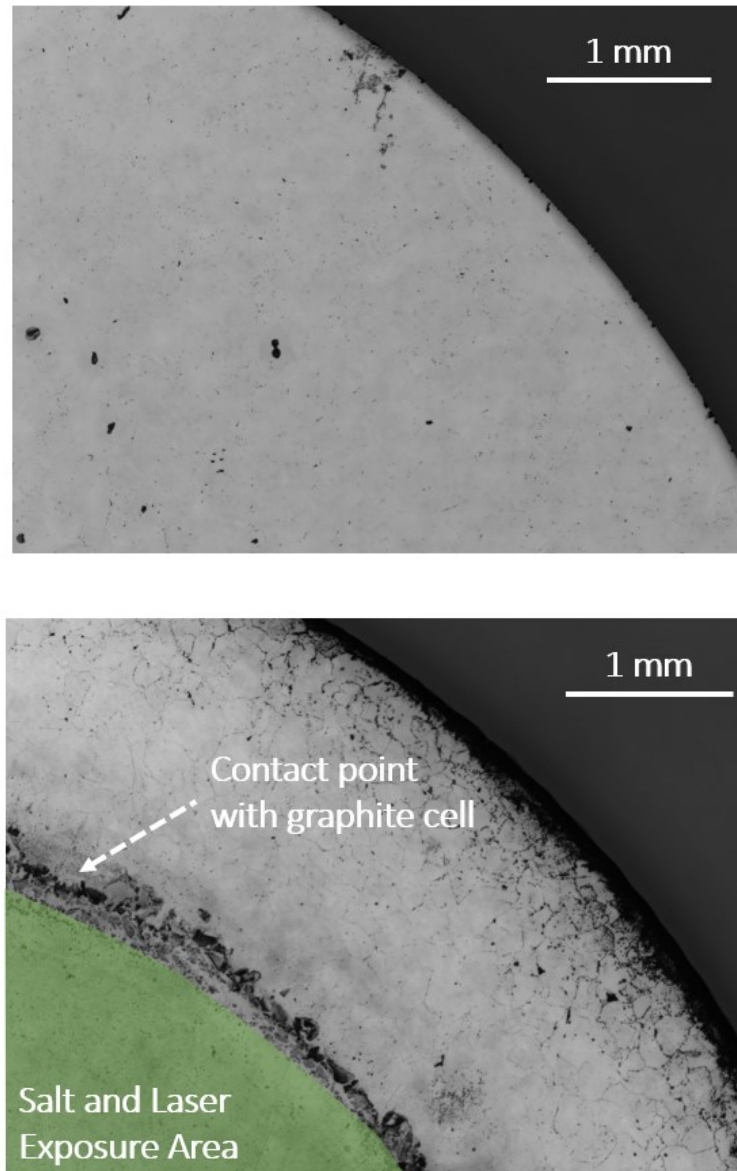
Figure 24. Optical microscope images of the CVD diamond windows used in the chamber design pre (Top) and post (Bottom) TGS measurements. The post salt exposure image was taken after multiple measurements (> 20 hours) of molten LiCl, with temperatures in excess of 700°C.

The success of the LiCl measurements coupled with the fact that no compatibility issues have been observed with fluoride salts, indicate that the chamber design should not be limiting when determining fluoride salt thermophysical properties using TGS. However, several issues with the design should be highlighted. Following several hours (20+) of salt exposure, the CVD diamond

windows began to lose transparency, hindering the signal strength of the measurements. The degradation of the windows performance is not expected to influence the results, as the timescale for signal reduction is many orders of magnitude longer than the full signal decay (100s μs vs hours). The introduction of corrosion products into the salt has the potential to modify bulk salt properties. However, as the addition of 1wt% of transition metal halides has not been shown to affect TGS results, the influence of corrosion products is expected to be below the sensitivity of this embodiment of the technique. Reducing the temperature and duration of the measurements can extend the windows lifetime, however, these windows can simply be treated as a consumable. Alternative window material such as MgO were also tried showing much higher signal strengths upon initial melting of the salt. Rapid deterioration of MgO prevented temperature dependent analysis from being performed, however, the higher transmission percentage of MgO may prove useful if alternative salts elicit compatibility.
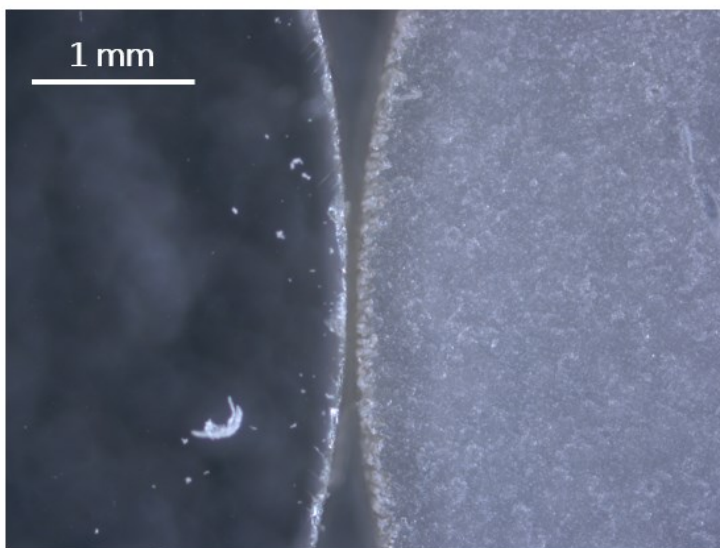
Figure 25. Optical microscope images of MgO windows prior to molten salt exposure (Left) and following exposure to FLiNaK for less than 30 minutes (Right). During FLiNaK exposure, salt temperatures did not exceed 500°C. MgO was not tested in LiCl.

In addition to the windows, the use of sheathed graphite cell presents another long-term challenge. Sealing of the windows is achieved by pressure from the external sheath on the graphite rings. Wear of the surfaces of these two components eventually leads to a reduction in the applied pressure resulting in salt leakage around the windows. Similarly, to the windows, the graphite rings can be treated as a consumable, with slight increases in thickness being applied to the replacements. A fully

metallic cell (Ex. Ni201) presents an interesting opportunity moving forward, however, challenges with thermal expansion would need to be accounted for in the design.

Ultimately, the development of this optically transparent molten salt thermophysical property measurement system appear to have successfully isolated the specific properties of interest, particularly thermal diffusivity, from other heat transfer modes. The relatively short timescale of the measurement (100s μs) precludes the formation and propagation of convective eddy currents, and the very low temperature rise due to the transient grating excitation has previously been hypothesized to mitigate radiative heat transfer contributions [59]. However, as radiation likely plays a significant role in many of the previous experimental techniques error, a rigorous validation of its negligible role within TGS measurements is the subject of the following section.

3. The role of radiation in transient grating spectroscopy

Parts of this chapter have been reproduced from A. A. Maznev, S. G. Robertson, M. P. Short and K. A. Nelson, "Radiative contribution to thermal grating decay," Journal of Applied Physics, 130, 2021, with the permission of AIP Publishing

3.1 Formulation of the radiative contributions to TGS grating decay

At the high temperatures that molten salts operate, avoiding contributions from radiation in thermal conductivity measurements can be difficult. To understand the extent to which a given setup is at risk (and potentially adjust the measured values as a result), means of accurately quantifying the potential radiative contributions are required. One relatively simple formulation that was developed using a kinetic heat transport approach (Eq 14) [65] (similar to what is adopted for describing thermal diffusivity in gases), is shown In Eq 14. Optical properties were assumed to be independent of wavelength, where λ_r is the radiative contribution to thermal conduction, n is the material's refractive index, σ is the Stefan-Boltzmann constant, T_0 is the background temperature and ϵ is the optical extinction coefficient (sum of the absorption and scattering coefficients).

$$\lambda_r = \frac{16n^2\sigma T_0^3}{3\epsilon} \qquad \text{Eq 14}$$

For transparent or low extinction coefficient materials such as molten salts, Eq 14 can be seen to diverge. This highlights a general limitation of models of this type, as they can be seen to only strictly apply when the heat transfer distance is much larger than the extinction length of the thermal radiation ($1/\epsilon$). For short heat transfer distances or transparent medium, relevant formulations must start from the more general Radiation Transport Equation (RTE) [66].

With the assumption of a non-scattering medium, changes in thermal radiation energy density (e) with time (t) and along the wavevector (k) are governed primarily by the absorption and emission of light. The loss due to absorption can be expressed as the energy density multiplied by the distance traveled (dk) over the absorption length (a, inverse of the absorption coefficient). At equilibrium, the radiation energy density is a result of blackbody radiation, and therefore the gain due to emission can be expressed as a function of the blackbody energy density at the perturbed temperature T ($e_0(T)$) [66]. Combining these terms yields the RTE for an isotropic non-scattering absorbing medium (Eq 15).

$$e(k + dk, t + dt) - e(k, t) = \frac{e_0(T) - e(k, t)}{a} dk \qquad \text{Eq 15}$$

Eq 15 can be simplified by expressing the outgoing energy density as a Taylor series $(e(k + dk, t + dt) = e(k, t) + dt(\partial e/\partial t) + dk(\partial e/\partial k))$. Substituting the group velocity (v_g) for dk/dt and converting the direction of interest to x through addition of a factor $cos(\theta)$, where θ is the angle between the wavevector and the x direction yields Eq 16.

$$\frac{1}{v_g}\frac{\partial e}{\partial t} + cos\theta \frac{\partial e}{\partial x} = \frac{e_0(T) - e}{a} \qquad \text{Eq 16}$$

To describe a system where both radiation and thermal conduction take place, the net gain or loss due to emission and absorption of radiation can be added to the classical heat diffusion equation (Eq 17), where C is the volumetric heat capacity, λ is the material's intrinsic thermal conductivity and Q accounts for any potential heat source.

$$C\frac{\partial T}{\partial t} - \lambda\frac{\partial^2 T}{\partial x^2} = -\int \frac{v_g}{a}[e_0(T) - e]dk + Q \qquad \text{Eq 17}$$

These two expressions (Eq 16 and Eq 17) act as the starting point for a derivation of the potential contributions of radiation to TGS grating decay. As a first step, a Fourier transform $(\tilde{f}(\eta, \xi) = \int f(t) e^{i\eta t - i\xi x} dt)$ can be applied to both Eq 16 and Eq 17. A simplification can be made that as the rate of thermal conduction is much slower than the speed of light, time derivatives in Eq 16 can be neglected, yielding Eq 18 and Eq 19.

$$-i\xi v_g cos(\theta)\, \tilde{e} = \frac{v_g(\tilde{e}_0(T) - \tilde{e})}{a} \qquad \text{Eq 18}$$

$$i\eta C\tilde{T} + \xi^2 \lambda \tilde{T} = -\int \frac{v_g}{a}[\tilde{e}_0(T) - \tilde{e}]dk + \tilde{Q} \qquad \text{Eq 19}$$

At this stage, an expression for the blackbody thermal radiation energy density (Eq 20, akin to Planck's law) can be introduced. In Eq 20, ω is the angular frequency, $\hbar$ is the reduced plank constant $(h/2\pi)$ and k_B is the Boltzmann constant. For convenience, a term that separates the frequency

dependance ($\beta(\omega)$) from the perturbation temperature can be used, with a factor v_g/a being included to simplify the remaining derivation.

$$e_0(T) = \frac{2\hbar^2\omega^2 e^{\frac{\hbar\omega}{k_B T_0}}}{(2\pi)^3 k_B T_0^2 \left(e^{\frac{\hbar\omega}{k_B T_0}} - 1\right)^2} T = \frac{\beta(\omega)aT}{v_g}$$

Eq 20

Solving for $\tilde{e}$ in Eq 18 and subbing it into Eq 19, allows for an expression for the Fourier transformed perturbation temperature (Eq 21) to be determined.

$$\tilde{T} = \frac{\tilde{Q}}{i\eta C + \xi^2\lambda - \int \left(1 - \frac{1}{1 - i\xi a\cos(\theta)}\right)\beta(\omega)dk}$$

Eq 21

The integral with respect to the wavevector (k) in Eq 21 can be converted to an integral with respect to angular frequency and solid angle. The integration over angle can then be evaluated analytically resulting in Eq 22.

$$\tilde{T} = \frac{\tilde{Q}}{i\eta C + \xi^2\lambda - \frac{4\pi}{c^3}\int n^3\omega^2\left(1 - \frac{arctan(\xi a)}{\xi a}\right)\beta(\omega)d\omega}$$

Eq 22

For TGS, the interference pattern of the two pulsed "pump" beams allows the heat source to be approximated as a delta function in time (i.e. instantaneous) and sinusoidal in space (Eq 23), where Q_0 is the initial amplitude, and q is the grating's wavevector.

$$Q(t,r) = Q_0\delta(t)e^{iqx}$$

Eq 23

Applying a Fourier transform to Eq 23 and substituting it into Eq 22 results in Eq 24.

$$\tilde{T} = \frac{2\pi Q_0\delta(\xi - q)}{i\eta C + \xi^2\lambda - \frac{4\pi}{c^3}\int n^3\omega^2\left(1 - \frac{arctan(\xi a)}{\xi a}\right)\beta(\omega)d\omega}$$

Eq 24

Performing an inverse Fourier transform on Eq 24 provides the temperature profile in the material ($T = (Q_0/C)e^{-\gamma t}e^{iqx}$) where γ is the TGS grating decay rate, defined by Eq 25.

$$\gamma = \frac{1}{C}\left[q^2\lambda + \frac{4\pi}{c^3}\int n^3\omega^2\left(1 - \frac{arctan(qa)}{qa}\right)\beta(\omega)d\omega\right]$$

<div align="right">Eq 25</div>

Eq 25 can be seen to yield an "effective" thermal conductivity ($\lambda_{eff} = \gamma C/q^2$) responsible for the decay of the TGS grating, where the material's intrinsic thermal conductivity (λ) is aided by an additional contribution from radiation (λ_r). Extracting the radiative contribution and substituting back in the definition of $\beta(\omega)$ (Eq 20) yields Eq 26. This provides a rigorous definition of the potential role of radiation in TGS measurements, the evaluation of which is the subject of sections 3.2 to 3.4.

$$\lambda_r = \frac{\hbar^2}{\pi^2 c^3 q k_B T_0^2}\int_0^\infty d\omega \frac{n^3 v_g \omega^4 e^{\frac{\hbar\omega}{k_B T_0}}}{\left(e^{\frac{\hbar\omega}{k_B T_0}} - 1\right)^2}\frac{1}{qa}\left[1 - \frac{arctan(qa)}{qa}\right]$$

<div align="right">Eq 26</div>

3.2 Maximum possible radiative contribution for TGS
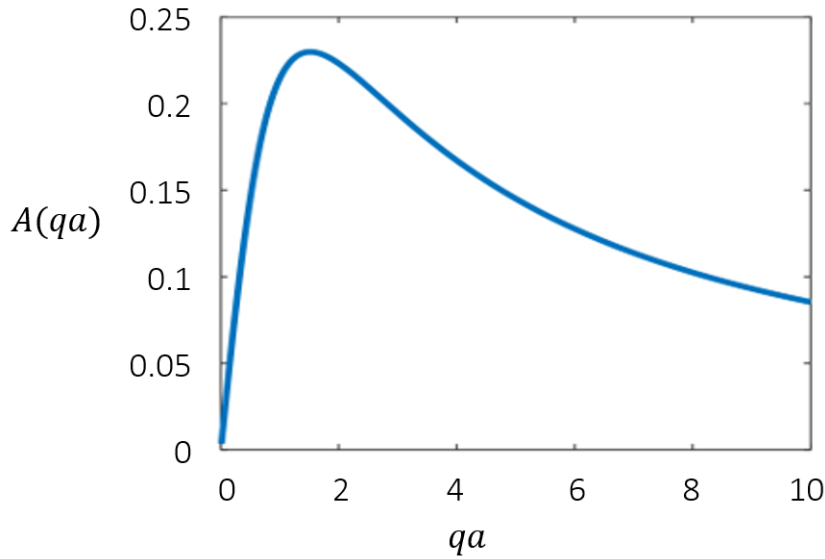
Figure 26. The collective dependence (Eq 27) of the radiative contribution to absorption length (a) plotted as a function of the product of the grating's wavevector (q) and absorption length.

To establish an upper bound for Eq 26, simplifications can be made by replacing different property dependencies with maximum possible values. For the material's wavelength dependent absorption length, its influence can be consolidated into Eq 27. Plotting this expression as function of the product of the grating's wavevector (q) and absorption length (a), shows a maximum for qa values

of roughly 1.5 (Figure 26). Physically, this implies that radiative contributions are highest when the absorption length and grating spacing are of comparable magnitudes, as the grating wavevector is inversely proportional to the grating spacing ($d = 2\pi/q$).

$$A(qa) = \frac{1}{qa}\left[1 - \frac{arctan(qa)}{qa}\right]$$

Eq 27

Replacing Eq 27 by its maximum value (A_{max}, approximately 0.23) reduces the complexity of the integral in Eq 26. Setting the refractive index at an artificially large constant value (ex 4) allows for further simplification, recalling that the group velocity takes the form c/n when n is independent of wavelength.

$$\lambda_r = \frac{A_{max}n^2\hbar^2}{\pi^2c^2qk_BT_0^2}\int_0^\infty d\omega \frac{\omega^4 e^{\frac{\hbar\omega}{k_BT_0}}}{\left(e^{\frac{\hbar\omega}{k_BT_0}} - 1\right)^2}$$

Eq 28

Pulling a factor of $(\hbar/k_bT_0)^4$ back into the integral allows for substitution of $x = \hbar\omega/k_bT_0$ and $dx = (\hbar\omega/k_BT_0)d\omega$, resulting in well-defined definite integral (Eq 29).

$$\lambda_r = \frac{A_{max}n^2k_B^4T_0^3}{\pi^2c^2q\hbar^3}\int_0^\infty dx \frac{x^4e^x}{(e^x - 1)^2}$$

Eq 29

Replacing the integral with its value of $4\pi^4/15$ results in a final analytical expression (Eq 30) for the maximum possible contribution of radiation to transient grating decay, with the Stefan-Boltzmann constant ($\sigma = 2\pi^5k_B^4/15c^2\hbar^3$) being used to further simplify the expression.

$$\lambda_r = \frac{2A_{max}\sigma n^2T_0^3}{q\pi^3}$$

Eq 30

3.3   Estimating FLiNaK optical properties

To assess the role of radiation in TGS measurements beyond the maximum possible contribution, wavelength dependent absorption coefficient and refractive index data are required. Experimental setups used to obtain these properties have suffered from similar material compatibility challenges to TGS (Section 2), limiting the availability of relevant data for fluorides. In the absence of experimental data for FLiNaK, estimates have been determined (Figure 27) by combining the results of ab-initio simulations [47] and single constituent data [67] [68] [69] [70].
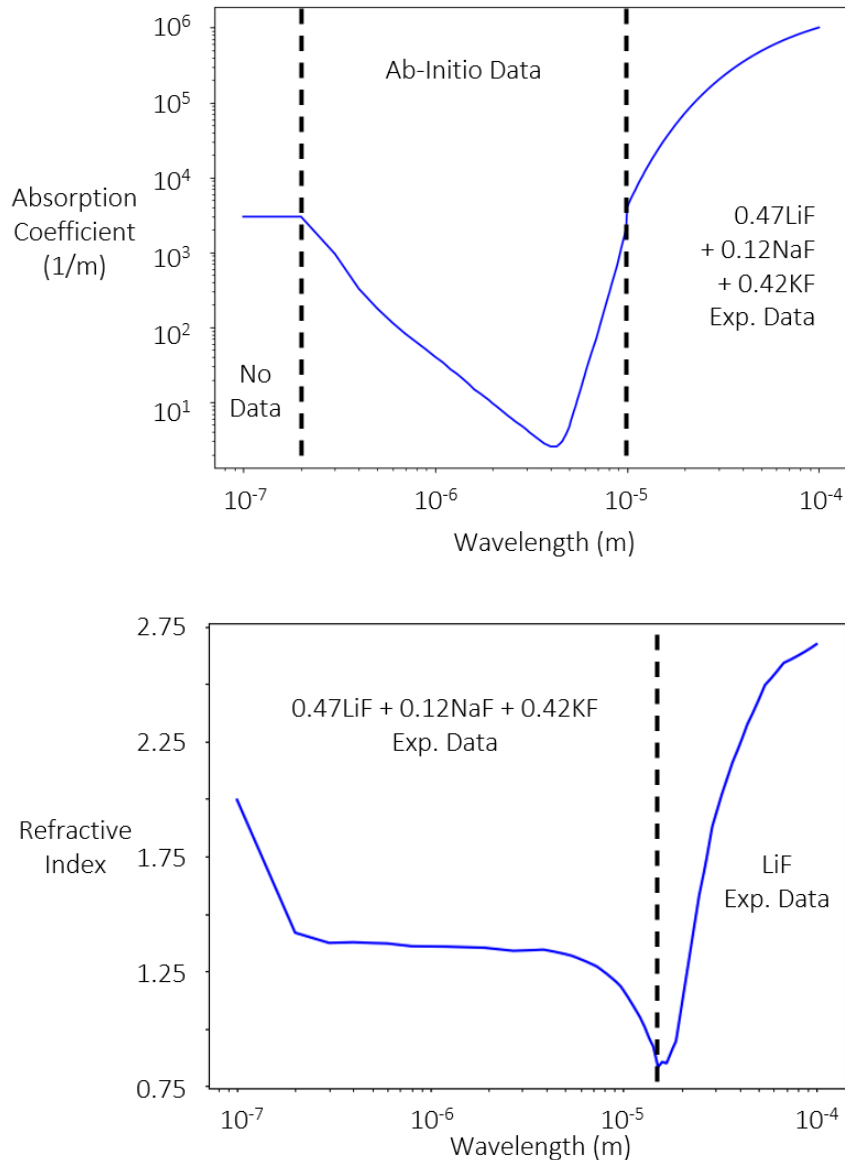
Figure 27. Compiled estimates of FLiNaK's wavelength dependent absorption coefficient (Top) and refractive index (Bottom) data. Original data used in the creation of these plots is a combination of simulated [47] and single constituent results [69] [68] [67] [70].

For FLiNaK's absorption coefficient, ab-initio results [47] were used at wavelengths below 10μm, while experimental data for LiF, NaF, and KF [67] were combined proportional to the FLiNaK eutectic composition (i.e. 0.465 LiF + 0.115 NaF + 0.42KF) for wavelengths great than 10μm. Several sets of experimental data were considered unreliable, as many showed negative absorption coefficients or values of exactly zero at certain wavelengths [71]. Estimates of FLiNaK's refractive index were taken as a similar additive contribution from the single constituent data [68] below

12.5μm, while above 12.5μm, the lack of data necessitated the use of experimental results strictly for LiF [69] [70]. This approximation can be justified as LiF has a large mol fraction in FLiNaK (0.465), as well as wavelength ranges (< 12.5μm) where data for all three constituents are available showed very similar values (1.35 to 1.4).

In practice, literature data was digitized with a linear extrapolation being applied in between data points to provide a continuous function for numerical integration. As the integral in Eq 26 is infinite, evaluation of optical properties below 100nm or above 100μm were taken as constants (Table 2). Temperature dependance of the optical properties has not been considered, both due to the lack of data, and the small expected contribution that it would likely play [68].

Table 2. Estimates of FLiNaK's absorption coefficient and refractive index at the wavelength bounds (100nm and 100μm) of Figure 27.

Wavelength	Absorption Coefficient (1/m)	Refractive Index
100nm	$2.9973 \cdot 10^3$	1.9957
100μm	$1.0064 \cdot 10^5$	2.6725

Rough agreement between the single constituent estimates and abi-initio values at the boundaries of the data sets for the absorption coefficient provides additional confidence in the approximation. However, this should not act as a true substitute for real experimental data for FLiNaK without proper validation. The use of the current TGS chamber or other diamond-based setups should be explored for the acquisition of salt optical properties and is the subject of one of the future research directions outlined in Section 6.2.

3.4   Quantifying radiative contributions to FLiNaK TGS measurements

Using the estimates of FLiNaK's wavelength dependant optical properties outlined in Section 3.3, Eq 26 can be evaluated numerically. Numerical integration was performed using SciPy's integrate.quad function with $1.88 \cdot 10^{13}$ Rad/s (100μm) and $1.88 \cdot 10^{16}$ Rad/s (100nm) acting as lower and upper integration bounds respectively. Convergence of the obtained results within these integration bounds was observed (Figure 28), with minimal sensitivity being shown to the upper integration limit (lower wavelengths) at these temperatures (500ºC).
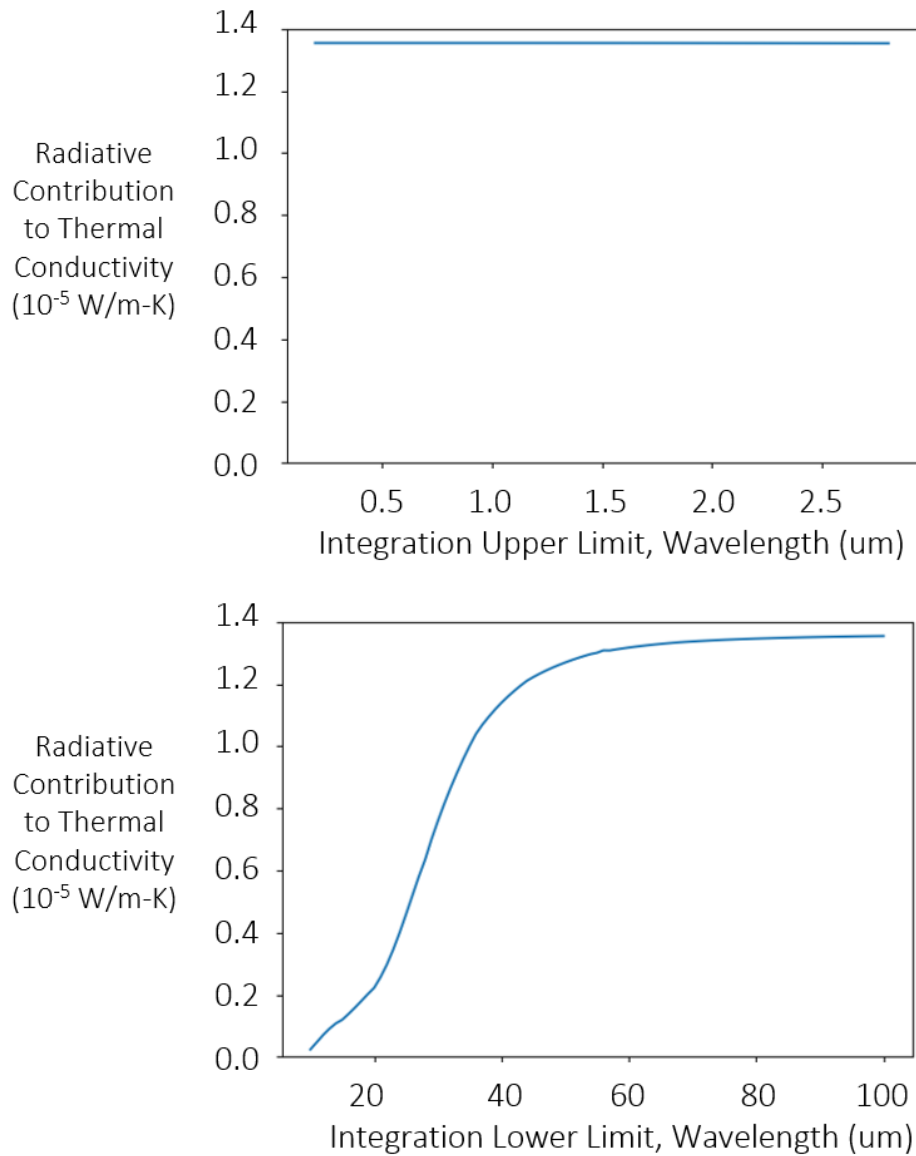
Figure 28. Sensitivity of the calculated radiative contribution to the upper (Top) and lower (Bottom) integration limits of Eq 26. Results shown are for the FLiNaK optical properties estimated in Section 3.3 for a grating spacing of 17.6μm and a temperature of 500°C. Grating spacing and temperature have been selected based on the applicability to the FLiNaK experiments conducted in Section 4.

In addition to evaluating Eq 26 numerically, the conservative maximum possible contribution (Eq 30) is also presented in Figure 29 for comparison. Results are shown as a function of TGS grating spacing and salt temperature, with the corresponding fixed parameter (500°C and 17.6μm) being selected based on its applicability to the FLiNaK results presented in Section 4.
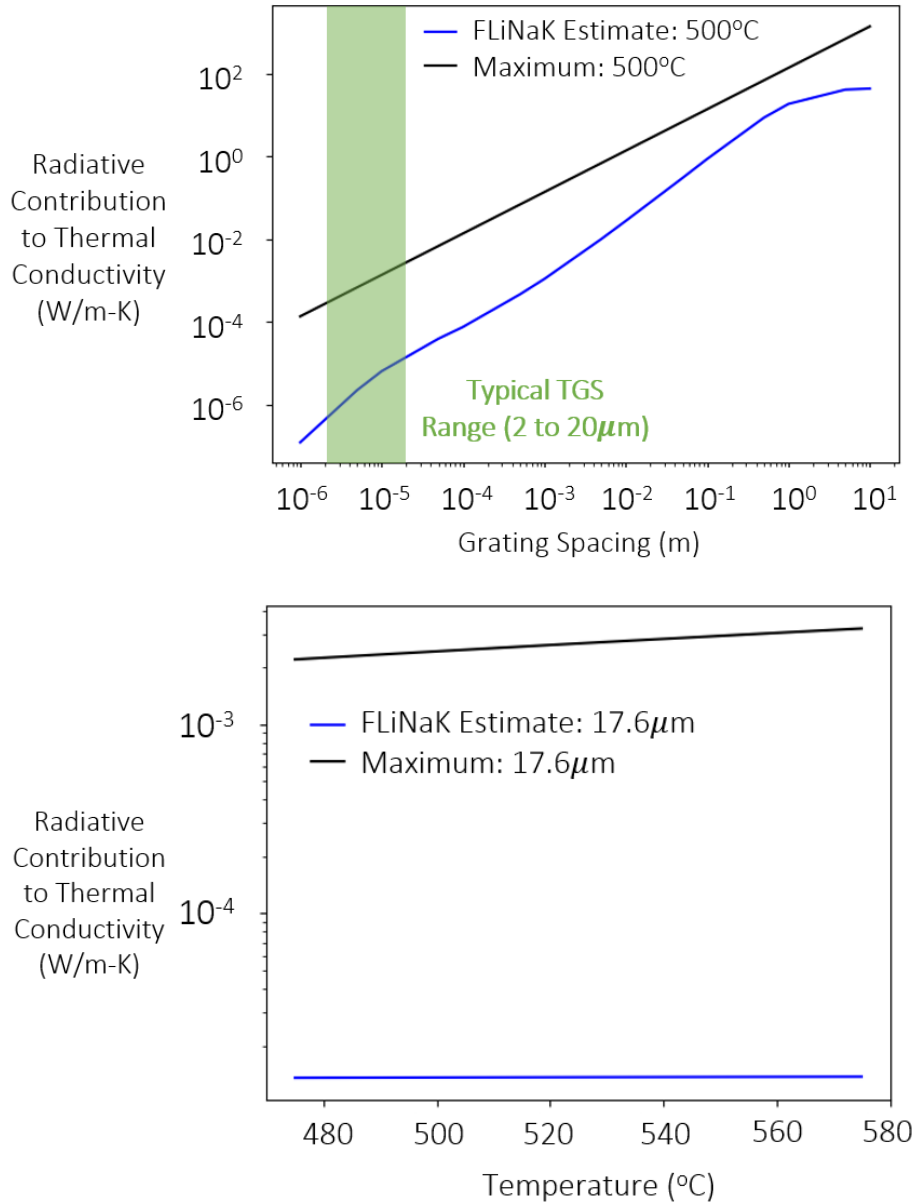
Figure 29. Maximum possible and FLiNaK estimates of radiative contributions to thermal conductivity as a function of TGS grating spacing (Top) and temperature (Bottom). Typical grating spacings used in the TGS setup discussed in this thesis are highlighted in green.

Although existing Fluoride salt thermal conductivity data is suspect, more reliable experimental measurements and theoretical models have converged on an expected order of magnitude of 1 W/m-K for the thermal conductivity of FLiNaK. Based on the results shown in Figure 29, even at the maximum possible contribution, the influence of radiation is likely insignificant for grating spacings below 100μm. However, when using a more realistic estimate based on the optical

properties of FLiNaK, this grating spacing cutoff grows to several millimeters. As TGS measurements are typically performed on the single to tens of μm range, this result provides confidence that TGS measurements are likely not plagued by the confounding contributions from radiation that other techniques (Section 1.5) have suffered from. This result sets the stage for potentially the first thermal conductivity measurements in FLiNaK and fluoride salts more broadly that have truly isolated a single mode of heat transfer, namely conduction.

4. Evaluating FLiNaK thermophysical properties with TGS

Parts of this chapter have been reproduced from S. G. Robertson, R. Wiser, W. Yang, S. Choi, E. Bagletto and M. P. Short, "The Curious Tempertaure Dependence of Fluoride Molten Salt Thermal Conductivtiy" Journal of Applied Physics, 2022, with the permission of AIP Publishing

4.1 FLiNaK sample preparation and composition

Following validation of the molten salt compatible setup (Section 2) and confirmation of the negligible role of radiation in TGS (Section 3), FLiNaK (the eutectic composition of LiF-NaF-KF [46.5-11.5-42 mol%]) was selected as a model fluoride system for investigation. FLiNaK is a commonly proposed coolant salt and has already been subject to numerous experimental and theoretical attempts at determining thermal conductivity (Figure 3) [11] [8], making it an ideal candidate to test the erroneous temperature dependance hypothesis (Section 1.7).

Within an argon glove box, approximately 7 g of FLiNaK (supplied by Copenhagen Atomics, 99.9% metals basis) were loaded into the custom graphite cell detailed in Section 2.1. The salt containing cell was then transferred into the TGS measurement vacuum chamber (Section 2.1), being exposed to air for less than one minute. The chamber was pumped down to below 100mtorr and heated to approximately 340°C for roughly 15 hours to remove moisture introduced during salt handling. As mentioned in Section 2.2, this length of bakeout is likely unnecessary to remove moisture, as minimum vacuum levels are reached after several hours.

Following preheating, the samples were taken up to 480°C (roughly 25°C above the salt's melting point) and allowed to equilibrate for 30 minutes. Measurements were taken from approximately 480 to 580°C, with the salt heating (cooling) rate varying between 1.0 to 2.5°C/min (-2.8 to -4.0°C/min). Data was obtained while the sample was both increasing and decreasing in temperature, with the salt being cycled up to 580°C twice, once for the acquisition of short timescale (100ns timebase), and once for the acquisition of long timescale signals (20μs timebase). As a result of this procedure, each salt sample was held above its melting point for roughly 4 hours.

To absorb adequate levels of pump light (532nm) for grating formation, a small amount ($\approx$ 1wt%) of CoF_2 was added to the FLiNaK samples. Based on the success of the LiCl results (Section 2.3), several attempts were also made with NiF_2. NiF_2 based samples resulted in minimal pump wavelength (532nm) absorption and were not investigated further. Although absorption spectrum data for fluorides is sparse, early experiments analyzing CoF_2 in FLiNaK indicate that single wt%

additions could be responsible for up to a two-fold increase in 532 nm absorption [72]. Previous work on single constituent salts showed that additions of transition metal halides at these levels are not expected to influence the salt's bulk thermophysical properties [59]. However, to further validate this hypothesis and assess day-to-day variations in the system performance, five different FLiNaK samples were prepared with CoF_2 additions ranging from 0.7 to 1.5 wt%.
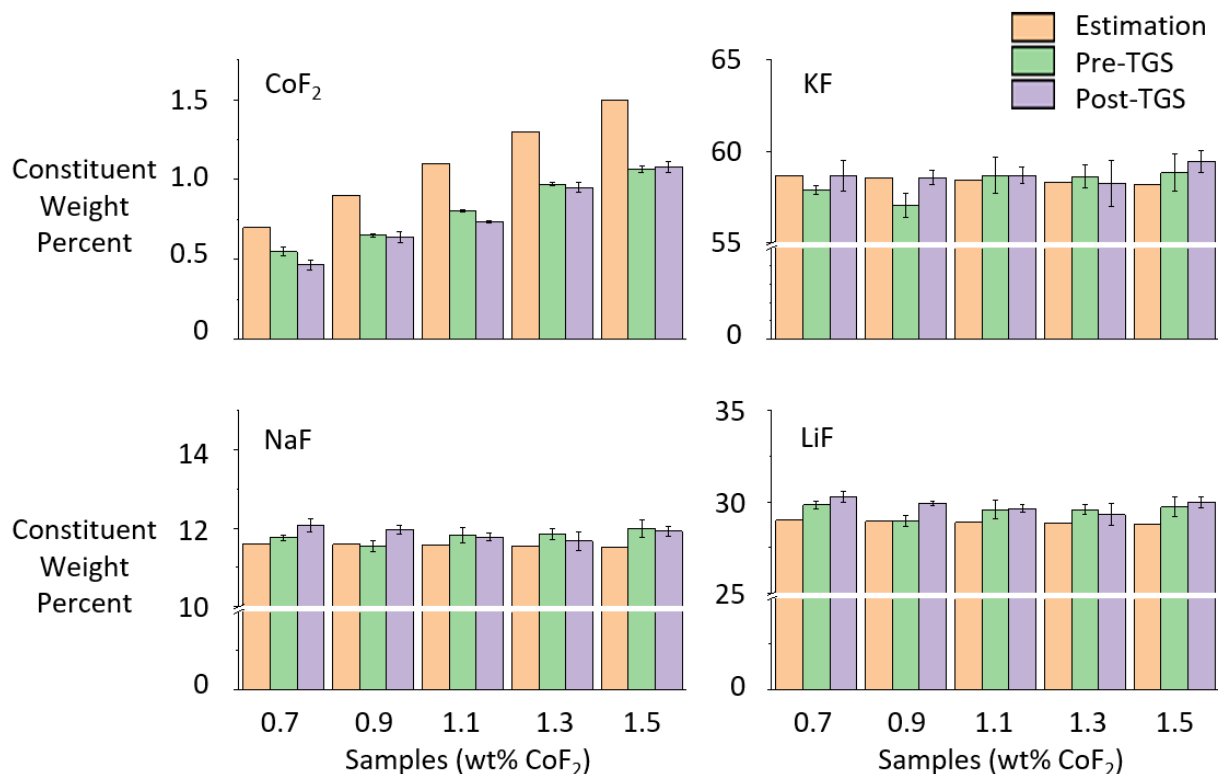
Figure 30. ICP-AES composition results for the bulk constituents present in the pre and post TGS measurement samples. The expected weight precents if an exact eutectic of LiF-NaF-KF with the desired CoF_2 additions was used is also included. Elemental results have been converted to constituent weight percent by assuming the oxidation state or number of fluorine anions that would be associated with the cation.

As a further assessment of the accuracy of the results, salt composition analysis for both pre and post TGS measurements was performed using Inductively Coupled Plasma - Atomic Emission Spectroscopy (ICP-AES) and Mass Spectrometry (ICP-MS) by colleagues at Seoul National University (SNU) and Korea Advanced Institute of Science and Technology (KIST), in the group of Professor Sungyeol Choi. 4 random pieces of the solidified salt were taken from the pre and post measurement samples, with all handling operations being conducted in a glovebox with an argon environment

([O2], [H2O] < 5 ppm). A mixed acid with 1 to 1 ratio of HNO_3 (68±2%, JKC) and HF (49~50%, JKC) was used for the ICP-solution. Measurements were conducted at the National Center for Inter-university Research Facilities (NCIRF) and were performed 3 times for each of the 4 pieces of a sample. ICP-AES results for the bulk-constituents and ICP-MS results for the observed impurities are presented in Figure 30 and Figure 31 respectively. R-squared values for the calibration curves and detection limits for both the ICP-AES and ICP-MS are presented in Table 3.

Table 3. Detection limits and calibrations curve R^2 values for the elements and instruments used to analyze salt composition.

Instrument	Element	Calibration Curve R^2	Detection Limit
ICP-AES OPTIMA 8300 Perkin-Elmer	K	0.999998	< 0.01 ppm
	Na	0.999999	< 0.05 ppm
	Li	0.999999	< 0.01 ppm
	Ca	0.999981	< 0.01 ppm
	Co	0.999950	< 0.01 ppm
	Ni	0.999936	< 0.01 ppm
	Cr	0.999938	< 0.01 ppm
ICP-MS MexIon 350D Perkin-Elmer	Fe	0.999768	< 0.1 ppb
	Rb	0.999997	< 0.1 ppb
	Sr	0.999998	< 0.1 ppb
	Ba	0.999936	< 0.1 ppb
	Cs	0.999995	< 0.1 ppb

Figure 30 highlights that the resulting CoF_2 concentrations ended up being lower than what was expected based on the sample preparation. High moisture content or vapor pressure of the CoF_2 constituents, is likely responsible for the deviation.
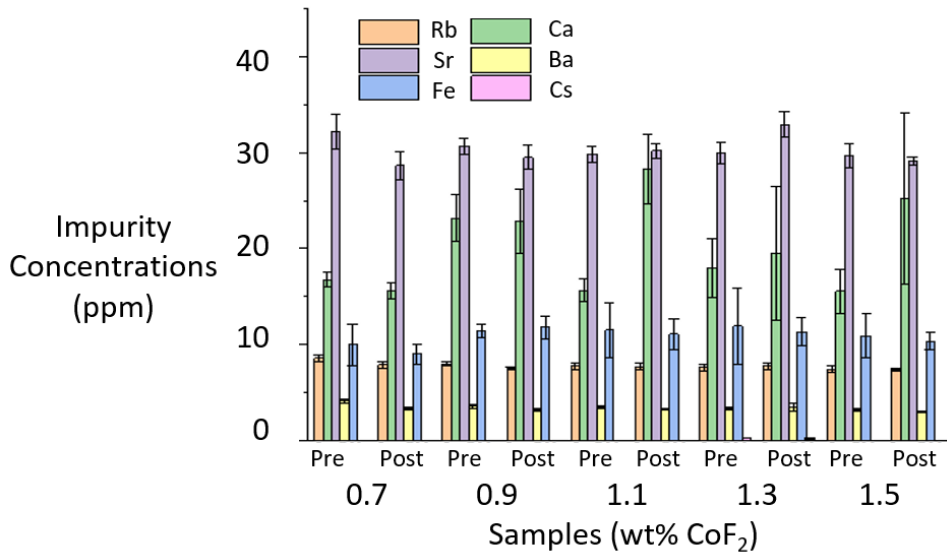
Figure 31. ICP-MS composition results for the impurities present in the pre and post TGS measurement samples.

4.2 TGS obtained FLiNaK thermal conductivity results
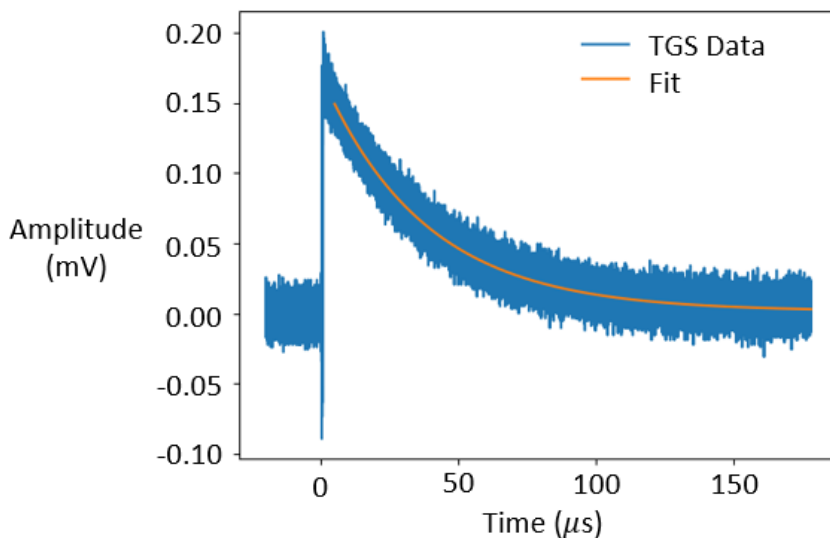
Figure 32. Raw long timescale TGS signal (blue) for FLiNaK at 489°C along with the fit of the signal (orange) used to extract the salt's thermal diffusivity. The signal shown represents the average of 10,000 grating formation and decays. Fit start time is chosen as 5 μs to avoid short timescale noise, however, the obtained results prove insensitive to fit start time. Y-axis has been normalized to a zero-value baseline as this is a DC coupled detector.

Over longer timescales (0 to 180 μs), FLiNaK TGS signals displayed the characteristic exponential decay. Figure 32 shows a typical TGS signal that was observed in FLiNaK, highlighting the significant increase in signal to noise compared to the previous LiCl validation results (Figure 18)

Figure 33 (Left) shows the obtained thermal diffusivity data for the five samples (FLiNaK plus varying concentrations of CoF$_2$) as a function of temperature. The data from TGS was then converted to thermal conductivity (Figure 33 (Right)) using the recommended correlations for FLiNaK density ($\rho = 2579 - 0.624 \cdot T[K]$ in kg/m^3) and heat capacity ($c_P = 1884$ in J/kg-K) [10]. Although recommended, the potential influence of uncertainty in existing heat capacity data will be addressed further in Section 5.2.
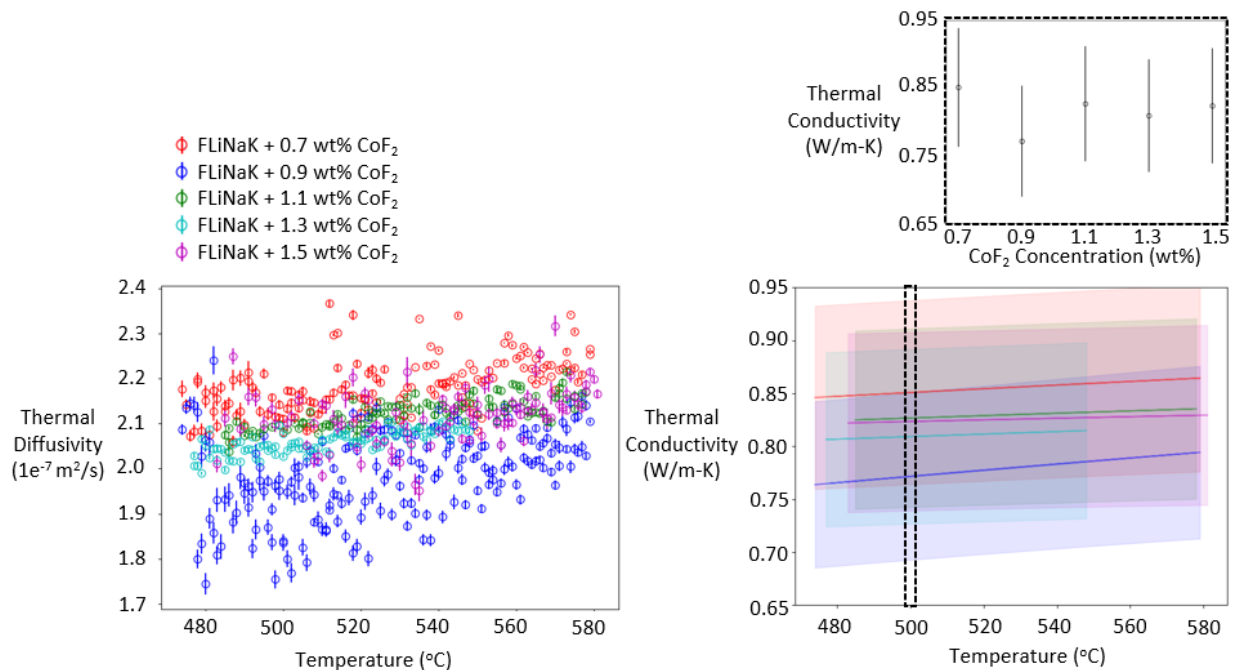
Figure 33. FLiNaK thermal diffusivity data obtained from TGS. (Left) Individual data points for 5 different FLiNaK samples (legend). Data points represent the fitting parameter and associated standard error of the TGS signals (average of 10,000 grating formation and decays). (Right) The converted line of best fit from the thermal diffusivity data using recommended correlations for FLiNaK density (ρ= 2579 - 0.624 $\cdot$ T[K] in kg/m3) and heat capacity (C_P = 1884 in J/kg-K) [10].Uncertainty (shaded region) represents the propagated 95% confidence interval of the fit, along with a 2% and 10% uncertainty for density and heat capacity respectively. (Right Cutaway) Thermal conductivity at 500°C vs CoF$_2$ concentration, showing the lack of trend at these concentration and uncertainty levels.

Larger spreads in the obtained thermal diffusivity values were observed for the data sets that had the lowest (0.7 and 0.9wt%) CoF_2 concentrations. For the 0.7 and 0.9wt% CoF_2 samples, a reduced signal to noise ratio was observed, indicating that potentially not enough pump light was absorbed to produce a strong grating. Comparison of the line of best fit for each sample (Right of Figure 33) highlights that no clear trend with $[CoF_2]$ is present, and that the variation of the different data sets is most likely representative of an estimate of the measurement's systematic error. Although the data sets do vary slightly in magnitude, a consistent feature is the presence of a slightly positive temperature coefficient.

Subtracting the maximum radiative contribution (Figure 29) from the line of best fit for the combined data of the five FLiNaK samples (Figure 34), shows that even a conservative estimate of the role of radiation cannot account for the small positive temperature coefficient that has been observed. The remainder of the thesis will discuss the validity of the FLiNaK results and offer potential explanations for why current theoretical models and experimental data remain in contradiction regarding the temperature dependence of fluoride molten salt thermal conductivity.
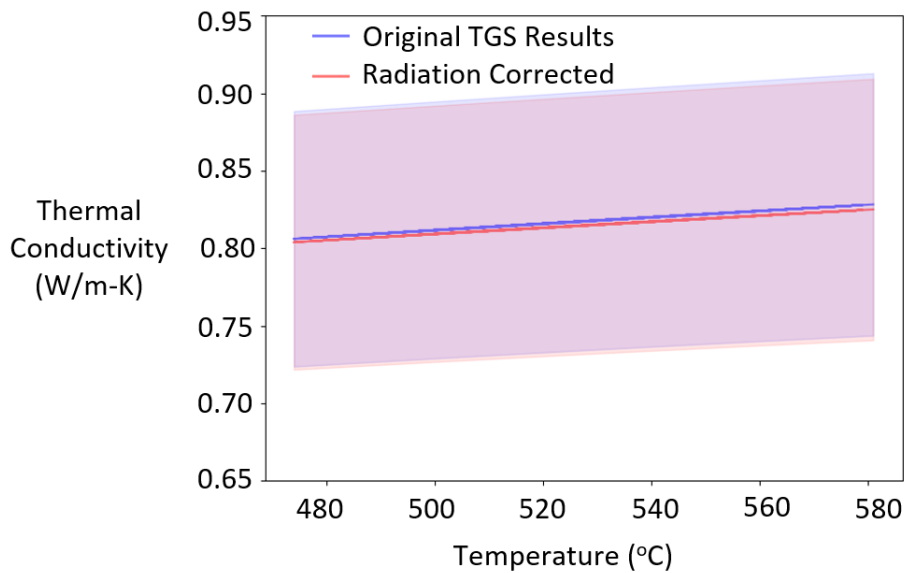
Figure 34. The combined thermal conductivity for the five FLiNaK samples with and without subtraction of the maximum potential radiative contribution (Figure 29). The shaded region represents a propagated error of approximately 10 %.

4.3   CFD modeling of laser flash as a means of validating TGS results

To further assess the validity of the TGS-obtained FLiNaK thermal conductivity values (Section 4.2), a critical analysis of the most recent published FLiNaK results [8] (acquired using Laser Flash

Analysis, LFA) was undertaken. Although it has been highlighted in Section 1.5, recall that LFA was primarily developed for opaque solids, where the energy from a laser is deposited in a very thin layer on the sample's surface. Samples are typically designed to be very thin, allowing for axial heat transfer to dominate. The raw data obtained in LFA is the temperature response of the side opposite to the energy deposition. Similarly, to TGS, thermal diffusivity information is obtained by fitting the transient temperature response to an equation that describes the heat transfer through the sample. As the technique has been primarily used for opaque solids, most fitting equations that have been developed do not account for potential contributions from convection and radiation to heat transfer through the sample [73], nor can they capture erroneous heat conduction paths introduced from different crucible designs.

The recent LFA experiments [8] were replicated in the commercial finite volume CFD solver STAR-CCM+ [74]. The geometry of the crucible and salt cavity are illustrated Figure 35 (Left). One fourth of the circular domain was simulated, with symmetry conditions applied to represent the full domain. Crucible dimensions and material properties were taken from the experiment (except for salt thermal conductivity, which was set to 0.8 W/m-K). Exterior boundary conditions were set to radiative and convective, with the experiment's initial temperature used as the environmental temperature. The heat transfer coefficient for the crucible exterior was set to 1 W/m^2-K and the emissivity to 0.5, although sensitivity to these parameters was very low due to small temperature differences. Conjugate heat transfer was applied to solve the energy equation in both the fluid and solid portions of the domain. A trapezoidal heat pulse of 2.5 J was applied to the bottom crucible surface to replicate the experimental laser heat flux. Laminar heat transfer was applied in the fluid domain, and temperature-dependent salt density was applied to account for buoyancy effects. (In some simulation scenarios, to test sensitivity, convection was eliminated by removing gravity). The fluid momentum and energy transport equations were integrated with a second-order upwind scheme. A hybrid Gauss-least square method was used for computing reconstruction gradients, with the Venkatakrishnan's reconstruction gradient limiter [75]; time integration was achieved with a second order accurate three-time level backward Euler method.

To facilitate LFA for molten salts, previous efforts have sandwiched the salt sample between layers of graphite, with a small empty volume near the periphery of the crucible allowing for salt expansion as temperature is increased (Figure 35 (Left)) [8]. Regardless of the potential contributions from radiation and convection for this geometry, it was observed that since graphite has a higher thermal conductivity than FLiNaK, heat is initially transferred radially and up the sides of the crucible (Figure

35 (Right)). Consequently, the temperature rise measured at the top center of the domain is slowed, as the open volume necessary for salt expansion acts as a thermal insulator. The model used to determine thermal diffusivity in these measurements assumes rapid axial heat transfer through the bulk of the sample [73]. Artificially slowing temperature rise as a result of the crucible design would likely lead to underestimations of the salt's thermal conductivity.
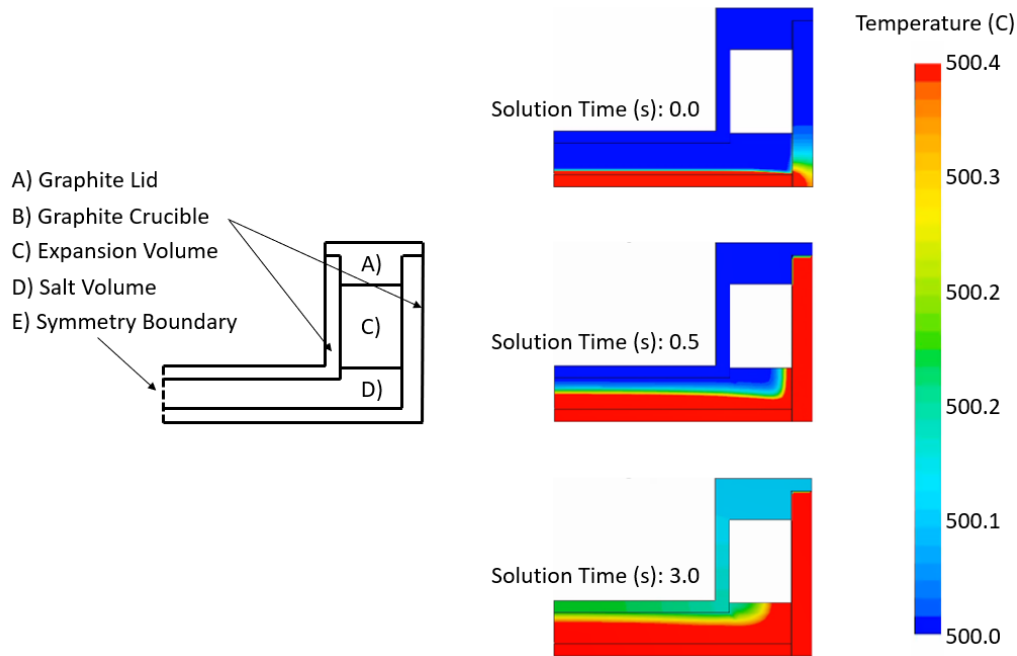
Figure 35. (Left) The geometry used for CFD modeling of FLiNaK laser flash thermal conductivity measurements. (Right) Temperature maps as a function of time for the simulated laser flash measurements, highlighting the unaccounted-for heat transfer up the side walls of the graphite crucible.

To provide further evidence for the potential underestimation, an idealized three-layer (graphite-salt-graphite) slab was simulated alongside the crucible. Comparison of the temperature response for the two geometries shows that the crucible does experience a reduced rate of axial heat transfer, resulting in a temperature profile that is shifted down and to the right (Figure 36).
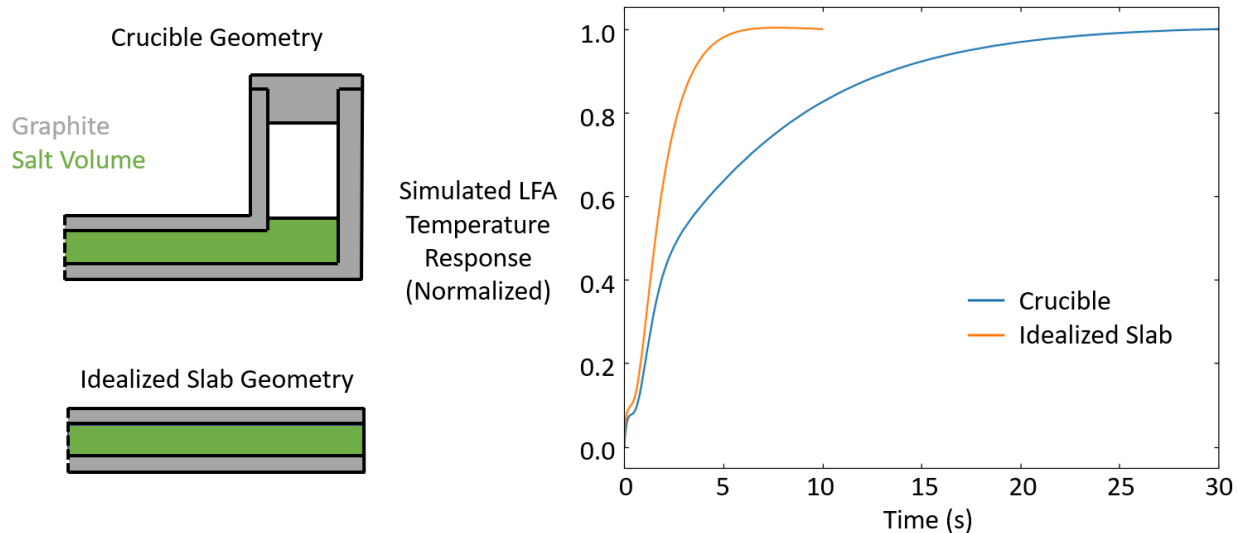
Figure 36. (Left) The slab and crucible geometries used in the simulations; more details of the crucible geometry can be found in Figure 35. (Right) Normalized sample surface temperature rise for the CFD simulated laser flash measurements in FLiNaK, measured at the top center of the domain for both the crucible and idealized slab geometries.
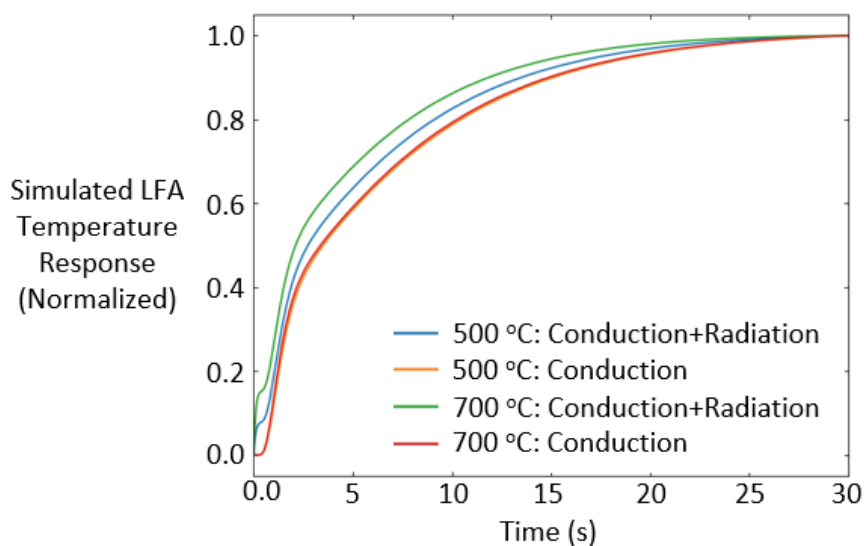
Figure 37. Normalized sample surface temperature rise for the CFD simulated laser flash measurements in FLiNaK, measured at the top center of the domain. Simulations have been run with and without the radiative heat transfer at two different temperatures (legend), highlighting the potential impact of radiation in this geometry.

Despite the potential flaws associated with the crucible design, an assessment of the potential contributions of radiation and convection for this geometry was still performed. The LFA measurements were simulated with and without convective and radiative heat transfer. The inclusion of convection was shown to play no role in modifying the temperature response of the sample's surface, however, simulating radiation did lead to deviations from the pure conduction reference case (Figure 37).

As the thermal conductivity of FLiNaK was taken as a constant (0.8 W/m-K), simulated results (Figure 37) for the pure conduction case were equivalent across the temperatures that were modeled (500 and 700 °C). The addition of radiation led to faster heat transfer through the molten salt, increasing in magnitude as temperature increased. Directionally, the contributions of radiation in this geometry would indicate that a larger positive temperature coefficient would be expected for LFA in comparison to a technique where radiation has been shown to be negligible (i.e. TGS, Section 3).
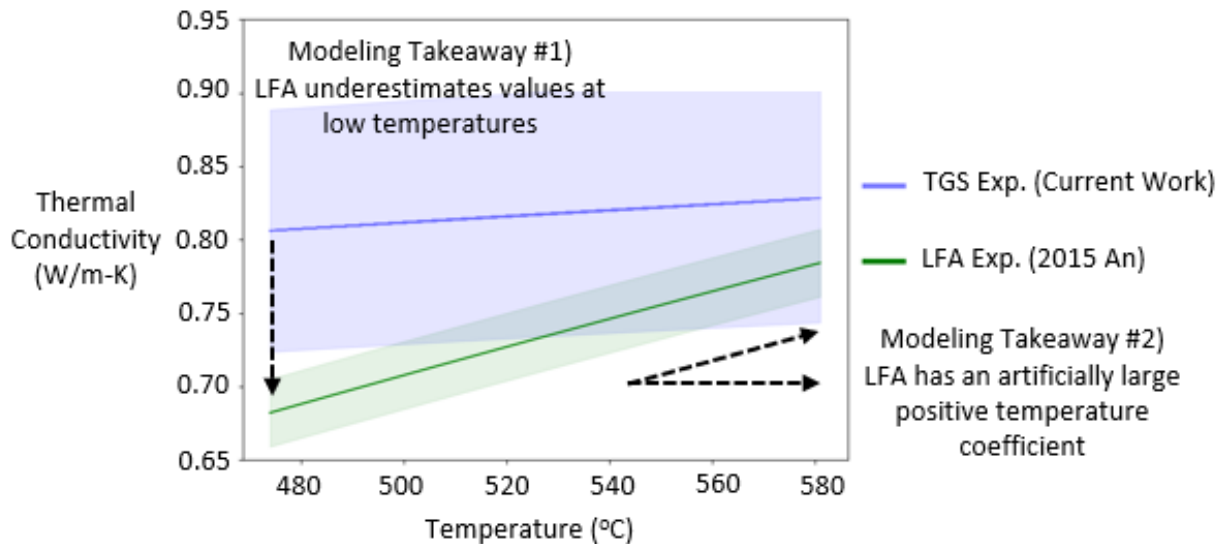
Figure 38. A comparison of TGS (current work) and LFA thermal conductivity measurements for FLiNaK, highlighting the consistency of the TGS results with the conclusions from the LFA modeling work. TGS results have been reported as the line of best fit for the 5 samples analyzed (0.7, 0.9, 1.1, 1.3 and 1.5wt% CoF_2) including a roughly 10% uncertainty (shaded region). LGA results are taken from 2015 An [8] and include the reported +/-0.023 W/m-K uncertainty (shaded region).

As the raw temperature response data from the LFA measurements is not available, two qualitative conclusions can be drawn from the modeling of the proposed molten salt LFA geometry [8]. Firstly,

heat transfer up the side walls of the crucible is not accounted for in the fitting function used to obtain thermal diffusivity results experimentally. Artificially slowing axial heat transfer due to the presence of a dominant radial path would likely lead to underestimation of the salt's thermal conductivity (particularly at low temperatures). Secondly, radiation is likely to play a significant role within the heat transfer of this LFA geometry. Contributions from radiation to heat transfer through the sample increase with temperature, leading to a larger positive temperature coefficient than what would be present in the absence of radiation (TGS measurements).

Comparison of the TGS and LFA experimental results (Figure 38) highlights the consistency of the values obtained from TGS if the LFA measurements were corrected for the errors highlighted in the CFD modeling work (i.e. crucible design and contributions from radiation).

4.4   Magnitude of the theoretical thermal conductivity temperature coefficient

Although the modeling work associated with LFA measurements (Section 4.3) provides some evidence to support the validity of the TGS results (Section 4.2), it is still necessary to address the small positive temperature coefficient that has been observed. As discussed in the Introduction (Section 1.3), positive temperature coefficients contradict the current theoretical understanding of heat conduction in molten salts. However, common explanations (contributions from radiation and convection) for experimentally observed positive temperature coefficients have been shown to not be applicable for the TGS measurements. Alternative potential explanations for the existence of a positive temperature coefficient are presented in Section 5, however, prior to this discussion, the absolute magnitude of the theoretical coefficient should be addressed.

Recall from Section 1.3 that in addition to the distance between atoms or the density of the salt, sound speed has also found its way into many of the theoretical models of molten salt thermal conductivity [25] [76]. A large ratio of thermal to mass diffusivity, and large Lorenz number (proportional to the ratio of thermal to electrical conductivity) [27], has been taken as evidence that molten salts conduct heat primarily via a vibrational mechanism (as opposed to diffusive movement of the salt's ions). Early models proposed that salts could be thought of as having a quasi-lattice structure, with energy being transferred between atoms at the speed of sound [25]. More recent models leverage similar assumptions, however, the expressions have ultimately been presented using the salt's Gruneisen parameter (a function of sound speed that describes how changes in volume affect vibrational properties) [77]. The accuracy of these models hinges on the availability

of accurate sound speed measurements in the salts of interest, a body of literature for fluorides that is potentially even more sparse than the data on thermal conductivity [6].
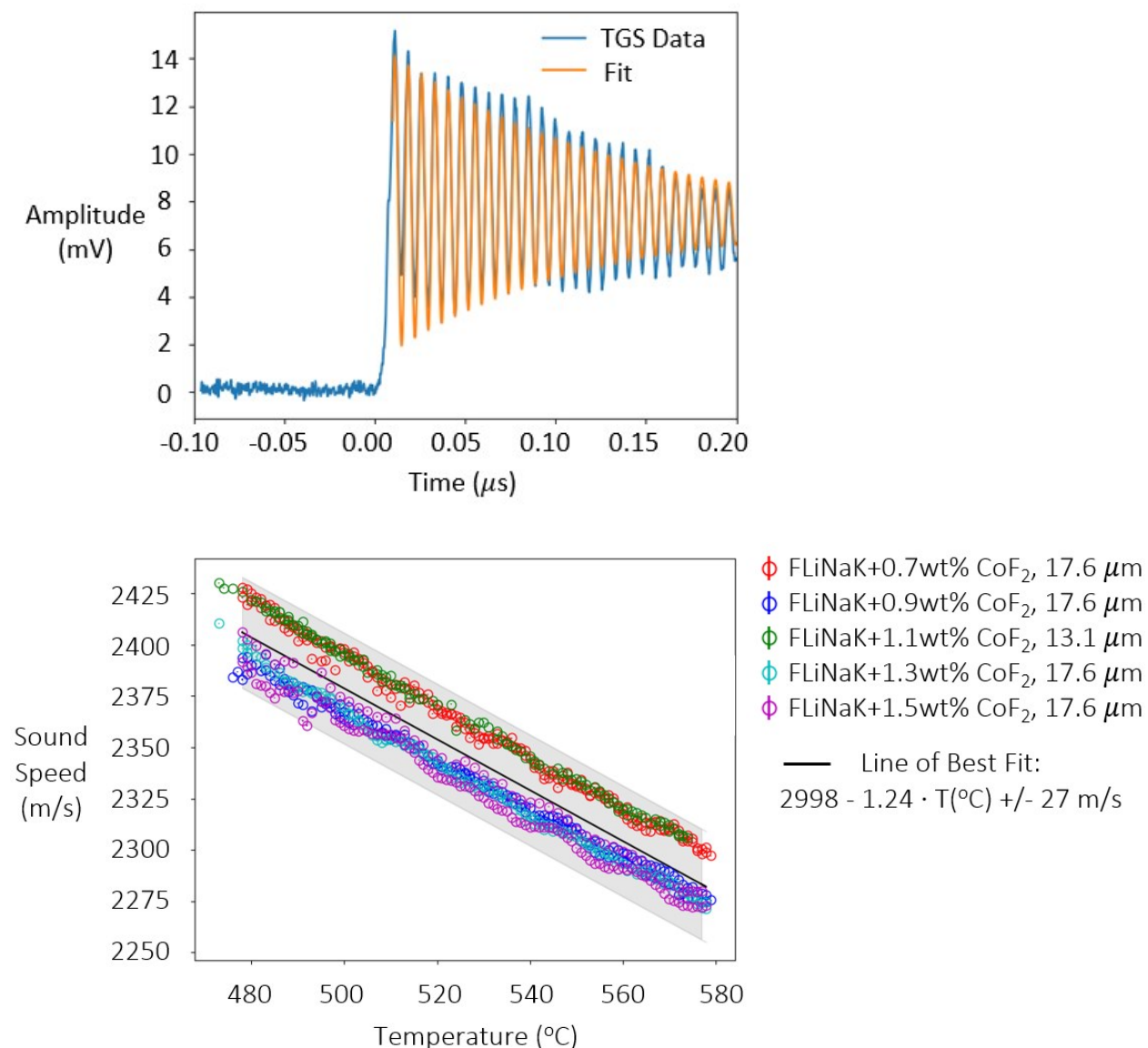
Figure 39. (Top) Raw short timescale TGS signal (blue) for FLiNaK at 483°C along with the fit of the signal (orange) used to extract the salt's sound speed. Raw signal represents the average of 10,000 grating formation and decays. (Bottom) Sound speed data as a function of temperature for the 5 samples analyzed (0.7, 0.9, 1.1, 1.3, and 1.5wt% CoF_2). The equation for a line of best fit for the accumulative data is also included (2998 – 1.24 · T (°C) +/- 27 m/s) along with a 95% prediction interval (shaded region). Grating spacings for the five samples are presented in the legend.

As discussed earlier, TGS also results in acquisition of the salt's sound speed due to oscillations in the induced density grating over short timescales. The top graph of Figure 39 presents a typical short timescale signal that has been observed in FLiNaK, highlighting the well-defined oscillation frequency that is used to determine sound speed. Similarly to thermal conductivity, sound speed data was obtained for all five FLiNaK samples (0.7 to 1.5 wt% CoF_2), with no trends in CoF_2 concentration being observed. A slight deviation between the 1.1 wt% CoF_2 sample that was obtained using a different grating spacing is curious, however as it has good agreement with the 0.7 wt% CoF_2 sample, it does not provide clear evidence that a dependance length scale has been observed. Additional dedicated temperature dependent trials to examine the influence of grating spacing are the subject of a future research direction discussed further in section 6.2. The acquisition of sound speed results in FLiNaK (Figure 39 (Bottom)) are to the author's best knowledge the first time that sound speed has been measured within this salt composition
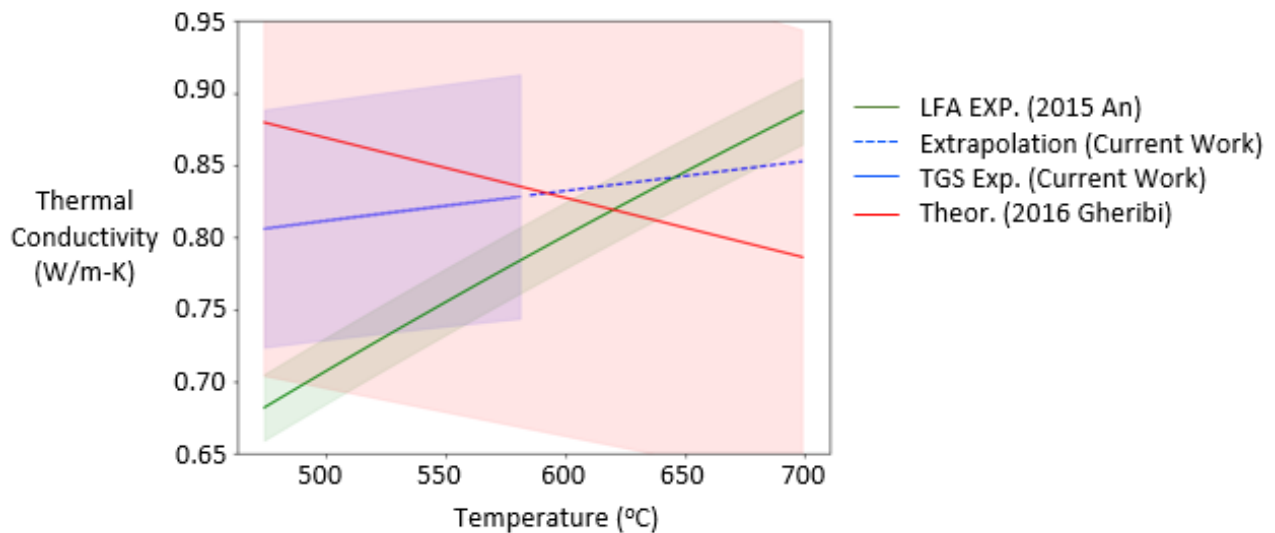
Figure 40. A comparison of theoretical and experimental (TGS and LFA) FLiNaK thermal conductivity results. For TGS a roughly +/- 10 % uncertainty (shaded region) is shown along with a line of best fit for the combined 0.7, 0.9, 1.1, 1.3, and 1.5 CoF_2wt% data. LGA results are taken from 2015 An [8] and include the reported +/-0.023 W/m-K uncertainty (shaded region). Theoretical estimates are taken from 2016 Gheribi [11] and include a +/- 20 % uncertainty (shaded region) as suggested in a previous publication [77].

Up until now, experimental sound speed data has not been available for FLiNaK. Models that require sound speed have relied on estimates based on data from FLiNaK's constituents [78]. Despite this,

comparison of the most recent theoretical FLiNaK thermal conductivity estimates and the experimental data from TGS are in relatively good agreement (Figure 40), considering the expected uncertainty of the model (+/- 20 %) [77]. However, as the temperature coefficient for the two results (Theory and TGS experiments) have different signs, the agreement is not expected to hold at extremely elevated temperatures.

The theoretical logic that justifies the expected presence of a negative thermal conductivity temperature coefficient for molten salts does not by itself indicate the magnitude of the coefficient. Reliable experimental data from non-fluoride salts does show a strong temperature dependence, however, the fluoride salt experimental data that has been deemed reliable enough for theoretical comparison (Figure 4) is largely flat, if not slightly increasing with increasing temperature.

A reduced magnitude (even if still negative) for the theoretical estimate of FLiNaK's thermal conductivity temperature coefficient would offer better agreement with the experimental results from TGS. Justification for this reduced magnitude in the context of the most recent theoretical model (Eq 31) would likely come from overestimates of the thermal conductivity (λ_{fus}) and sound speed (v_{fus}) at the melting point [77].

$$\frac{\partial \lambda}{\partial T} = -\lambda_{fus} \alpha_{fus} \left(\frac{\alpha_{fus} M_W v_{fus}^2}{C_{P,fus}} + \frac{1}{3} \right)$$

Eq 31

For FLiNaK, a theoretical thermal conductivity temperature coefficient of approximately $-4 \cdot 10^{-4}$ W/m-K^2 has been proposed. This result implies a value of 0.89 W/m-K for the thermal conductivity and 2808 m/s for the sound speed at the melting point (when considering a molecular weight (M_W), thermal expansion coefficient (α_{fus}), and molar heat capacity ($C_{P,fus}$) of 0.04129 kg/mol, $2.94 \cdot 10^{-4}$ K^{-1} and 77.79 J/mol-K respectively [79]). If the TGS results for thermal conductivity (0.80 W/m-K) and sound speed (2434 m/s) at the melting point are instead used, the theoretical coefficient drops to roughly $-2.9 \cdot 10^{-4}$ W/m-K^2 (a 27% reduction).

In addition to reductions from the model's inputs, a potential error in the derivation of the model may reduce the magnitude of the coefficient further. The thermal conductivity model proposed by Gheribi et al [77] begins by expressing the temperature dependence of thermal conductivity at constant pressure using a change of path.

$$\left(\frac{\partial \ln \lambda}{\partial T} \right)_P = \left(\frac{\partial \ln \lambda}{\partial T} \right)_\rho + \left(\frac{\partial \ln \lambda}{\partial \ln \rho} \right)_T \left(\frac{\partial \ln \rho}{\partial T} \right)_P$$

Eq 32

The derivation then uses an observation from MD simulations [33] [80] that in the absence of a change in density, molten salt thermal conductivity is relatively unaffected by changes in temperature.

$$\left(\frac{\partial ln\lambda}{\partial T}\right)_{\rho} = 0 \qquad \text{Eq 33}$$

Using this assumption, the initial expression (Eq 32) simplifies to Eq 34.

$$\left(\frac{\partial \ln \lambda}{\partial T}\right)_P = \left(\frac{\partial \ln \rho}{\partial T}\right)_P \left(\frac{\partial \ln \lambda}{\partial \ln \rho}\right)_T \qquad \text{Eq 34}$$

A simple model of energy transfer in a quasi-lattice structure [81] is then assumed, where thermal conductivity can be approximated as Eq 35.

$$\lambda = \sqrt{2} v c_V a^{-1} \rightarrow \lambda \propto v \rho^{1/3} \qquad \text{Eq 35}$$

Substituting in this relation yields Eq 36.

$$\left(\frac{\partial \ln \lambda}{\partial T}\right)_P = \left(\frac{\partial \ln \rho}{\partial T}\right)_P \left(\frac{\partial \ln v\rho^{\frac{1}{3}}}{\partial \ln \rho}\right)_T = \left(\frac{\partial \ln \rho}{\partial T}\right)_P \left(\left(\frac{\partial \ln v}{\partial \ln \rho}\right)_T + \frac{1}{3}\left(\frac{\partial \ln \rho}{\partial \ln \rho}\right)_T\right)$$
$$= \left(\frac{\partial \ln \rho}{\partial T}\right)_P \left(\left(\frac{\partial \ln v}{\partial \ln \rho}\right)_T + \frac{1}{3}\right) \qquad \text{Eq 36}$$

The next step in the derivation (integration of the expression) is where a potential error is introduced.

$$\int \left(\frac{\partial \ln \lambda}{\partial T}\right)_P dT = \int \left(\frac{\partial \ln \rho}{\partial T}\right)_P \left(\left(\frac{\partial \ln v}{\partial \ln \rho}\right)_T + \frac{1}{3}\right) dT \qquad \text{Eq 37}$$

Gheribi et al. suggest integration of the Eq 37 results in Eq 38, which can be rearranged to Eq 39.

$$ln\left(\frac{\lambda(T)}{\lambda(T_0)}\right) = \left(\frac{\partial \ln \rho}{\partial T}\right)_P \left(\left(\frac{\partial \ln v}{\partial \ln \rho}\right)_T + \frac{1}{3}\right)(T - T_0) \qquad \text{Eq 38}$$

$$\lambda(T) = \lambda(T_0) e^{\left(\frac{\partial \ln \rho}{\partial T}\right)_P \left(\left(\frac{\partial \ln v}{\partial \ln \rho}\right)_T + \frac{1}{3}\right)(T-T_0)} \qquad \text{Eq 39}$$

A Taylor expansion of the exponential and differentiation yields Eq 40, with differentiation with respect to temperature resulting in Eq 41.

$$\lambda(T) = \lambda(T_0)\left(1 + \left(\frac{\partial \ln \rho}{\partial T}\right)_P \left(\left(\frac{\partial \ln v}{\partial \ln \rho}\right)_T + \frac{1}{3}\right)(T - T_0)\right) \qquad \text{Eq 40}$$

$$\frac{\partial \lambda(T)}{\partial T} = \lambda(T_0)\left(\frac{\partial \ln \rho}{\partial T}\right)_P \left(\left(\frac{\partial \ln v}{\partial \ln \rho}\right)_T + \frac{1}{3}\right) \qquad \text{Eq 41}$$

However, the integration step assumes the entire function on the right side is independent of temperature. Instead, integration of the partial derivative of the density should return the density. An updated integration and rearrangement follows from Eq 42 to Eq 45.

$$\ln\left(\frac{\lambda(T)}{\lambda(T_0)}\right) = \ln\frac{\rho(T)}{\rho(T_0)}\left(\left(\frac{\partial \ln v}{\partial \ln \rho}\right)_T + \frac{1}{3}\right) \qquad \text{Eq 42}$$

$$\lambda(T) = \lambda(T_0)\left(\frac{\rho(T)}{\rho(T_0)}\right)^{\left(\left(\frac{\partial \ln v}{\partial \ln \rho}\right)_T + \frac{1}{3}\right)} \qquad \text{Eq 43}$$

$$\frac{\partial \lambda(T)}{\partial T} = \frac{\lambda(T_0)\left(\left(\frac{\partial \ln v}{\partial \ln \rho}\right)_T + \frac{1}{3}\right)\left(\frac{\partial \rho(T)}{\partial T}\right)\left(\frac{\rho(T)}{\rho(T_0)}\right)^{\left(\left(\frac{\partial \ln v}{\partial \ln \rho}\right)_T + \frac{1}{3}\right)}}{\rho(T)} \qquad \text{Eq 44}$$

$$\frac{\partial \lambda(T)}{\partial T} = \lambda(T_0)\left(\left(\frac{\partial \ln v}{\partial \ln \rho}\right)_T + \frac{1}{3}\right)\left(\frac{\partial \ln \rho}{\partial T}\right)_P\left(\frac{\rho(T)}{\rho(T_0)}\right)^{\left(\left(\frac{\partial \ln v}{\partial \ln \rho}\right)_T + \frac{1}{3}\right)} \qquad \text{Eq 45}$$

Dividing the updated coefficient (Eq 45) over the original coefficient (Eq 41) yields Eq 46.

$$\frac{\left(\frac{\partial \lambda(T)}{\partial T}\right)_{\text{Updated}}}{\left(\frac{\partial \lambda(T)}{\partial T}\right)_{\text{Original}}} = \left(\frac{\rho(T)}{\rho(T_0)}\right)^{\left(\left(\frac{\partial \ln v}{\partial \ln \rho}\right)_T + \frac{1}{3}\right)} \qquad \text{Eq 46}$$

This factor is less than one (approximately 0.9) and decreases as temperature increases, indicating that the original theoretical coefficient is likely further overestimated particularly at high temperatures. This adjustment is not enough to elicit full agreement with the experimental results

from TGS, however, it may provide sufficient conformity over the temperature range of interest for fluoride salt-based energy applications (500 to 700ºC).

5. The positive temperature coefficient of fluoride molten salt thermal conductivity

Parts of this chapter have been reproduced from S. G. Robertson, R. Wiser, W. Yang, S. Choi, E. Bagletto and M. P. Short, "The Curious Tempertaure Dependence of Fluoride Molten Salt Thermal Conductivtiy" Journal of Applied Physics, 2022, with the permission of AIP Publishing

5.1 The role of vapor pressure in multi-constituent salts

Although a reduced magnitude (even if still negative) of the theoretical temperature coefficient offers better agreement with the experimental results from TGS, a physical hypothesis for why the signs of the temperature coefficient are in contrast is still required. One possible explanation for why positive coefficients may be observed experimentally is changes in salt composition as a function of temperature or time. Non-reversible mechanisms such as evaporation and deposition away from the salt, or continuous reactions with salt contacted materials have been ruled out, as data taken during the initial heating and subsequent cooling of the salt samples are consistent (Figure 41). However, temperature dependent-reversible reactions may offer an explanation.
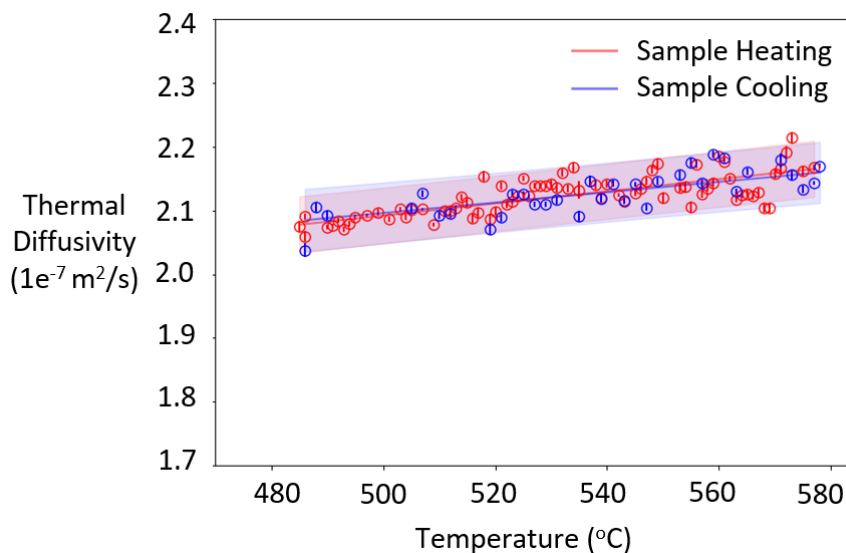
Figure 41. TGS Thermal diffusivity data for FLiNaK+1.1wt%CoF$_2$ taken during sample heating and cooling (legend). Data points represent the fitting parameter and associated standard error of the TGS signals (average of 10,000 grating formation and decays). Lines of best fit and 95% prediction intervals (shaded region) have been included, highlighting the consistency of the two data sets.

As highlighted in the LFA modeling work (Section 4.3), most experimental setups for measuring molten salt thermophysical properties require open volumes for the salt sample to expand into as temperature is increased. The salts in these systems are typically held under vacuum, or with an inert atmosphere cover gas. Open volumes shown in molten salt crucible designs are typically not the full space to which salt vapor may have access to, with small holes typically connecting the crucible to a larger system volume. Large open volumes above salt samples may allow for relative differences in the vapor pressure of salt constituents to play a role in reversible composition change as a function of temperature.

The vapor pressure (P) of the different constituents in FLiNaK (Figure 42 (Top)) has been measured recently as a function of temperature [82]. The partial pressure of the constituents in the gas phase is not proportional to the mol fraction of the species in the liquid phase, leading to changes in the mol fraction of the constituents remaining in the molten salt (Figure 42 (Bottom)).

To estimate the composition changes due to the differences in constituent vapor pressure, a characteristic exponential function (Eq 47) was fit to the experimental vapor pressure (P) vs temperature (T) data (using C_1 and C_2 as fitting constants). Fluorine was assumed to accompany alkali metals in the vapor phase, allowing for mols in the vapor to equal the moles lost in the liquid. Acting as a conservative estimate of the potential effect, the volume of the entire TGS vacuum chamber (0.004 m^3) was used along with the ideal gas law, to estimate the number of mols in the vapor phase.

$$P = C_1 e^{-C_2/T}$$ Eq 47

Figure 42 indicates that potassium fluoride is likely to be the largest contributor to FLiNaK's vapor pressure. As potassium fluoride is expected to have the lowest thermal conductivity of the three constituents [77], its relative loss as a function of temperature could lead to an increase in the thermal conductivity of the remaining salt. However, as the expected scale of the mol fraction change is extremely small ($1e^{-9}$), it is unlikely that this is responsible for the positive temperature coefficient that has been observed in TGS.
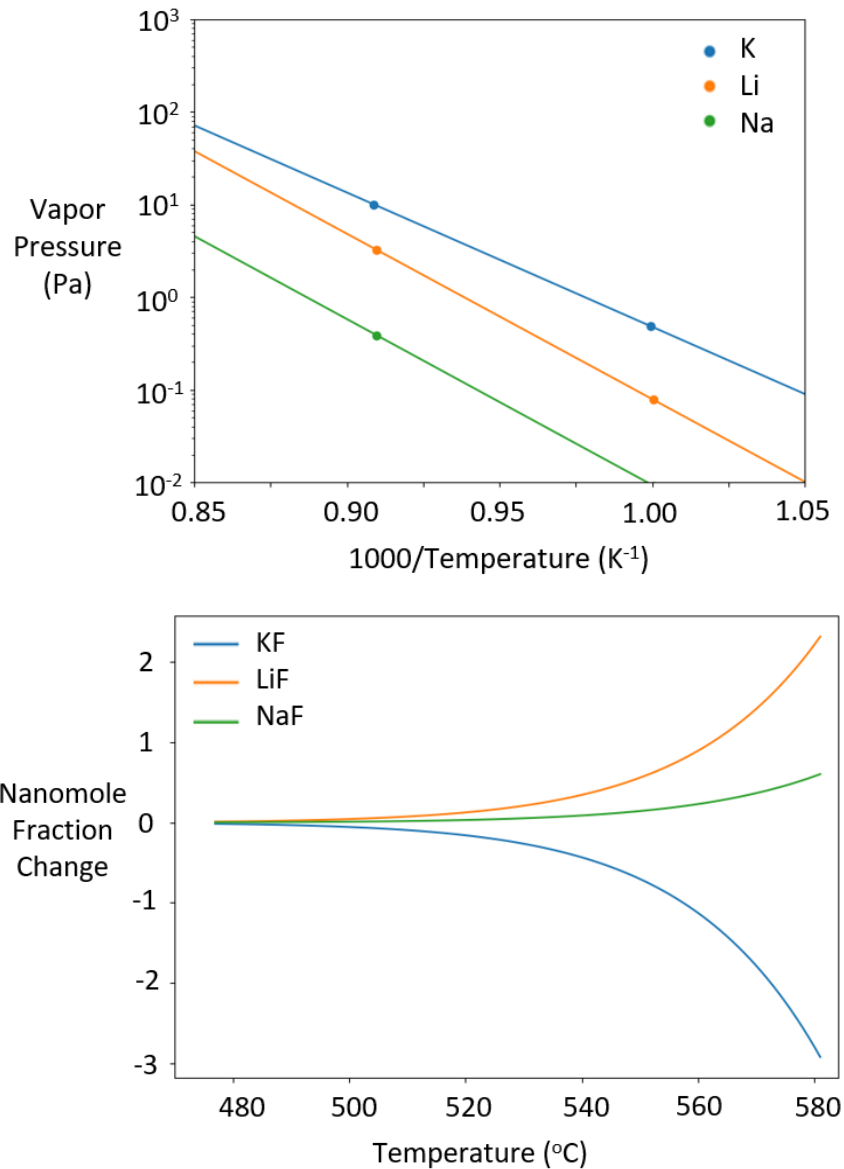
Figure 42. (Top) Experimental vapor pressure results (points) and an exponential fit (lines) for the constituents within FLiNaK [82]. (Bottom) Estimated mol fraction change as a function of temperature using the vapor pressure data (Top) and a vapor and salt volume of $4.0 \cdot 10^{-3}$ and $3.3 \cdot 10^{-6}$ m^3 respectively.

In contrast to existing vapor pressure data, early composition analysis of alternative FLiNaK samples showed a significant reduction in KF between the pre and post TGS samples. As a result of the observed composition change, subsequent FLiNaK measurements were held below 600°C in attempt to minimize evaporation-based losses. This result was however not repeatable, and subsequent composition analysis showed no clear trend in KF loss or gain (Figure 30). It is expected

that the significant loss of KF initially observed may have been due to heterogeneity in the samples sent for analysis. Additional trials of FLiNaK should be repeated at higher temperatures, measuring during both heating and cooling to confirm the point at which evaporation may begin to play a role.

Following the LiCl measurements large deposits of salt were observed on the lid of the graphite cell (Figure 43, not the case for FLiNaK). Deposition of salt on the lid of the cell is likely due to salt condensing from the vapor phase as the lid contains no insulation and is likely to cool more quickly than the cell walls and base once the heater has been turned off. As mentioned, the potential observation of high vapor pressures for single constituent salts is unlikely to influence the obtained thermal diffusivity results as no composition change has occurred, however, this may be a consideration for LiCl containing multi-constituent salts.
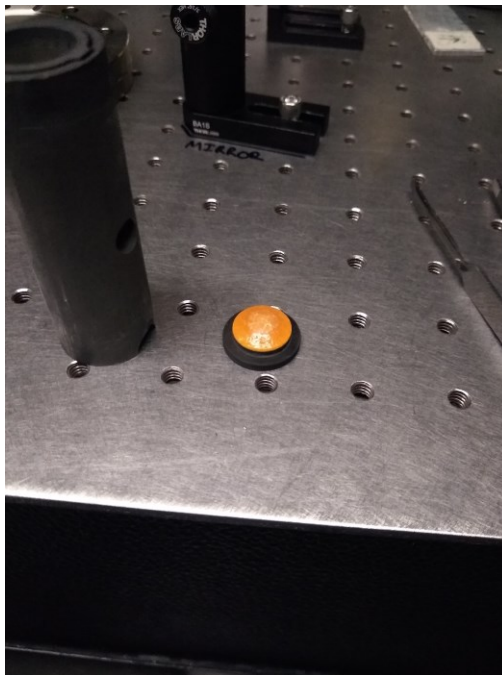
Figure 43. LiCl + 1wt%NiCl$_2$ deposits on the lid of the graphite cell following heating beyond 700°C and rapid cooling.

5.2   Uncertainty in heat capacity data

Another source of uncertainty comes through the conversion of thermal diffusivity (**D**) to conductivity (Eq 48). Although the density (**ρ**) of FLiNaK is well characterized, existing heat capacity (**C$_P$**) data varies substantially, even disagreeing on the sign of the property's temperature coefficient (Figure 44 (Top)) [79].

$$\lambda = D\rho C_P \qquad\qquad \text{Eq 48}$$
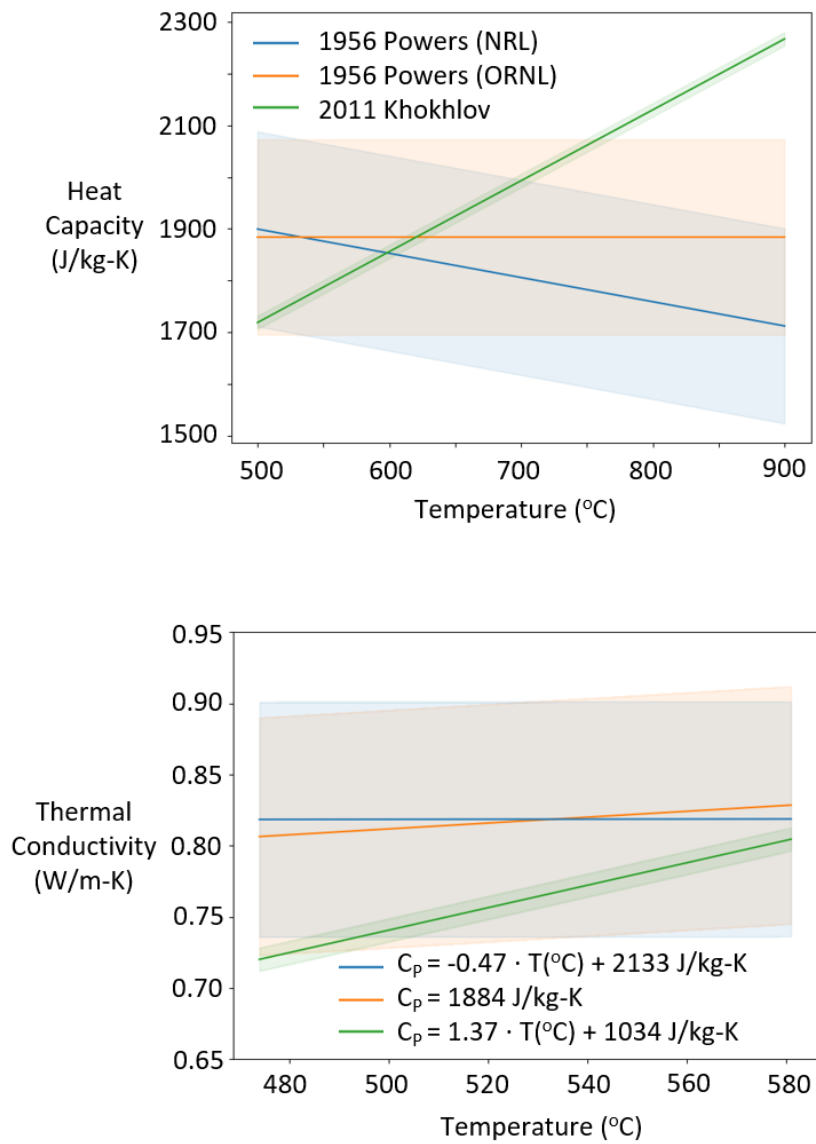
Figure 44. (Top) A selection of FLiNaK experimental heat capacity data that varies significantly in the sign of the temperature coefficient [83] [18]. (Bottom) The thermal conductivity of FLiNaK using TGS obtained thermal diffusivity data and the different expressions for heat capacity (Top) along with a density of ρ = 2579 – 0.624 ·T[K] kg/m³. Shaded region represents the propagated uncertainty from the heat capacity, density, and thermal diffusivity data.

If heat capacity does indeed decrease with temperature as some of the data shows [83], existing correlations are enough to convert the TGS obtained thermal diffusivity into a thermal conductivity

result that deceases with increasing temperature (Figure 44 (Bottom)). However, many of the more recent data sets have shown that heat capacity is flat to slightly increasing with increasing temperature [18], leading to even larger positive temperature coefficients for the converted thermal conductivity (Figure 44 (Bottom)).

5.3   The validity of neglecting diffusive contributions

As a final potential explanation for experimentally observed positive thermal conductivity temperature coefficients, the validity of theoretical model assumptions for fluoride molten salts is examined. As discussed in the introduction, a characteristic of almost all theoretical models is the assumption that diffusive contributions can be considered negligible compared to the role of vibrational interactions between neighboring ions. As a review from the introduction, the diffusive contribution to thermal conductivity can be approximated by Eq 7, where a is a constant (typically 2), D_m is the mass diffusivity, C_V is the heat capacity and l is the spacing between atoms.

$$\lambda_{diff} = \frac{aD_mC_V}{l^3} \qquad\qquad Eq\ 7$$

By itself, the diffusive contribution has a positive temperature coefficient, as the product of diffusivity and heat capacity typically grows faster than the molar volume (l^3) as temperature increases (similar to what is observed for gases). However, to determine if this is enough to outweigh the decreasing vibrational component and subsequently whether the answer would be salt specific, it is necessary to evaluate Eq 7 quantitatively.

Figure 45 highlights the expected diffusion coefficients for the two molten salts examined in this thesis (LiCl and FLiNaK), salts that have shown contrasting temperature dependences when their thermal conductivity is determined from TGS measurements. As a first approximation, an average coefficient for the different ions in the salt can be used in Eq 7, with LiCl and FLiNaK being taken as $2.3859 \cdot 10^{-11} \cdot T[K] - 1.555 \cdot 10^{-8}$ and $1.4128 \cdot 10^{-11} \cdot T[K] - 1.0392 \cdot 10^{-8}$ m^2/s respectively [84] [85]. To calculate the spacing between atoms or molar volume of the salt, the molar mass (M_{LiCl} = 42.39 g/mol and M_{FLiNaK} = 41.29 g/mol), and density can be used ($l^3 = M/\rho$), with LiCl and FLiNaK densities being take as $1884 - 0.4328 \cdot T[K]$ and $2579 - 0.624 \cdot T[K]$ kg/m^3 respectively [24] [10]. Heat capacities can be taken as constants (C_{LiCl} = 62.35 J/mol-K and C_{FLiNaK} = 77.79 J/mol-K) and a value of 2 can be used for a as is the case for some derivations [27].
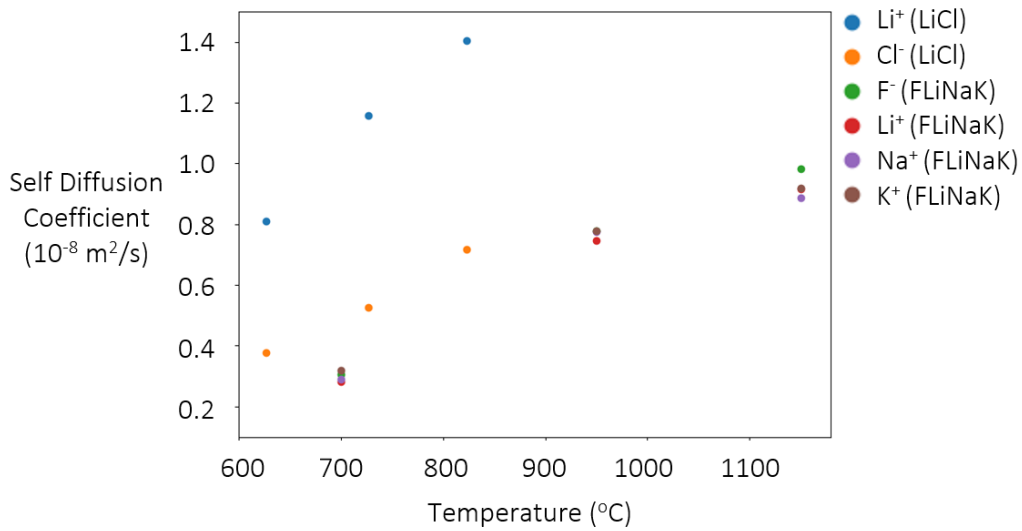
Figure 45. Simulated self-diffusion coefficients for the ions present ions present in LiCl [84] and FLiNaK [85].
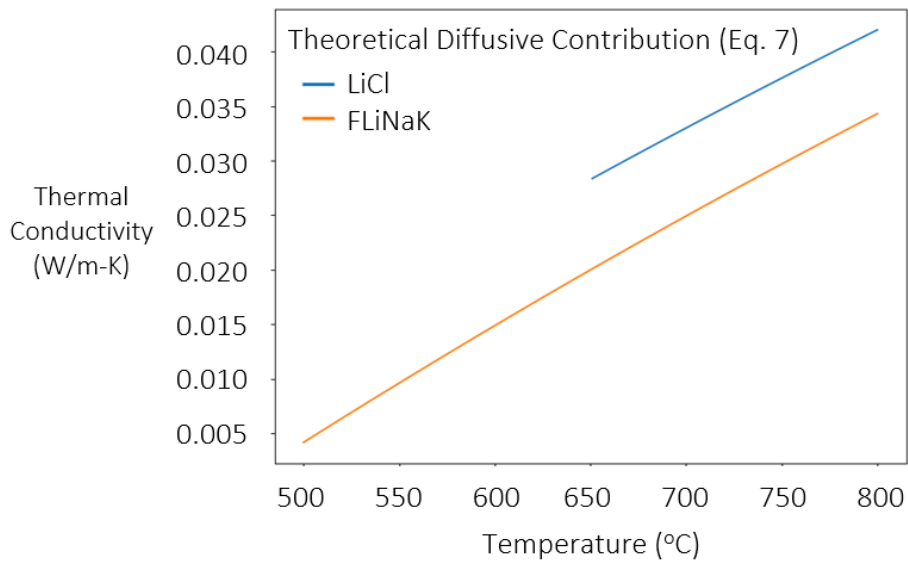
Figure 46. Theoretical diffusive contribution to thermal conductivity (Eq 7) for LiCl and FLiNaK. Diffusion coefficients have been taken as an average of the ions present $2.3859 \cdot 10^{-11} \cdot T[K] - 1.555 \cdot 10^{-8}$ and $1.4128 \cdot 10^{-11} \cdot T[K] - 1.0392 \cdot 10^{-8}$ m^2/s for LiCl and FLiNaK respectively [84] [85]. Salt density is taken as $1884 - 0.4328 \cdot T[K]$ and $2579 - 0.624 \cdot T[K]$ kg/m^3 for LiCl and FLiNaK respectively [24] [10]. Heat capacities are taken as constants (C_{LiCl} = 62.35 J/mol-K and C_{FLiNaK} = 77.79 J/mol-K) and a value of 2 is used for **a** [27].

Using the aforementioned property values, Eq 7 can be evaluated as a function of temperature (

Figure **46**). These values show the characteristic positive temperature coefficient that is expected for diffusion controlled thermal conduction.

To provide context to the proposed theoretical model adjustments that have been discussed (i.e. updated sound speed and thermal conductivity at the melting point (Section 4.4), updated derivation for the theoretical coefficient (Section 4.4), and inclusion of diffusive contributions (Section 5.3)), the original theoretical model from Gheribi et al [11] is shown with successive corrections alongside the TGS experimental data for FLiNaK (Figure 47).
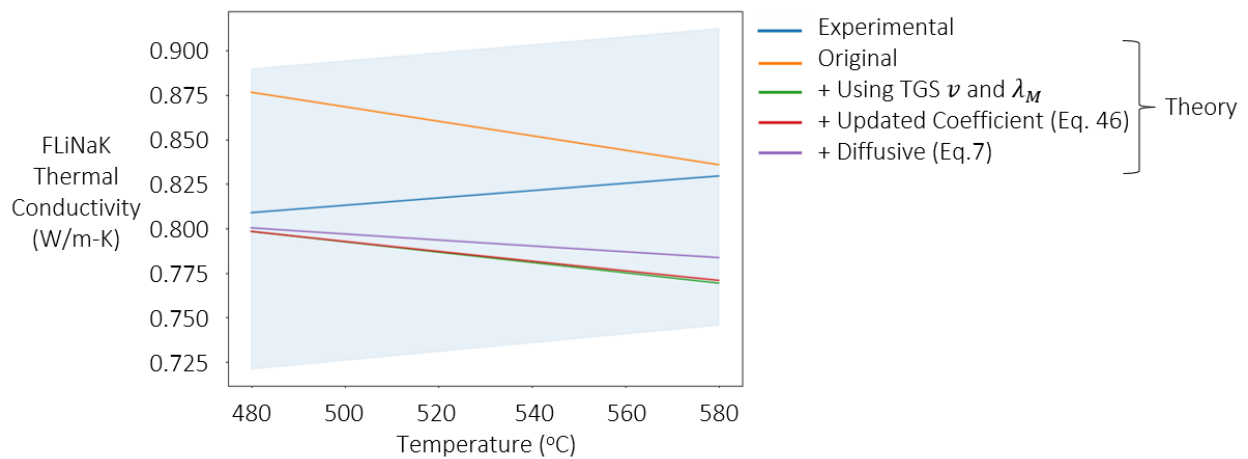
Figure 47. A comparison of the original theoretical model for FLiNaK thermal conductivity from Gheribi et al [11], along with cumulative corrections based on using TGS determined sound speed (2968 - 1.2·T [ºC]) and melting point thermal conductivity (0.8055 W/m-K), an updated derivation for the theoretical temperature coefficient (Eq 46), and the addition of diffusive contributions (Eq 7 and Figure 46). Experimental data for the thermal conductivity of FLiNaK determined from TGS (Section 4.2) is also shown along with a +/- 10% uncertainty.

Figure 47 highlights that although adjustments to the theoretical model of thermal conductivity provide better agreement with the experimental results from TGS, a continued contrast in the sign of the temperature coefficient remains. Theoretical reductions along with the uncertainty in experimental heat capacity data (Section 5.2) provide evidence to support the fact that fluoride molten salt thermal conductivity is likely weakly temperature dependent. However, further explanations and evidence are required to address why TGS, or theoretical models, are unable to

capture the correct sign of the temperature dependance for fluoride molten salt thermal conductivity.

6.   Conclusions and Future Directions

6.1   Conclusions

For fluoride salt-based technologies to play a significant role in the future energy landscape, accurate salt property data is required (Section 1.1). To date, existing thermal conductivity measurements have been plagued by large uncertainties and a curious positive temperature coefficient (Section 1.2). Theoretical models of molten salt thermal conductivity indicate that thermal conductivity should decrease as a function of temperature, consistent with the trends observed in other simple fluids (Section 1.3). Contradictions between theory and experimental data have been hypothesized to be the result of experimental technique's inability to isolate a single mode of heat transfer. Unaccounted for contributions from radiation and convection would likely lead to the erroneous observation of a positive temperature coefficient for thermal conductivity measurements, as both heat transfer modes are expected to increase with temperature. Theoretical models have pointed to single constituent chloride data as supporting evidence for theory, having shown a weakly negative temperature dependance. Promising single constituent chloride data has been obtained using a technique known as transient grating spectroscopy (TGS, Section 1.6). TGS attempts in fluorides have failed primarily due to material compatibility constraints. Small length and timescales, indicate that TGS is likely not subject to the same contributions from radiation and convection as other experimental techniques. TGS based measurements can also result in the acquisition of a material's acoustic properties (ex. sound speed), a body of literature that is equally sparse and that can have serious impacts on the modeling of transient scenarios in advanced reactors.

At the outset of this thesis, it was hypothesized that by designing a fluoride salt compatible setup for transient grating spectroscopy, the longstanding disagreement between thermal conductivity theory and experiments would finally be rectified for fluoride molten salts. As with most research projects, the results of this work did not directly confirm the initial hypothesis, however, numerous insights and accomplishments were made in its pursuit.

This project resulted in the design and validation of a versatile fluoride salt compatible optical measurement system (Section 2.1), where the salt sits within a graphite cell with two diamond windows 180 degrees from one another facilitating light transmission. The use of diamond windows in a molten salt environment was found to be sufficient but not immune to degradation, experiencing reduced transparency on a roughly 20-hour timescale when held above 500°C.

The validation of the system's performance was achieved by using lithium chloride as a reference material (Section 2.3). Sound speed measurements in lithium chloride represented the first TGS based measurements of molten halide salt acoustic properties, with previous measurements having been performed using a double transducer method. Results for both thermal conductivity and sound speed displayed excellent agreement with the LiCl literature.

Although it had previously been suggested that TGS based measurements were not subject to contributions from radiative heat transfer, a rigorous analysis had not been performed. As this was a primary factor for the shortcoming of previous techniques, a derivation of the potential contributions in TGS was undertaken (Section 3.1). An analytical expression was found for the maximum possible contribution (Section 3.2), while more realistic estimates were developed using approximations for fluoride salt optical properties (Section 3.3). Both calculations showed that for the characteristic heat transfer distance (**μm**) that TGS typically operates on, radiative contributions are indeed negligible.
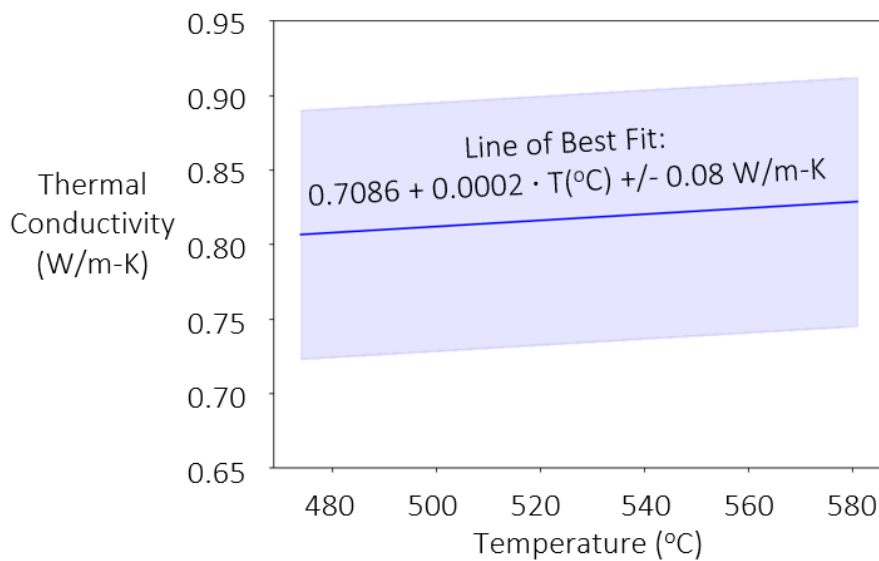
Figure 48. FLiNaK thermal conductivity relation obtained from TGS. TGS thermal diffusivity data has been converted to thermal conductivity using the recommended correlations for FLiNaK density (ρ= 2579 - 0.624 · T[K] in kg/m3) and heat capacity (C_P = 1884 in J/kg-K) [10].Uncertainty (shaded region) represents the propagated 95% confidence interval of the thermal diffusivity fit, along with a 2% and 10% uncertainty for density and heat capacity respectively.

Confirmation of the negligible role of radiation in TGS set the stage for potentially the first fluoride salt thermal conductivity measurements that did not have confounding contributions from additional

modes of heat transfer (Section 4), with FLiNaK (Eutectic of LiF, NaF and KF, a commonly proposed coolant salt) being selected as an initial test case. Results showed a relatively flat but slightly increasing thermal conductivity value as a function of temperature.

Prior to the TGS measurements, the most recent data for the thermal conductivity of FLiNaK had been obtained by using laser flash analysis (LFA), showing a large positive temperature coefficient. To further understand the differences between the two techniques, the LFA measurements were simulated using computational fluid dynamics (Section 4.3). Modeling the LFA measurements with and without radiation, showed that radiation likely is playing a significant role in the LFA geometry leading to an artificially large positive slope. Deviations between the expected heat transfer and paths present in laser flash crucible design indicated a likely underestimation of thermal conductivity at low temperatures. These two observations suggest that careful consideration must be taken when using LFA for high temperature transparent liquids. Correcting directionally for the error uncovered in the LFA measurements provided qualitative validation of the TGS results.
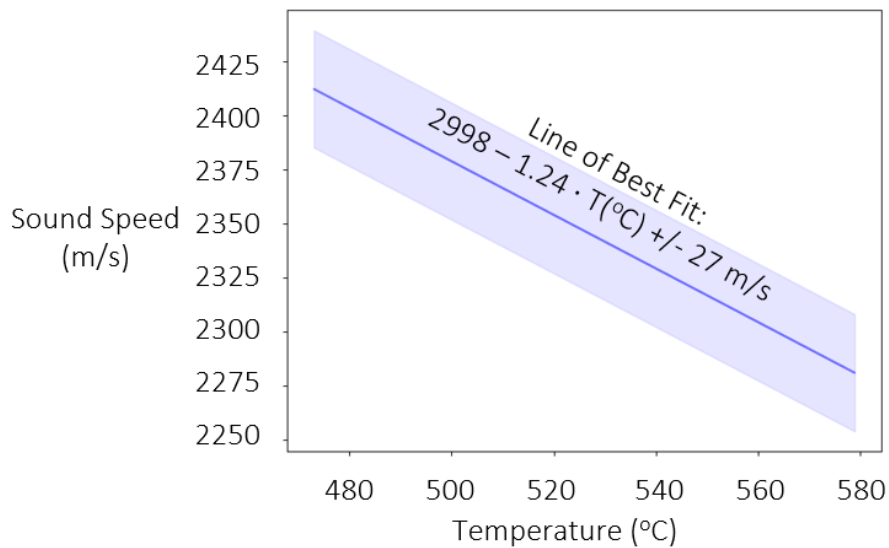
Figure 49. FLiNaK sound speed relation obtained from TGS. Uncertainty (shaded region) represents the propagated 95% confidence interval of the TGS data fit.

Improvement over the previous LFA measurements is promising, however, a continued discrepancy with theory on the sign of the temperature coefficient must be addressed. Many theoretical models rely on sound speed as an input and have turned to estimates when no experimental data has been available. As a result of the TGS measurements, the first experimental sound speed data for FLiNaK has been obtained (Section 4.4), showing values that are lower than theoretical estimates. The use

81

of a lower sound speed values reduced the magnitude of the theoretical thermal conductivity temperature coefficient, providing better agreement with the results from TGS.

As previous explanations (radiation and convection) for experimentally observed positive temperature coefficients have been shown to not be applicable to TGS measurements, several new proposals for why a positive temperature coefficient may be observed were put forward (Section 5).

Of the three constituents in FLiNaK, KF has both the highest vapor pressure and lowest single constituent thermal conductivity. Disproportionate loss of KF into the vapor phase as temperature increases could results in an experimentally observed positive temperature coefficient for the thermal conductivity of FLiNaK (Section 5.1). A vapor pressure-based explanation is consistent with the negative temperature coefficient observed in single constituent salts as no composition change would be observed. However, literature data on the vapor pressure of FLiNaK indicates that this effect is likely small.

An alternative hypothesis for the observation of a positive temperature coefficient comes from uncertainty in other salt properties such as heat capacity (Section 5.2). TGS measurements results in the acquisition of thermal diffusivity which is then converted to thermal conductivity with knowledge of the salt's density and heat capacity Existing heat capacity data for FLiNaK has shown large variations even disagreeing on the sign of the property's temperature coefficient. The use of the 1956 Powers heat capacity data set [83] allows TGS results to be converted to thermal conductivity values that decreases with temperature for the first time in fluorides (Section 5.2).

Finally, diffusive contributions to thermal conductivity, such as that observed in the gas phase, elicit a positive temperature dependance. Most molten salt theoretical models neglect diffusive contributions as they are likely to only contribute a few percent of the total thermal conductivity. The use of diffusive contributions would further decrease the magnitude of the theoretical temperature coefficient, providing a further step in the direction of good agreement with the results of TGS (Section 5.3).

Ultimately, this thesis points to a new hypothesis that although the temperature dependance of fluoride salt thermal conductivity is likely negative, the magnitude of the coefficient is expected to be small, and thus the property should be considered weakly temperature dependent. The results from TGS although unsatisfying in their ability to completely validate existing theoretical models, have provided the field with a critical data set for both thermal conductivity and sound speed in a

highly relevant fluoride salt (FLiNaK). Numerous questions and future directions in line with the initial motivation of safe and cost-effective implementation of molten salt-based energy technologies have been uncovered. It is the hope that this thesis can act as guide for further pursuits of fundamental understanding of an interesting and widely applicable class of fluids.

6.2   Future directions
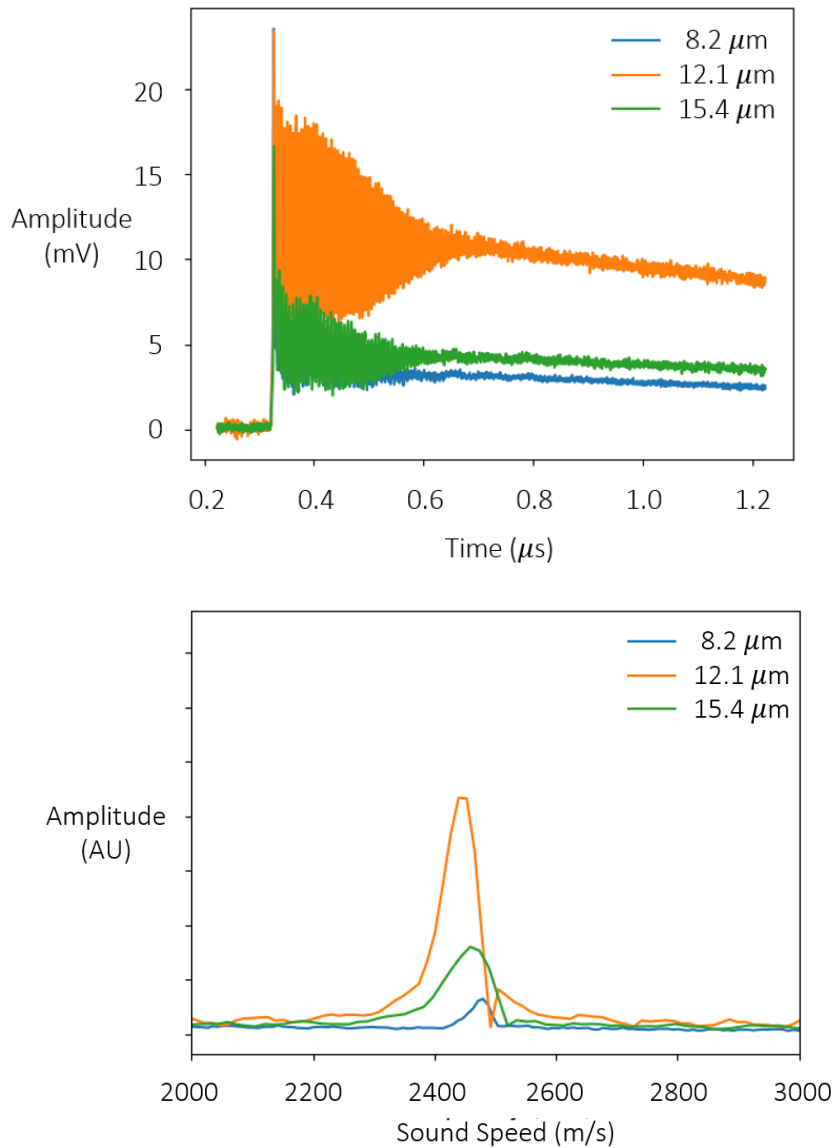
Figure 50. (Top) Raw short timescale acoustic signal obtained in FLiNaK + 1.1wt% CoF_2 at 473^0C at a variety of grating spacings. (Bottom) Fourier transform of the raw acoustic signals (Top) for three different gratings spacings. Frequencies have been converted to sound speed by multiplying by the grating spacing.

The first future research direction relates to the accuracy of the current TGS setup. Measurements at a single temperature have shown that changes in grating spacing albeit over a limited range do not influence results significantly (Figure 50 (Bottom)). However, signal strengths were shown to be grating spacing dependent (Figure 50 (Top)), a potentially uninteresting result born from sub-optimal alignment. Although it is unlikely that this result will change as a function of temperature, a full confirmatory study where sound speed and thermal diffusivity are obtained at different grating spacings as a function of temperature should be undertaken. If a large enough range in grating spacings are used, this trial could act as a means of validating the theoretical contributions from radiative heat transfer calculated in Section 3.4. At large grating spacings (> mm) it is expected that TGS obtained thermal diffusivity results would elicit a stronger more positive slope, consistent with the non-negligible presence of radiative heat transfer.

Although, the use of a 5 μJ/pulse pump laser proved inadequate for measurable grating formation in FLiNaK, a straightforward and direct way to test the influence of pump power would be to repeat the LiCl trials with the higher-powered pump laser (50 μJ/pulse). As no measurable change in the FLiNaK results were observed when changing the dye concentration (Figure 33), it is not expected that an alternative means of influencing the degree of absorption or grating strength (pump power) will prove interesting, however, this should be confirmed.
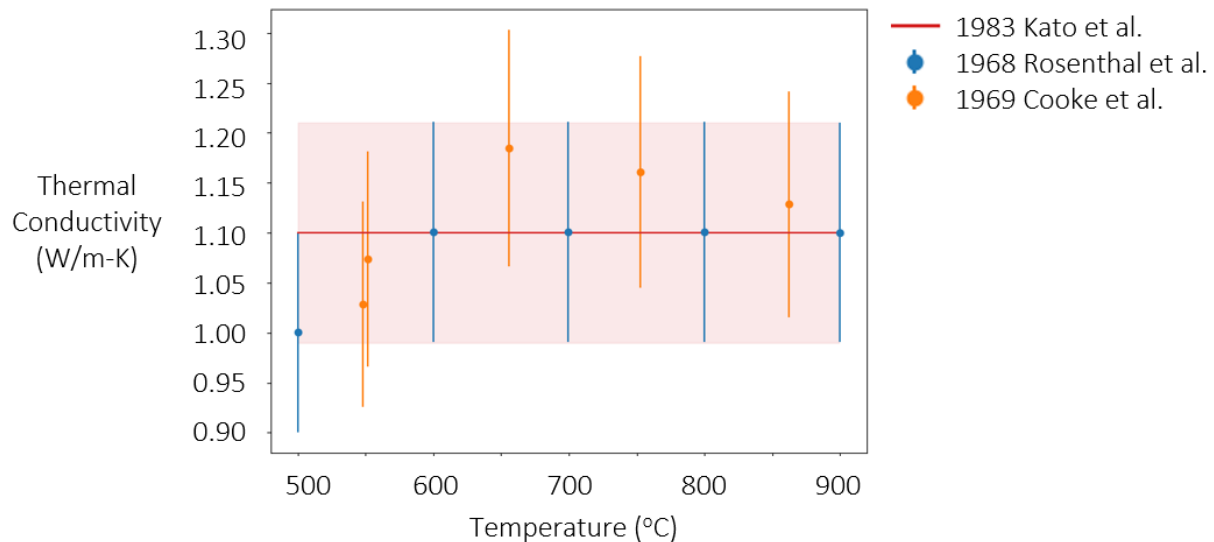
Figure 51. Several temperature dependent experimental thermal conductivity values for FLiBe, including a stated 10% uncertainty [89] [87] [88].

Following additional validation of the TGS setup, measurements in alternative fluoride salts should be considered. Similarly to FLiNaK, FLiBe ($0.66LiF - 0.33BeF_2$) has received significant interest for its potential use as a coolant in advanced fission and fusion systems [86]. Thermal conductivity values for FLiBe are similarly plagued by large uncertainties and indicate a flat to slightly increasing value as a function of temperature [87] [88] [89]. Additional handling considerations associated with beryllium bearing salts is likely to be the biggest hurdle for this trial, and therefore an additional setup reserved for beryllium experiments should be considered.

In addition to engineering relevant salts, a useful dataset for the theoretical community would be to perform measurements on single constituent salts such as LiF, NaF and KF. If fluorides do indeed elicit a different temperature response than chlorides, single constituent data offer's the best comparison for existing models and literature. However, as all three alkali metal fluorides have melting points greater or equal to roughly 850°C, system modifications related to the elevated temperatures would need to be considered. To go beyond the current maximum temperature of 750°C, a higher-powered power source (>60V DC) or external vacuum chamber insulation would be required. Based on experience at temperatures greater than 700°C the cell's diamond windows are expected to continue to provide transparency at elevated temperatures, however, their lifetime will undoubtedly be reduced.

The validity of diamond as a transparent fluoride salt compatible material opens the door for additional optical measurements of molten salts. Techniques such as Raman Spectroscopy that rely on scattered light have been able to develop setups where the salt is not required to be in contact with a viewport [90], while absorption-based measurements such as Fourier transform infrared spectroscopy (FTIR) have already proposed designs for diamond-based setups [91]. In its current state, the system designed for TGS could provide crude absorption-based measurements, however, the thickness of the salt sample (12mm) may ultimately prove limiting. Subsequent cell iterations could be designed to limit salt thickness in the direction of an incoming laser, however, these cells would have limited applicability for TGS due to the requirement that the grating depth greatly exceed its spacing (1D heat transfer approximation). Although the deterioration of the diamond window's transparency has proven too slow to influence the results of TGS, additional considerations may need be made for measurements tied to the quantity of transmitted light as a function of temperature. Pre and post transmission measurements of an empty cell may prove sufficient to define the uncertainty of the salt's absorption properties, however, for long measurements, more elaborate schemes may be required.

Although not used frequently, TGS measurements also result in the acquisition of a third property known as the acoustic damping parameter (C_3 fitting parameter of Eq 11, related to the rate at which acoustic oscillations dissipate in the short timescale signals). Physically the acoustic damping parameter can be expressed as a function (Eq 49) of a variety of salt properties namely the salt's density (ρ), shear viscosity (η), volumetric heat capacity (C_V), heat capacity ratio (γ), thermal conductivity (λ), and the bulk or volume viscosity (ξ, a parallel of shear viscosity for compression and expansion) [50]. With knowledge of all but one of the salt properties expressed in Eq 49, acquisition of the acoustic damping parameter could provide a means of solving for the unknown. In particular, bulk viscosity is an often-neglected quantity in hydrodynamics as it is only applicable in the absence of incompressible assumptions, and thus has received limited attention for molten salts [92] [93]. However, the utility of bulk viscosity data may come as a means of further understanding molten salt vibrational and rotational degrees of freedom, a proxy for composition change, or an additional tool to validate theoretical models [94].

$$C_3 = \Gamma = \frac{1}{2\rho_o}\left(\frac{4}{3}\eta + \xi + \frac{(\gamma - 1)\lambda}{\gamma C_v}\right) \hspace{3cm} \text{Eq 49}$$
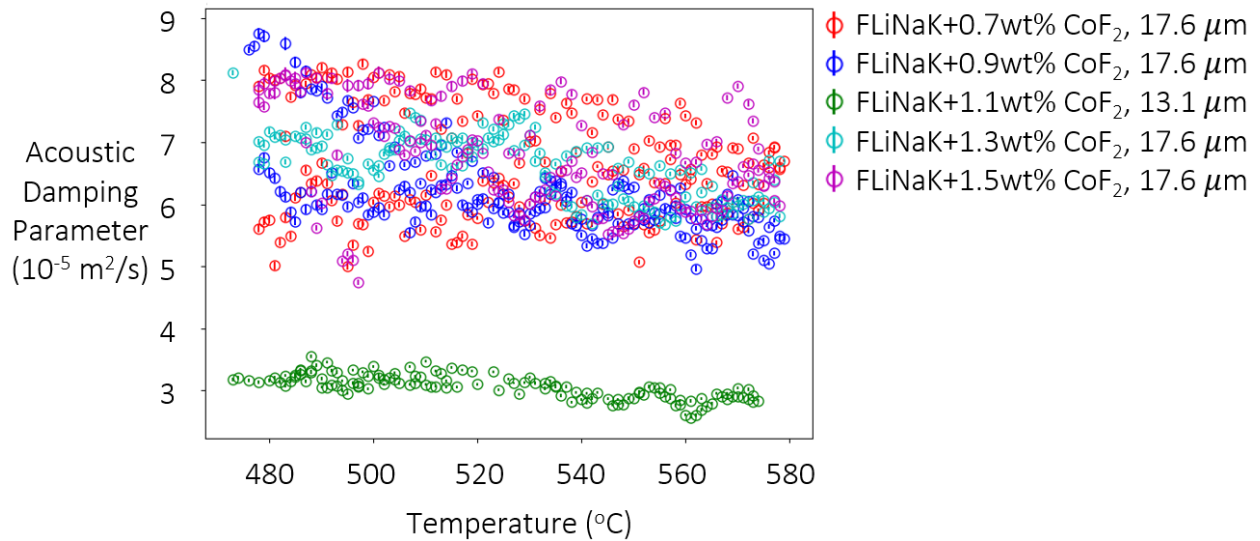
Figure 52. The acoustic damping parameter (C_3 fitting parameter of Eq 11) as a function of temperature and CoF_2 concentration in FLiNaK. The 1.1wt%CoF_2 measurements were done on a different grating spacing (13.1μm) compared to the other samples (17.6μm). Each data point results from fitting a 10,000 grating formation and decay average signal with uncertainty being stated as the standard error of the fit.

Plotting the acoustic damping parameter as a function of temperature and CoF_2 concentration in FLiNaK (Figure 52) shows that the current TGS measurements appear insensitive to the degree of CoF_2, however, a large difference is observed for the 1.1wt% CoF_2 sample that employed a different grating spacing (13.1 vs 17.6μm). The fact that the parameter appears sensitive to the difference in length scale or oscillation frequency beyond accounting for the $(2\pi/d)^2$ dependance of the exponent in Eq 11 is interesting and warrants further investigation.

In summary, the ability to obtain fundamental properties in a non-contact optical measurement for fluoride molten salts opens the door for numerous new research directions. This thesis thus provides merely a small step in comparison to the potential future characterization efforts that can be undertaken.

References

[1] J. Serp, M. Allibert, O. Benes, S. Delpech, O. Feynberg, V. Ghetta, D. Heuer, D. Holcomb, V. Ignatiev, J. Kloosterman, L. Luzzi, E. Merle-Lucotte, J. Uhlir, R. Yoshioka and D. Zhimin, "The molten salt reactor (MSR) in generation IV: Overview and perspectives," Progress in Nuclear Energy, 77, 308-319, 2014.

[2] B. N. Sorbom, J. Ball, T. R. Palmer, F. J. Mangiarotti, J. M. Sierchio, P. Bonoli, C. Kasten, D. A. Sutherland, H. S. Barnard, C. B. Haakonsen, J. Goh, C. Sung and D. G. Whyte, "ARC: A compact, high-field, fusion nuclear science facility and demonstration power plant with demountable magnets," Fusion Engineering and Design, 100, 378-405, 2015.

[3] C. Halliday and T. A. Hatton, "The potential of molten metal oxide sorbents for carbon capture at high temperature: Conceptual design," Applied Energy, 280, 2020.

[4] Y. Tian and C. Y. Zhao, "A review of solar collectors and thermal energy storage in solar thermal applications," Applied Energy, 104, 538-553, 2013.

[5] L. Toth, G. Cul, S. Dai and D. Metcalf, "Molten fluoride fuel salt chemistry," AIP Conference Proceedings, 346, 617-626, 1995.

[6] Y. Marcus, "The compressibility of molten salts," The Journal of Chemical Thermodynamics, 61, 7-10, 2013.

[7] A. Gheribi, J. Torres and P. Chartrand, "Recommended values for the thermal conductivity of molten salts between the melting and boilng points," Solar Energy Materials and Solar Cells,126, 11-25, 2014.

[8] X.-H. An, J.-H. Cheng, H.-Q. Yin, L.-D. Xie and P. Zhang, "Thermal conducitvity of high temperature fluoride molten salt determined by laser flash technique," International Journal of Heat and Mass Transfer, 2015.

[9] V. Nunes, M. Lourenco, F. Santos and C. Nieto de Castro, "Importance of accurate data on viscosity and thermal conductivtiy in molten salt applications," Journal of Chemical Engineering Data, 48, 466-450, 2003.

[10] R. R. Romatoski and L. W. Hu, "Fluoride salt coolant properties for nuclear reactor applications: A review," Annals of Nuclear Energy, 109, 635-647, 2017.

[11] A. E. Gheribi and P. Chartrand, "Thermal conductivty of molten salt mixtures: Theoretical model supported by equillibirum molecular dynamics simulations," The Journal of Chemical Physics, 144, 084506, 2016.

[12] G. Sengler, F. Foret, G. Schlosser, R. Lisdat and S. Stelletta, "EPR core design," Nuclear Engineering and Design, 187(1), 79-119, 1999.

[13] C. B. Davis, "Implementation of Molten Salt Properties into RELAP5-3D/ATHENA," Idaho National Engineering and Environmental Laboratory, EXT-05-02658, 2005.

[14] E. Cervi, A. Lorenzi, A. Cammi and L. Luzzi, "Development of a multiphysics model for the study of fuel compressibility effects in the molten salt fast reactor," Chemical Engineering Science, 193, 379-393, 2019.

[15] G. J. Janz and R. P. T. Tomkins, "Physical properties data compilations relevatnt to energy storage. IV molten salts: data on additional single and multi-component systems," National Standard Reference Data System, 1981.

[16] M. V. Smirnov, V. A. Khohklov and E. S. Filatov, "Thermal conductivity of molten alkali halides and their mixtures," Electrochimica Acta, 32(7), 1019-1026, 1986.

[17] V. Khokhlov, V. Ignatiev and V. Afonichkin, "Evaluating physical properties of molten salt reactor fluoride mixtures," Journal of Fluorine Chemistry, 130, 30-37, 2009.

[18] V. Khokhlov, I. Korzun, V. Dokutovich and E. Filatov, "Heat capacity and thermal conductivity of molten ternary lithium, sodium, poassium, and zirconium fluorides mixtures," Journal of Nuclear Materials, 410, 32-38, 2011.

[19] C. T. Ewing, J. R. Spann and R. R. Miller, "Radiant transfer of heat in molten inorganic compounds at high temperatures," Journal of Chemical and Engineering Data, 7(2), 246-250, 1962.

[20] W. D. Powers, S. I. Cohen and N. D. Greene, "Physical properties of molten reactor fiels and coolants," Nuclear Science and Engieering, 17(2), 200-211, 1963.

[21] R. DiGuilio and A. Teja, "A rough hard-sphere model for the thermal conductivtiy of molten salts," International Journal of Thermophsyics, 13(5), 855-871, 1992.

[22] V. D. Golyshev and M. A. Gonik, "High-temperature thermophysical properties of nonscattering semitransparetn materials. III. therml conductivtiy of melts," High Temperatures-High Pressures, 24(6), 677-688, 1992.

[23] V. D. Golyshev, M. A. Gonik, V. A. Petrov and Y. M. Putilin, "Experimental investigation of the thermal-conductivty of transparent melts," Thermophysical Properties of Materials, 21(5), 684-687, 1983.

[24] Y. Nagasaka, N. Nakazawa and A. Nagashima, "Experimental determination of the thermal diffusivity of molten alkali halides by the forced rayleigh scattering method. I. Molten LiCl, NaCl, KCl, RbCl and CsCl," International Journal of Thermophysics, 13(4), 555-574, 1992.

[25] P. W. Bridgman, "The thermal conductivity of liquids," Proceedings of the National Academy of Sciences, 9, 1923.

[26] J. Bockris and N. Richards, "The compressibilities, free volumes and equation of state for molten electrolytes: Some alkali halides and nitrates.," Proceedings of the Royal Societ of London. Series A, Mathematical and Physical Sciences, 241(1224), 44-66, 1957.

[27] A. G. Turnbull, "Thermal conductivity of molten salts. 2. Theory and results for pure salts," Australian Journal of Applied Science, 12, 1961.

[28] Y. Nagasaka and A. Nagashima, "The thermal conductivity of molten NaNO3 and KNO3," International Journal of Thermophysics, 12(5), 769-781, 1991.

[29] J. K. Horrocks and E. McLaughlin, "Thermal conductivity of simple molecules in the condensed state," Transactions of the Faraday Society, 56, 206-212, 1960.

[30] S. E. Gustafsson, N. O. Halling and R. A. E. Kjellander, "Optical determination of thermal conductivity with a plane source technique," Zeitschrift für Naturforschung A, 23, 682-686, 1968.

[31] Y. Nagasaka and A. Nagashima, "Corresponding states correlation for the thermal conductivity of molten alkali halides," International Journal of Thermophysics, 14(4), 1993, 1992.

[32] D. F. Williams, "Assessment of candidate molten sal coolants for the NGNP/NHI heat-transfer loop," Oak Ridge National Lab, TM-2006, 69, 2006.

[33] N. Ohtori, T. Oono and K. Takase, "Thermal conductivity of molten alkali halides: Tempearture and density dependence," The Journal of Chemical Physics, 130, 2009.

[34] Y. Ishii, K. Sato, M. Salanne, P. A. Madden and N. Ohtori, "Thermal conductivity of molten alkali metal fluorides (LiF, NaF, KF) and their mixtures," The Journal of Physical Chemistry B, 118, 3385-3391, 2014.

[35] N. Galamba and C. A. Nieto de Castro, "Equillibirum and nonequilibirum molecualr dynamics simulations of the thermal conductivity of molten alkali halides," The Journal of Chemical Physics, 126, 204511, 2007.

[36] D. P. Sellan, E. S. Landry, J. E. Turney, A. J. McGaughey and C. H. Amon, "Size effects in molecular dynamics thermal conductivity predictions," Physical Review B, 81, 214305, 2010.

[37] D. J. Evans, "Homogeneous NEMD algorithim for thermal conductivity - Application of non-canonical linear response theory," Physics Letters, 91A (9), 457-460, 1982.

[38] D. J. Searless and D. J. Evans, "The fluctuation theorem and Green-Kubo relations," Journal of Chemical Physics, 112(22), 9727-9735, 2000.

[39] N. Ohtori, M. Salanne and P. A. Madden, "Calculations of the thermal conductivities of ionic materials by simulation with polarizable interaction potneitals," The Journal of Chemical Physics, 130, 104507, 2009.

[40] H. Lee and T. Oda, "Development of potential models for alkali halides using first-principles calculation," Transaction of the Korean Nuclear Society Autum Meeting, 2018.

[41] F. G. Fumi and M. P. Tosi, "Ionic sizes and born repulsive parameters in the NaCl-type alkali halides - I," Journal of Physical Chemistry Solids, 25, 31-43, 1963.

[42] M. P. Tosi and F. G. Fumi, "Ionic sizes and born repulsive repulsive paramters in the NaCl - type alkali halides - II," Journal of Physical Chemistry Solids, 25, 45-52, 1964.

[43] E. Mclaughlin, "The thermal conductivity of liquids and dense gases," Chemical Reviews, 64(4), 389-428, 1964.

[44] Y. Ueiki, N. Fujita, J. Yagi, M. Shibaraha and A. Sagara, "Thermal conductivity measurment of fluoride molten salt FLiNaK by Transient hot-wire method," High Temperatures-High Pressures, 46, 247-254, 2017.

[45] J. A. Fortner, M. Rose and M. A. Williamson, "Standard methods for heat capacity and thermal conductivity measurements for molten salts," Fuel Cycle Reasearch and Development, Argonne National Laboratory, 2018.

[46] T. Omotani and A. Nagashima, "Thermal conductivity of molten salts, HTS, and the LiNO3-NaNO3 system, using a modified hot-wire method," Journal of Chemical Engineering Data, 29, 1-3, 1984.

[47] E. Chaleff, N. Antolin, W. Windl and T. Blue, "Ab-Initio calculation of spectral absorption coefficients in molten fluoride salts with metal impurities," Nuclear Technology, 204(1), 59-65, 2018.

[48] N. Nakazawa, Y. Nagasaka and A. Nagashima, "Experimental determination of the thermal diffusivity of molten alkali halides by the forced rayleigh scattering method. II. Molten NaBr, KBr, RbBr and CsBr," International Journal of Thermophysics, 13(5), 753-762, 1992.

[49] N. Nakazawa, Y. Nagasaka and A. Nagashima, "Experimental determination of the thermal diffusivity of molten alkali halides by the forced rayleigh scattering method. III. Molten NaI, KI, RbI and CsI," International Journal of Thermophysics, 13(5), 763-772, 1992.

[50] A. R. Duggal and K. A. Nelson, "Picosecond-microsecond structural relaxation dynamics in polypropylene glycol: impulsive stimualted light-scattering experiments," The Journal of Chemical Physics, 94, 7677-7688, 1991.

[51] A. A. Maznev, K. A. Nelson and J. A. Rogers, "Optical heterodyne detection of laser-induced gratings," Optics Letters, 23(16), 1319-1321, 1998.

[52] N. Nakazawa, Y. Nagasaka and A. Nagashima, "Measurment of the thermal diffusivity of molten salts by the forced rayleigh scattering method," High Temperature - HighPressures, 23, 595-604, 1991.

[53] D. K. Tsang, B. J. Marsden, S. L. Fok and G. Hall, "Graphite thermal expansion realtionships for different temperature ranges," Carbon, 43(14), 2902-2906, 2005.

[54] T. G. Kollie, "Measurement of the thermal-expansion coefficient of nickel from 300 to 1000 K and determination of the power-law," Physical Review B, 16(11), 4872-4881, 1977.

[55] L. Olson, J. Ambrosek, K. Sridharan, M. Anderson and T. Allen, "Materials corrosion in molten LiF-NaF-KF salt," Journal of Fluorine Chemistry, 130(1), 67-73, 2009.

[56] L. Toth, J. Young and G. Smith, "Diamond-windowed cell for spectrophotometry of molten fluoride salts," Analytical Chemistry, 41(4), 683-685, 1969.

[57] J. P. Young and J. C. White, "Absorption spectra of molten fluoride salts," Analytical Chemistry, 32(7), 799-802, 1960.

[58] A. Quist, "A windoless cell for laser-raman spectroscopy of molten fluorides," Applied Spectroscopy, 25(1), 80-82, 1971.

[59] Y. Nagasaka, T. Hatakeyama, M. Okuda and A. Nagashima, "Measurement of the thermal diffusivity of liquids by the forced rayliegh scattering method: Theory and experiment," Review of Scientific Instruments, 59, 1156-1168, 1988.

[60] C. Raptis, "A relaible, versitile optical furnace for raman spectroscopy of molten salts and hot solids," Journal of Physics E: Scientific Instruments, 16, 749-752, 1983.

[61] S. G. Robertson and M. P. Short, "2021-Liquid-TGS-RSI," https://github.com/shortlab/2021-Liquid-TGS-RSI, 2021.

[62] COMSOL Multiphysics v. 5.5. www.comsol.com. COMSOL AB, Stockholm, Sweden.

[63] G. C. Chow, "Tests of equality between sets of coeffecient in two linear regressions," Econometrica, 28(3), 591-605, 1960.

[64] Y. Yang and K. A. Nelson, "Tc of the mode coupling theory evaluated from impulsive stimulated light scattering on Salol," Physical Review Letters, 74(24), 4883-4886, 1995.

[65] D. W. Lee and W. D. Kingery, "Radiatiion energy transfer and thermal conductivity of cermaic oxides," Journal of the American Ceramic Society, 53(11), 594-607, 1960.

[66] M. F. Modest, "Radiative heat transfer, Third Edition, Ch 10 The radiative transfer equation in participating media," Elsevier, 2013.

[67] H. H. Li, "The infared absorption coefficient of alkali halides," International Journal of Thermophysics, 1(1), 97-134, 1979.

[68] H. H. Li, "Refractive index of alkali halides and its wavelgnth and temperature derivatives," Journal of Phyiscal and Chemical Reference Data, 5(2), 329-528, 1976.

[69] M. G. Mead, "Comparison of the optical and dielectric properties of crystalline and molten lithium fluoride," Journal of Physics C: Solid State Physics, 7, 445-453, 1974.

[70] J. R. Jasperse, A. Kahan and J. N. Plendl, "Temperature dependence of infared dispersion in ionic crystals LiF and MgO," Physical Review, 146(2), 425-542, 1965.

[71] J. K. Wilmshurst, "Infared spectra of molten salts," The Journal of Chemical Physics, 39(10), 1963.

[72] J. P. Young and J. C. White, "Absorption spectra of molten fluoride salts," Analytical Chemistry, 32(7), 799-802, 1960.

[73] L. Dusza, "Combined solution of the simultaneous heat loss and finit pulse corrections with the laser flash method," High Temperatures - High Pressures (27/28), 467-473, 1995.

[74] Siemens Industries Digital Software, "Simcenter STAR-CCM+, version 2021.1," Siemens, 2021.

[75] V. Venkatakrishnan, "On the accuracy of limiters and convergence to steady state solutions," Aeropsaces Sciences Meeting & Exhibit, 1993.

[76] J. Kincaid and H. Eyring, "Free volumes and free angle ratios of molecules in liquids," Jorunal of Chemical Physics, 1938.

[77] A. E. Gheribi, J. A. Torres and P. Chartrand, "Recommended values for the thermal conductivity of molten salts between the melting and boiling points," Solar Energy Materials & Solar Cells, 126, 11-25, 2014.

[78] M. V. Smirnov, V. I. Minchenko and Y. V. Konovalov, "The sound velocity and adiabatic compressibility of molten alkali fluorides and their binary mixtures," Proceeding of the first International Symposium on Molten Salt Chemistry and Technology, 457-460, 1983.

[79] R. R. Romatoski and L. W. Hu, "Fluoride salt coolant properties for nuclear reactor applications: A review," Annals of Nuclear Energy, 109, 2017.

[80] K. Takase, Y. Matsumoto, K. Sauto and N. Ohtori, "Thermal conductivity in molten alkali halides: composition dependence in mixtures of (Na-K)Cl," Molecular Simulation, 38(5), 2011.

[81] R. G. Ross, "Thermal conductivtiy of solids and liquids under pressure," Reports on Progress in Physics, 47, 1347-1402, 1984.

[82] Y. Sekiguchi, K. Uozumi, T. Koyama and T. Terai, "Fundamental study on the vaporization of cesium and iodine dissolved in LiF-NaF-KF molten salt," Journal of Nuclear Materials, 522, 136-143, 2019.

[83] W. D. Powers and G. C. Blalock, "Enthalpies and heat capacities of solid and molten fluoride mixtures," Reactor Experimental Engineering Division, ORNL-1956, 1956.

[84] A. Bengston, H. O. Nam, S. Saha, R. Sakidja and D. Morgan, "First-principles molecular dynamics modeling of the LiCk-KCl molten salt system," Computational Materials Science, 83(15), 362-370, 2014.

[85] H. O. Nam, "First-principles molecular dynamics modeling of the molten fluoride salt with Cr solute," Journal of Nuclear Materials, 449(1-3), 148-157, 2014.

[86] S. Delpech, C. Cabet, C. Slim and G. Picard, "Molten fluorides for nuclear applications," Materials Today, 13(12), 34-41, 2010.

[87] J. W. Cooke, H. W. Hoggman and J. J. Keyes, "Thermophysical properties in molten-salt reactor program semiannual progress report for period ending February 28 1969," ORNL-4396, 1969.

[88] Y. Kato, K. Furukawa, N. Araki and K. Kobayasi, "THermal diffusivity measurment of molten salts by use of a simple ceramic cell," High Temp - High Press, 15, 191-198, 1983.

[89] M. W. Rosenthal, R. B. Briggs and P. R. Kasten, "Molten-salt reactor program semiannual progress report for period ending August 3,1968," ORNL-4344, 1968.

[90] Y. Li, X. Liu, B. Wang and C. Wang, "Raman and theoretical studies on structural evolution of Li2BeF4 and binary LiFBeF2 melts," Journal of Molecular Liquids, 325, 2021.

[91] C. Coyle, E. Baglietto and C. Forsberg, "Advancing radiative heat transfer modeling in high-temperature liquid salts," Nuclear Science and Engineering, 194, 782-792, 2020.

[92] R. W. Higgs and T. A. Litovitz, "Ultrasonic absorption and velocity in molten salts," The journal of the acoustical socity of america, 32(9), 1108-1115, 1960.

[93] T. Ejima and T. Yamamura, "Thermophyiscal properties of molten salts: Hypersonic velocities of molten alkali nitrates and their mixtures," International Journal of Thermophysics, 5(2), 131-148, 1984.

[94] A. S. Dukhin and P. J. Goetz, "Bulk viscosity and compressibility measurement using acoustic spectroscopy," The Journal of Chemical Physics, 130, 2009.